Institut de Physique du Globe de Paris

Ecole doctorale des Sciences de la Terre

Th de Doctorat

pour l'obtention du titre de

Docteur en Science

de l'Institut de Physique du Globe de Paris

SpecialitGeophysique

Soutenue par

Clément Thorey

Magmatisme intrusif sur les plans telluriques

Équipe Planétologie et Sciences Spatiales,

dndue le 5 Dmbre, 2013.

Jury :

Directeur:	Chloé Michaut	-	IPGP (Paris)
Co-directeur:	Mark Wieczorek	-	IPGP (Paris)
Rapporteur :		-	
Rapporteur :		-	
Examinateur :		-	
Examinateur :		-	

Remerciements

Je remercie marion rouault mae sans qui tout ceci n'aurait jamais vu le jour ;)

Contents

Rm la probltique et rltats principaux

Part I

Dynamique des magmas ible profondeur

Chapter 1

Magmatisme intrusif

Contents

1.1 Formation, transport et stockage des magmas

1.1.1 Formation

La majorité des magmas sont formées par fusion partielle des roches du manteau supérieurs. Cependant, dans les conditions normales de pression, la température du manteau supérieur n'est pas suffisante pour provoquer la fusion partielle des roches mantelliques (Figure 1.1) et d'autres mécanismes sont nécessaires pour amener les roches du manteau à croiser leur liquidus. Au

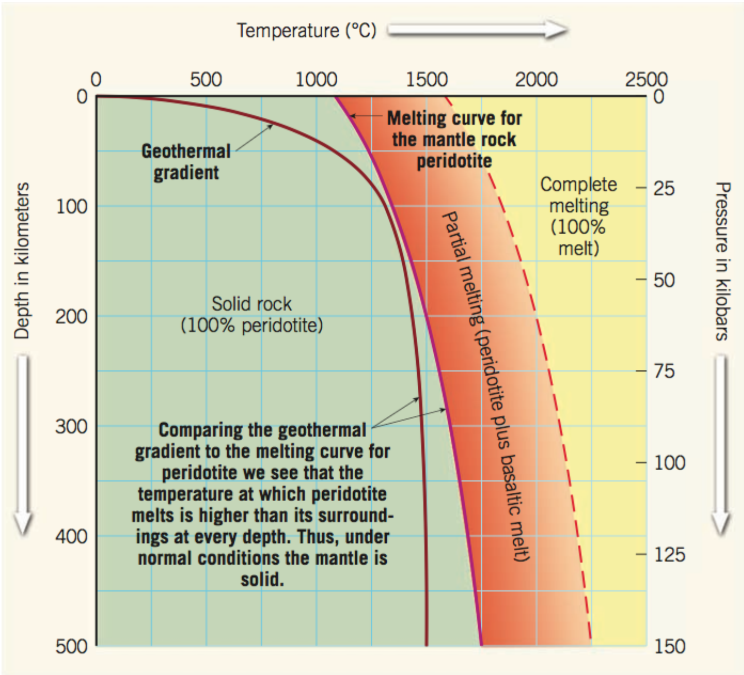

Figure 1.1: Temperature (C) versus depth (km). Reproduced from *Tarbuck et al.* (1998).

niveau des zones d'extension, i.e. au niveau des dorsales océaniques par exemple ou au sein des panaches mantelliques, la fusion partielle est ainsi causé par décompression des roches mantelliques. Au niveau des zones de subduction, les mécanismes mises en jeux sont plus complexes et font intervenir la déshydratation par chauffage des roches, la migration des fluides provoquant la fusion des roches alentours.

1.1.2 Transport

Les liquides de fusions ainsi formés sont moins dense que les roches solides alentours et s'élèvent donc, par compaction et percolation au travers de la matrice mantellique (*McKenzie*, 1984, 1985). Le magma, liquide de fusion + cristaux, s'accumule ensuite au sein de chenaux, i.e. de dykes ou le long de faille pré-existantes pour remonter rapidement vers les couches superficielles de la croûte (*Lister and Kerr*, 1991; *Clemens and Mawer*, 1992; *Petford et al.*, 1993; *Rubin*, 1995). En effet, bien que l'idée du magma remontant lentement au sein de gros volume diapirique est encore parfois invoqué au sein de la base ductile de la croûte (*Weinberg and Podladchikov*, 1994; *Weinberg*, 1996), le transport rapide du magma au sein des dykes permet de résoudre de nombreux problèmes, thermiques et mécaniques, associés à la remonté diapirique de gros volume de magma au sein des parties supérieurs fragiles de la croûte invoquée historiquement (*Miller and Paterson*, 1999).

1.1.3 Stockage

Historiquement, les travaux de *Walker* (1989) ont montré que les magmas remontent jusqu'à rencontrer leur zone de flotabilité neutre, une région ou la densité de la roche encaissante est proche de celle du magma lui même. En effet, au dessus de cette couche, le magma est plus dense que la roche encaissante et sa flotabilité l'entraîne vers le bas. De nombreux travaux, tant théoriques (*Lister and Kerr*, 1991; *Petford et al.*, 1993; *Rubin*, 1995) que expérimentaux (*Taisne and Tait*, 2009; *Taisne et al.*, 2011) ont en effet depuis montré que l'ascension d'un dyke était contrôlé par la différence de densité entre la tête de celui ci et la roche encaissante. Lorsque le dyke entre dans une région de densité inférieure, la surpression induite peut, sous certaines conditions, conduire à l'étalement du magma au niveau de la base de la région de plus forte densité (*Taisne et al.*, 2011). Le magma s'étale donc par gravité à la base de cette couche permettant ainsi la formation de réservoir magmatique sous forme d'intrusion magmatique au sein de la croûte. L'existence et la localisation de cette zone de flottabilité neutre, et donc la question de l'éruptabilité d'un magma, dépend de la densité relative entre la croûte et le magma. Elle dépend donc non seulement de la nature de la croûte, i.e. de sa composition, mais aussi de sa porosité, de la composition du magma, de sa température et de sa teneur en volatils, qui varie, elle, largement avec la pression et la profondeur.

Plus récemment, d'autres études ont montré que les contrastes de rigidité entre les différentes couches crustales pourraient aussi jouer un rôle non négligeable sur l'arrêt de l'ascension des dykes (*Menand*, 2011). En effet, des expériences réalisées par *Kavanagh et al.* (2006) ont montré que la propagation d'un dyke peut être arrêté quand celui ci rencontre une interface qui sépare un milieu plus rigide surplombant un milieu moins rigide (Figure 1.2). Le dyke arrête ainsi son ascension verticale et s'étale horizontalement juste en dessous de la couche de rigidité plus élevée. Ce mécanisme est d'autant plus efficace que le contraste de rigidité est important (*Kavanagh et al.*, 2006).

Finalement, les contraintes, locales ou globales, peuvent aussi dévier la trajectoire d'un dyke et influencer les trajets des magmas au sein de la croûte. En effet, des études ont montré que les intrusions magmatiques tendent à se propager perpendiculairement à la direction des contraintes de compressions (*Anderson*, 1951). Les dykes ont donc tendance à exister dans des situations ou les contraintes de compressions sont horizontales et donc à s'arrêter quand

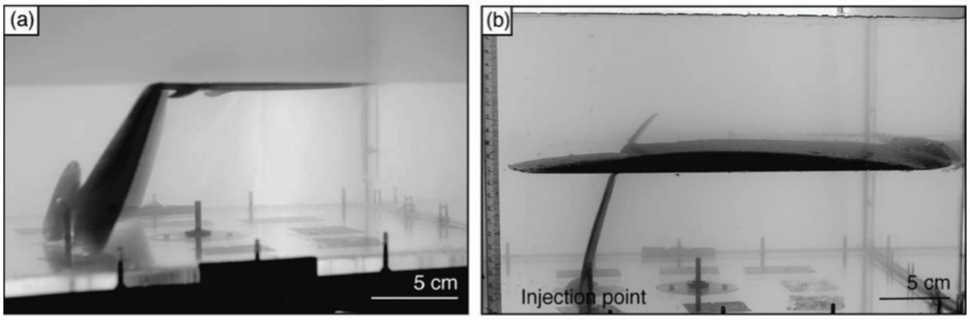

Figure 1.2: a) Photographie de deux des expériences réalisées par *Kavanagh et al.* (2006) sur le comportement d'un dyke à l'interface entre deux milieux de rigidités différentes. a) Le contraste de rigidité est très important et le dyke s'étale sous la couche de rigidité importante. b) Le contraste de rigidité est plus faible et, tout en s'étalant en dessous de la couche de rigidité supérieur, le dyke continue sa progression dans le milieu plus rigide.

le champ de contrainte évolue, d'une contrainte de compression horizontal à vertical comme c'est le cas par exemple au niveau des édifices volcaniques (*Pinel and Jaupart*, 2000, 2004; *Roman and Jaupart*, 2014).

Cependant, si ces différents facteurs jouent sûrement tous un rôle dans le transport et le stockage des magmas au sein de la croûte terrestre, la densité relative du magma et de la roche encaissante est certainement le facteur déterminant dans la mise en place d'intrusion magmatiques et la structure en densité d'une croûte planétaire joue donc un rôle essentielle dans le stockage des magmas.

1.2 Caractérisation du magmatisme intrusif à faible profondeur: apport des observations

1.2.1 Intrusion magmatique sur Terre

La croûte terrestre continentale, épaisse en moyenne de 35 km, a une densité moyenne proche de 2900 kg m^{-3}. De part sa densité relativement basse, elle constitue un filtre efficace à la remonté des magmas en surface qui sont par conséquence préférentiellement stockés en profondeur. *Crisp* (1984) et *White et al.* (2006) estiment en effet à 10 fois supérieur au volume de lave extrudé les volumes de magma intrudés au sein de la croûte continentale. Les mouvements tectoniques au sein de la croute ainsi que l'erosion ont expose nombreuses de ces intrusions magmatiques a la surface. La mise en place ces magmas en

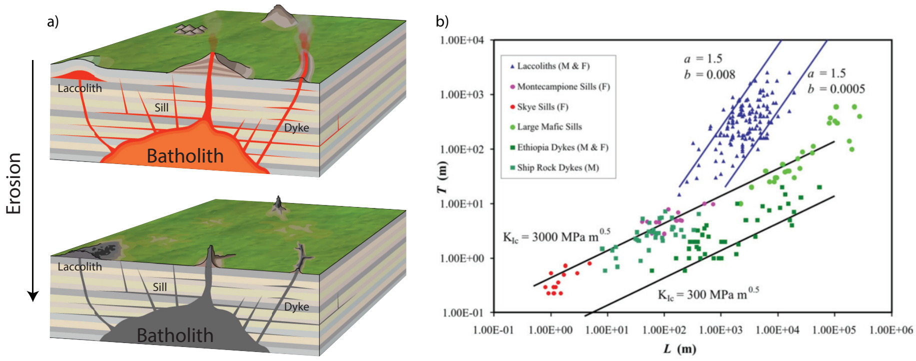

Figure 1.3: a) Différentes formes du magmatisme intrusif: batholith, dyke, sill et laccolith. Dimensions typiques pour des laccoliths, dyke et sill de composition et d'origines différentes repris de *Cruden et al.* (2012).

profondeurs et leur solidification semblent résulter en une grande variété de morphologie et de type d'intrusions différentes dépendante des conditions, profondeurs et caractéristiques mécaniques du milieu encaissant au moment de la formation.

Les batholiths sont de loin les plus imposants représentant de ces familles d'intrusions magmatiques. Ils peuvent atteindre jusqu'à quelques kilomètres d'épaisseur et s'étendre sur des centaines de kilomètres. Par exemple, le batholith de Sierra Nevada est une intrusion granitique qui s'étend sur presque la totalité de la Sierra Nevada en Californie. Il est maintenant clair que la mise en place de ces gigantesques volumes de magmas se forme par incréments successifs de petits volume de magma se solidifiant lors de leur mise en place sur de longues échelle de temps 10^5 to 10^6 années (*Petford et al.*, 2000; *Glazner et al.*, 2004). Dans cette thèse, on va donc se focaliser sur les mécanismes de formations et de mise en places de plus petit volume de magma dans la partie fragile de la croûte continental, des profondeurs inférieurs à 10 km.

On distingue généralement deux types d'intrusions magmatiques: les intrusions discordantes, qui se mettent en place perpendiculairement à la stratification naturelle de la croûte et les intrusions concordantes, qui se mettent en place parallèlement aux couche géologiques. Des études géologiques de terrain ont montré la présence de quatre grandes familles d'intrusions magmatique à faible profondeur.

- Les dykes, par lesquels remontent le magma à travers la lithosphère sont discordants et caractérisé par de faibles rapports d'aspects (Figure 1.3, 1.4 a). Leur épaisseur peut varier de quelques mètres à quelques centaines de mètres d'épaisseur (*Walker*, 1989; *Rubin*, 1995), cependant, l'épaisseur moyenne est de quelques dizaines de mètre. Les dykes de compositions felsiques sont généralement plus épais et moins long que leurs équivalents mafiques (*Rubin*, 1995).

- Les sills, à la différence des dykes, sont concordants (Figure 1.3, 1.4 b,f). Ils se mettent en place le long de discontinuités ou de failles pré-existantes, à la jonction entre deux couches sédimentaires par exemple. Les sills aux dimensions les plus importantes répertoriés sont mafiques et peuvent attendre jusqu'à 100 km sur des épaisseurs de presque 1 km (*Cruden et al.*, 2012). Leurs homologues felsiques, plus rares, sont souvent de dimension plus raisonnable.

- Les laccoliths ont été décrit premièrement par *Gilbert* (1877) suite à son étude géologique des Henry Mountains, dans l'Utah aux Etats-Unis (Figure 1.4 c, d, e). Ils se mettent en place principalement par flexion des couches sédimentaires sus-jascentes, ce qui leur donnent une forme plus ou moins en cloche. *Corry* (1988) a répertorié à peu près 900 laccoliths, principalement dans le nord des Etats-Unis. Leurs épaisseurs varient de quelques dizaines à quelques centaines de mètres et leurs rayons peut atteindre quelques kilomètres pour les plus gros (Figure 1.3 b). Ces laccoliths se sont parfois mis en place les uns sur les autres formant une structure en forme d'arbre de noël (*Corry*, 1988). Cette géométrie est aussi observé sur l'île d'Elbe, en Italie, ou un complexe de neuf laccoliths, exceptionnellement bien conservé, a été étudié en détail par *Rocchi et al.* (2002). De nombreux laccoliths sont aussi marqué par un toit plat, la flexure de l'encaissant ne concernant que les flans du laccolith (*Koch et al.*, 1981).

- Les bysmaliths sont d'imposants volumes cylindriques, préférentiellement composé de roche granitique, discordant (Figure 1.4 f). Ils sont notamment bordés par d'importantes failles quasiment verticales et peuvent atteindre quelques centaines de mètre d'épaisseur (*Johnson and Pollard*, 1973).

A l'instar des batholiths, de nombreuses observations de terrains proposent que les intrusions de taille moyenne se forment aussi par incrément successif de petit volume de magmas (*Habert and De Saint-Blanquat*, 2004; *Horsman et al.*, 2005) (Figure 1.5). Cependant, les même études montrent aussi que ces intrusions se forment sur de petite échelle de temps, une échelle assez petite pour pouvoir garder un corps chaud et liquide des première étape du processus d'intrusion à sa solidification. Au niveau du bysmalith de Black Mesa par exemple (Figure 1.4 f), *Habert and De Saint-Blanquat* (2004) ont

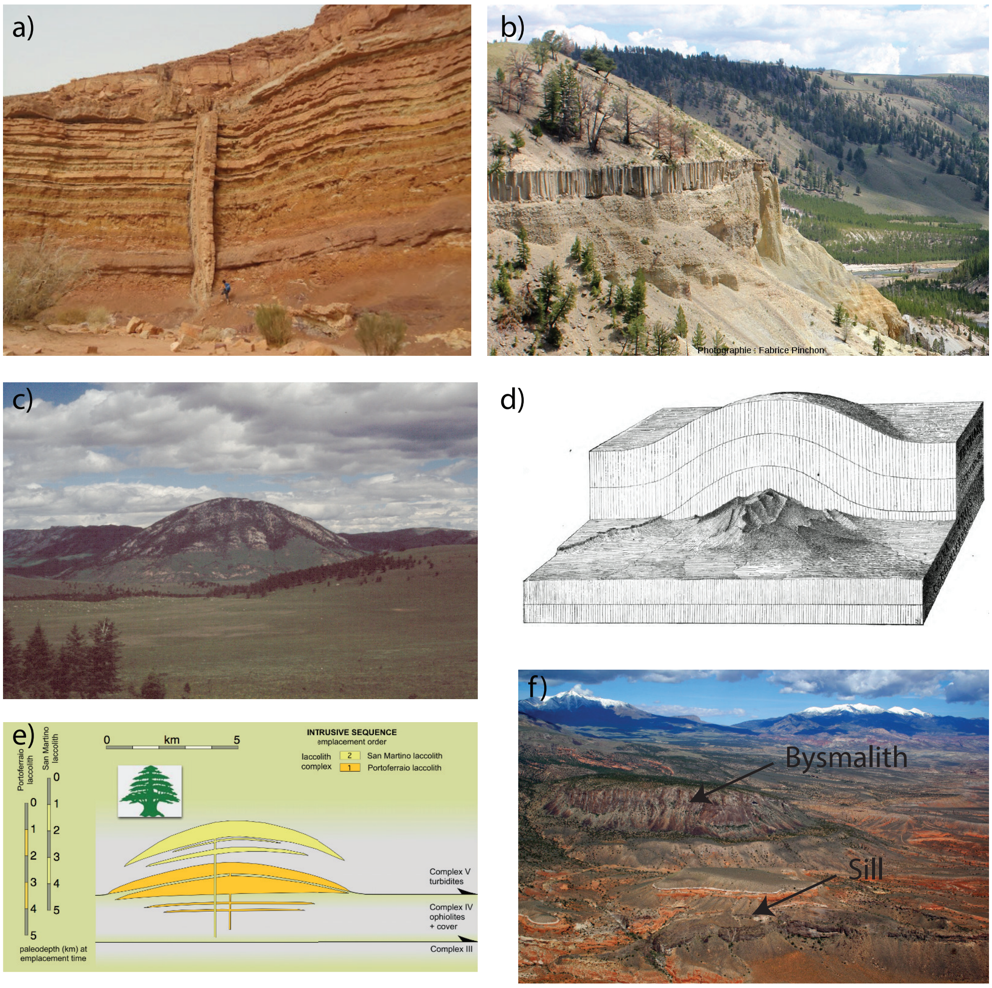

Figure 1.4: a) Dyke traversant des couches sédimentaires dans le Makhtesh Ramon, Israel; b) Sill basaltique au sein de sédiments, vallée de la Yellowstone River, Parc National du Yollowstone (USA). Photographie de Fabrice Pinchon. c) Laccolith à l'érosion dans le Montana d) Schéma de l'emplacement d'un laccolith réalisé par *Gilbert* (1877). e) Schéma simplifié de la structure en arbre de noel d'un complexe de laccolith sur l'île d'elbe, en Italie, étudié par *Rocchi et al.* (2010). f) Intrusions à l'érosion au alentour de la montagne Hillers, dans les Henry Mountains. On peut distinguer le black Mesa bysmalith au centre et le Maiden Creek sill en dessous. Photographie de Jack Share

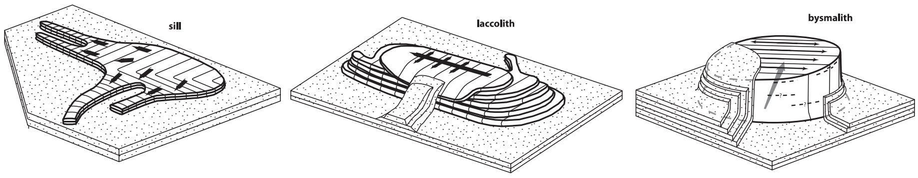

Figure 1.5: Ces diagrammes, réalisés par *Horsman et al.* (2009), montrent la structure verticale en couche de trois intrusions à l'érosion dans les Henry mountains. De gauche a droite: le Maiden Creek sill (Figure 1.4 f), le Trachyte Mesa laccolith et le black mesa bysmalith (Figure 1.4 f).

montré l'absence de structures entre les différentes couches ainsi que l'absence de métamorphisme important dans l'encaissant supposant un temps de mise en place de moins de 100 ans.

1.2.2 Intrusion magmatique sur la Lune

La densité de la croûte lunaire est particulièrement faible, 2550 kg m^{-3} selon les dernières estimations faite à l'aide des donnés gravitaires de la mission GRAIL de la NASA(*Wieczorek et al.*, 2013). La porosité résultante de 4 milliard d'année de bombardement météoritique, qui pourrait être de l'ordre de 12%, ainsi que la faible densité des minéraux la composant, principalement des plagioclases, tous les deux contribuent à sa faible densité. D'autre part, l'épaisseur de la croûte n'est pas négligeable, entre 34 et 43 km en moyenne avec une tendance à être plus épaisse sur la face cachée que sur la face visible.

La faible densité de sa crôute et son épaisseur non négligeable ont certainement joué un rôle important sur le volcanisme lunaire. En effet, les laves extrudés au sein des mers lunaires sont riches en éléments lourd, fer principalement FeO et titan TiO_2, et sont caractérisés par des densités de l'ordre de 3000 kg m^{-3}. La faible densité de la croûte a donc sans doute jouait aussi sur le Lune le rôle d'un filtre efficace à l'extrusion des magmas, formés par fusion partielle de son manteau, en surface, leur flotabilité ne leur permettant pas généralement d'atteindre la surface. *Head and Wilson* (1992) ont estimé ainsi à 50 fois plus important aux volumes extrudé en surface le volume des magmas intrusif sur la lune. Cependant, bien que ce rapport puisse donner de précieuses indications sur l'évolution thermique de la lune elle même, il est de fait très peu contraints. La détection des déformations de surface induites par la mise en place d'intrusion magmatique au sein de la croûte permet une meilleur caractérisation du magmatisme intrusif lunaire.

Deux manifestations principales à la surface de la lune ont été proposé comme potentiellement résultant de la mise en place d'intrusions magmatiques au sein de la croûte lunaire: les domes à faible pente et les cratères au sol fracturé.

- Les domes à faible pente sont localisé en bordure ou dans les mers lunaires, principalement sur la face visible (Figure 1.6 a, b). 13 de ces domes ont été recemment décrit par *Wöhler et al.* (2007). Bien que leur morphologie s'apparente à des laccoliths terrestres, ils sont de manière général beaucoup plus étalés que ceux sur Terre; pour une même épaisseur, l'équivalent lunaire peut ainsi être deux fois plus larges que son homologue Terrestre.

- Les cratères à sol fracturé sont des cratères d'impacts ayant subis des déformations suite à leur formation. A peu près 200 de ces cratères ont été répertorié par *Schultz* (1976), principalement autour des mers lunaires (Figure 1.6 c, d, e, f). La principale caractéristique de ces cratères est leur faible profondeur par rapport à celles des cratères non déformés. En effet, certain cratère au sol fracturé peuvent être jusqu'à 2 km moins profond que leurs homologues non déformées. Leur sol, soit en forme de dôme, soit plat séparé des mures du cratère par un imposant fossé circulaire, est systématiquement caractérisé par d'important réseaux de fractures radiales, concentriques ou encore pentagonales (Figure 1.6 c, d, e, f). Basé sur leur profondeur, topographie et niveau de déformation, *Schultz* (1976) a postuler l'existence de six grandes classe de déformation. La proximité des ces cratères avec les mers lunaire, ainsi que la présence de produits volcaniques au sein de certain cratère, suggèrent qu'ils ont été déformé suite à la mise en place de magma en profondeur sous leur sol.

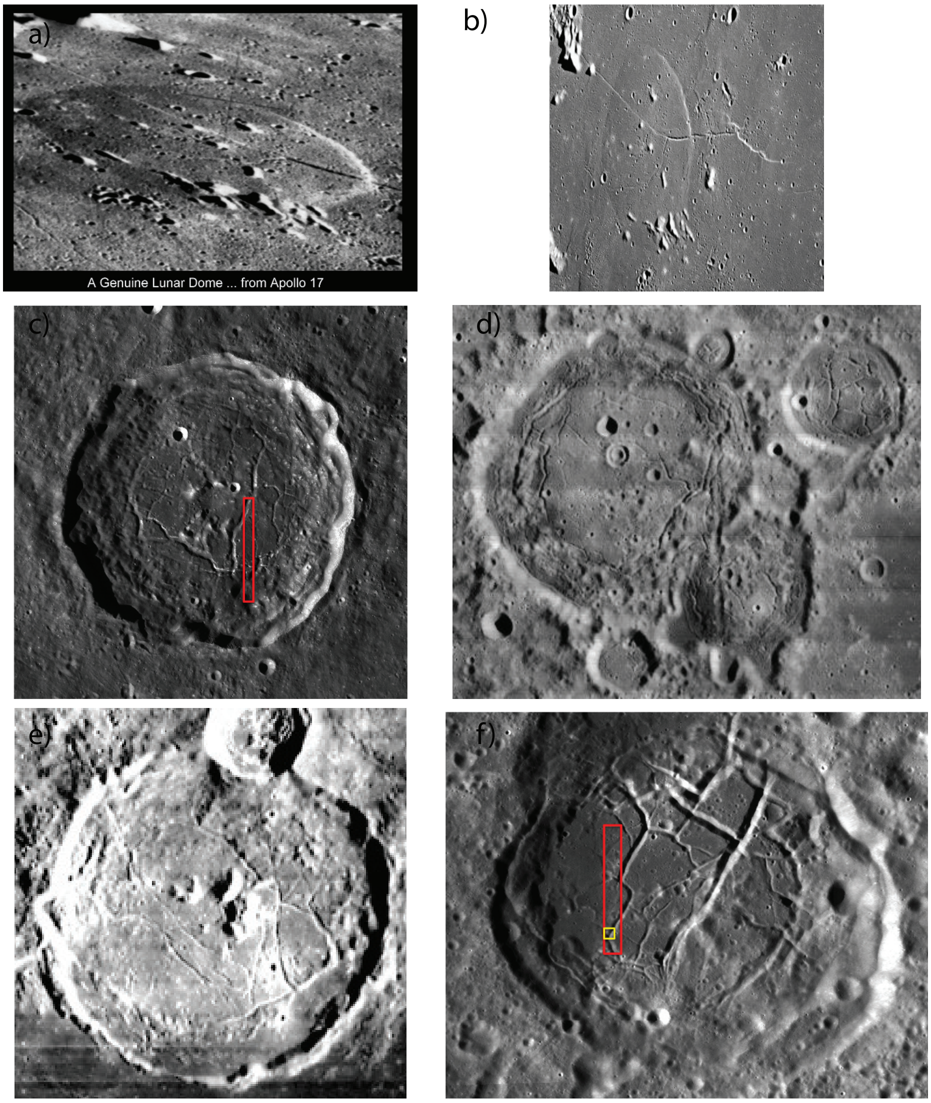

Figure 1.6: a) Dome lunaire, photo par Appolo 17 b) Apollo 15 orbital image AS15-91-12372, vue oblique du dôme Valentine. c) Cratère au sol fracture Atlas (Classe 1). d) Cratère au sol fracturé Lavoisier (Classe 5). e) Cratère au sol fracturé Gassendi (Classe 3). f) Cratère au sol fracturé Komarov (Classe 5). Photo extraite de *Lunar Orbiter Photographic Atlas of the Moon, NASA*

1.2.3 Intrusions magmatiques sur les autres planètes telluriques

1.3 Caractérisation du magmatisme intrusif à faible profondeur: apport de la modélisation

1.3.1 Model statique de déformation d'une couche élastique

Bien que la tailles, la morphologie et les volumes de magmas mise en jeux peuvent être récupérés, à partir d'observations directs ou de méthodes de prospection géophysique sur Terre, ou via les déformations induites à la surface des autres corps du système solaire, ces informations seuls ne donnent que peu d'indication sur les mécanismes de mise en place de ces intrusion magmatiques. En effet, ces observations doivent être interprété sous le regards des modèles d'intrusion magmatiques pour pouvoir extraire des informations sur le processus d'intrusion lui même, i.e. sur les paramètres physiques du magma, les taux d'injection ou encore la profondeur de mise en place.

La propagation d'un dyke dans un milieu élastique a été décrite par (*Lister and Kerr*, 1991; *Rubin*, 1995). En particulier, *Lister* (1990) ont montré que, à l'exeption de la tête du dyke où les contraintes élastiques induites par les roches encaissantes jouent un rôle important, la dynamique du magma au sein du dyke est contrôlée par un équilibre entre la flotabilité et les pertes associées à la viscosité du magma lui même. On a vu qu'un dyke peut se transformer en sill si celui ci rencontre sa zone de flotabilité neutre. La dynamique des dykes et des sills est comparable à forte profondeur (*Lister and Kerr*, 1991; *Cruden et al.*, 2012), cependant, à faible profondeur, la forme des laccoliths supposent que les intrusion magmatiques se mettent en place principalement par flexion des couches sédimentaires sus-jacentes (*Johnson and Pollard*, 1973). Les plupart des travaux modélisant ces intrusions magmatiques utilisent donc la théorie linéaire de l'élasticité qui prédit la flexure d'une plaque élastique en fonction de la contrainte appliqué (le taux d'injection) et des caractéristiques mécaniques de l'encaissant (*Pollard and Johnson*, 1973; *Koch et al.*, 1981). Ces travaux ont par exemple était appliqué à certain laccolith dans les Henry Mountains et pour déduire les profondeur d'intrusion et les taux d'injection nécessaire au niveau des dômes lunaires (*Wöhler et al.*, 2007) et des cratères au sol fracturés (*Jozwiak et al.*, 2012).

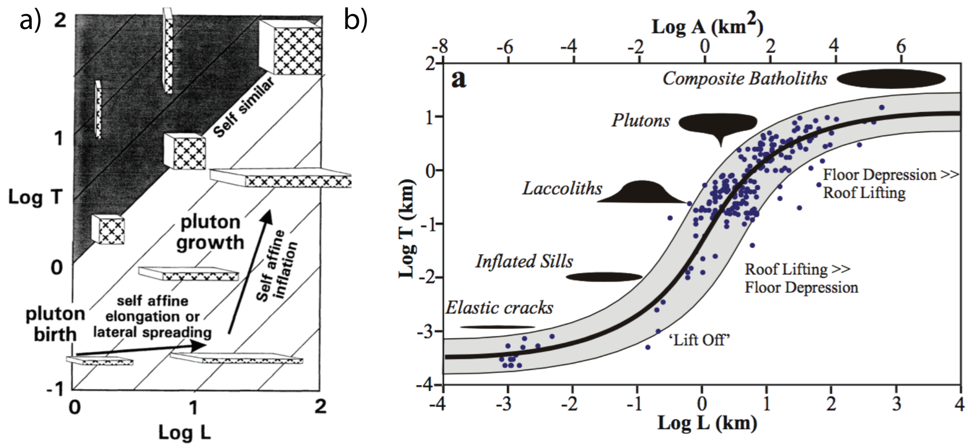

Figure 1.7: a) Schéma de la formation des laccoliths suivant deux étapes par *McCaffrey and Petford* (1997). Nouvelles données: épaisseurs en fonction de leur longueur de différent types d'intrusions magmatiques à différentes locations. Figure extraite de *Cruden et al.* (2012).

1.3.2 Emplacement dynamics des sills et laccoliths: que peut on apprendre de leur géométrie ?

Ces modèles statiques ne fournissent aucune information sur la dynamique du processus d'intrusion et sont donc incapables d'expliquer la diversité des formes observées. De plus, ils négligent la viscosité des magmas ainsi que le propre poids de l'intrusion qui doivent nécessairement jouer un rôle sur la mise en place de l'intrusion. En l'absence d'un modèle dynamique d'intrusion, la géométrie des intrusions répertoriées a été utilisé pour en déduire des indications sur les processus de mise en place et de croissance de ces intrusions. Ainsi, en utilisant les donnés répertoriés sur les laccoliths par *Corry* (1988), *McCaffrey and Petford* (1997) propose une loi de puissance empirique pour l'épaisseur des intrusions h_0 en fonction de leur longueur R, $h_0 = bR^a$ ou a est l'exposant de la loi de puissance et b une constante. Ainsi, un exposant supérieur à 1 indique que l'intrusion croit préférentiellement en s'épaississant et un exposant inférieur à 1 indique qu'elle croit plutôt par étalement.

Les laccoliths répertoriés par (*Corry*, 1988) montrent un exposant $a < 1$ (0.88 ± 0.1) interprété comme reflétant l'étalement de l'intrusion sur une certaine distance sous forme d'un sill avant son épaississement (Figure 1.7). Ce modèle est cohérent avec le modèle couramment accepté pour la mise en place des laccolith en deux étapes (*Johnson and Pollard*, 1973; *McCaffrey and Petford*, 1997). Premièrement, le magma s'étale latéralement au niveau de sa zone de flotabilité neutre $a < 1$ jusqu'à ce qu'un sill soit formé caractérisé par un large rapport d'aspect. Ensuite, lors de la deuxième étape, le sill s'épaissit par flexion des couches sus-jascentes pour former un laccolith caractérisé par $a > 1$ (*Johnson and Pollard*, 1973; *Koch et al.*, 1981). Si la roche sus-jacente est soumise à des contraintes trop importante, des failles se forment au niveaux des bords du sill et celui ci s'épaissit uniformément sur toute sa surface formant un bysmalith (*Corry*, 1988). L'étude détaillée du complexe intrusif de l'île d'Elbe en Italie (Figure **??**) montre des exposants supérieur à 1, jusqu'à 1.5 interprété comme étant le résultat d'une croissance dominé par l'épaississement de l'intrusion.

Des modèles plus récent conçoivent plutôt la formation des laccoliths par empilement successif de sill de grand rapport d'aspect plutôt que par injection d'un volume de magma fini à un temps donné (*Menand*, 2011). En effet, ces modèles sont en accord avec expérience de (*Kavanagh et al.*, 2006) (Section 1.1.3) où les sills se mettent en place à l'interface entre deux couches rigidité différentes, la rigidité de la couche sus-jascente étant plus importante que celle de la couche sous-jascente. En effet, la mise en place d'un sill en refroidissant procure un environnement favorable à la mise en place d'un nouveaux sill, soit au dessus si la rigidité du sill solidifié est inférieur à celle de la roche sus-jascente ou en dessous. Ce modèle de croissance est supporté par de récentes études structurales et stratigraphiques, notamment au niveau des intrusions de taille intermédiaires dans les Henry Mountains (*Horsman et al.*, 2005; *Morgan et al.*, 2008; *Horsman et al.*, 2009; *Menand*, 2011). Ce modèle permet aussi de rendre compte de la structure plate du toit des laccoliths. Cependant, ce mécanisme de croissance ne devrait pas impliquer un exposant caractéristique de la géométrie de ces laccoliths.

Cruden and McCaffrey (2002) ont réunit des donnés sur une plus grande plage de longueurs, des petits cracks élastique de quelques dizaines de mètres aux battholith de quelques centaines de kilomètres (Figure 1.7). (*Cruden and McCaffrey*, 2002) proposent que l'épaisseur en fonction de la longeur des intrusions magmatiques forme une distribution en forme de sigmoide (dans une échelle logarithmique) avec une pente maximum de 1.5 caractéristiques des laccoliths. Cependant, aucune théorie sous-jascente soutient cette observation. De plus, les données de (*Cruden et al.*, 2012) sur les larges sills mafiques contredise cette vision des choses (Figure 1.3).

1.4 Discussion

En conclusion, aucun des modèles présentés plus haut n'est cohérent à la fois avec la morphologie des sills et des laccoliths et leurs rapport d'aspect. Dans le but de comprendre plus en détails la dynamique de l'intrusion, *Michaut*

(2011) a développé un modèle théorique d'étalement d'un magma visqueux sous une couche élastique d'épaisseur contant continuellement nourrit par un conduit vertical en son centre. Ce modèle diffère de ces prédecesseurs par sa capacité a traité la dynamique même de l'intrusion ainsi que le poids du magma comme un moteur de l'écoulement. Ce modèle a été développé en 2D par (*Thorey and Michaut*, 2014). Dans la suite, je présente le modèle et les résultats que nous avons obtenus dans une géométrie axisymmétrique.

Bibliography

Anderson, E. M. (1951), The dynamics of faulting and dyke formation with applications to Britain. (Not cited.)

Clemens, J. D., and C. K. Mawer (1992), Granitic magma transport by fracture propagation, *Tectonophysics*, *204*(3-4), 339–360. (Not cited.)

Corry, C. E. (1988), Laccoliths: mechanics of emplacement and growth. (Not cited.)

Crisp, J. A. (1984), Rates of magma emplacement and volcanic output, *Journal of Volcanology and Geothermal Research*, *20*(3-4), 177–211. (Not cited.)

Cruden, A., and K. McCaffrey (2002), First international workshop on the-Physical Geology of Subvolcanic Systems – Laccoliths, Sills, and Dykes, in *LASI 1*, pp. 8–11. (Not cited.)

Cruden, A., A. Bunger, and S. Morgan (2012), Emplacement dynamics of laccoliths, sills and dykes from dimensional scaling and mechanical models, in *LASI 1*. (Not cited.)

Gilbert, G. K. (1877), Report on the Geology of the Henry Mountains , Government Printing Office, Washington, DC. (Not cited.)

Glazner, A. F., J. M. Bartley, D. S. Coleman, W. Gray, and R. Z. Taylor (2004), Are plutons assembled over millions of years by amalgamation from small magma chambers?, *GSA Today*, *14*(4), 4–8. (Not cited.)

Habert, G., and M. De Saint-Blanquat (2004), Rate of construction of the Black Mesa bysmalith, Henry Mountains, Utah, *Geological Society*. (Not cited.)

Head, J. W., and L. Wilson (1992), Lunar mare volcanism: Stratigraphy, eruption conditions, and the evolution of secondary crusts, *Geochimica et Cosmochimica Acta*, *56*(6), 2155–2175. (Not cited.)

Horsman, E., B. Tikoff, and S. Morgan (2005), Emplacement-related fabric and multiple sheets in the Maiden Creek sill, Henry Mountains, Utah, USA, *Journal of Structural Geology*, *27*(8), 1426–1444. (Not cited.)

Horsman, E., S. Morgan, M. de Saint-Blanquat, G. Habert, A. Nugent, R. A. Hunter, and B. Tikoff (2009), Emplacement and assembly of shallow intrusions from multiple magma pulses, Henry Mountains, Utah, *100*(1-2), 117–132. (Not cited.)

Johnson, A. M., and D. D. Pollard (1973), Mechanics of growth of some laccolithic intrusions in the Henry mountains, Utah, I: field observations, Gilbert's model, physical properties and flow of the magma, *Tectonophysics*. (Not cited.)

Jozwiak, L. M., J. W. Head, M. T. Zuber, D. E. Smith, and G. A. Neumann (2012), Lunar floor-fractured craters: Classification, distribution, origin and implications for magmatism and shallow crustal structure, *J. Geophys. Res.*, *117*(E11), E11,005. (Not cited.)

Kavanagh, J. L., T. Menand, and R. S. J. Sparks (2006), An experimental investigation of sill formation and propagation in layered elastic media, *Earth and Planetary Science Letters*, *245*(3-4), 799–813. (Not cited.)

Koch, F. G., A. M. Johnson, and D. D. Pollard (1981), Monoclinal bending of strata over laccolithic intrusions, *Tectonophysics*, *74*(3-4), T21–T31. (Not cited.)

Lister, J. R. (1990), Buoyancy-driven fluid fracture: the effects of material toughness and of low-viscosity precursors, *J. Fluid Mech.*, *210*(-1), 263–280. (Not cited.)

Lister, J. R., and R. C. Kerr (1991), Fluid-mechanical models of crack propagation and their application to magma transport in dykes, *Journal of Geophysical Research: Solid ...*, *96*(B6), 10,049–10,077. (Not cited.)

McCaffrey, K., and N. Petford (1997), Are granitic intrusions scale invariant?, *Journal of the Geological Society*, *154*(1), 1–4. (Not cited.)

McKenzie, D. (1984), The Generation and Compaction of Partially Molten Rock, *Journal of Petrology*, *25*(3), 713–765. (Not cited.)

McKenzie, D. (1985), The extraction of magma from the crust and mantle, *Earth and Planetary Science Letters*, *74*(1), 81–91. (Not cited.)

Menand, T. (2011), Physical controls and depth of emplacement of igneous bodies: A review, *Tectonophysics*, *500*(1-4), 11–19. (Not cited.)

Michaut, C. (2011), Dynamics of magmatic intrusions in the upper crust: Theory and applications to laccoliths on Earth and the Moon, *J. Geophys. Res.*, *116*(B5), B05,205. (Not cited.)

Miller, R. B., and S. R. Paterson (1999), In defense of magmatic diapirs, *Journal of Structural Geology*, *21*(8-9), 1161–1173. (Not cited.)

Morgan, S., A. Stanik, E. Horsman, B. Tikoff, M. de Saint-Blanquat, and G. Habert (2008), Emplacement of multiple magma sheets and wall rock deformation: Trachyte Mesa intrusion, Henry Mountains, Utah, *Journal of Structural Geology*, *30*(4), 491–512. (Not cited.)

Petford, N., R. C. Kerr, and J. R. Lister (1993), Dike transport of granitoid magmas, *Geology*, *21*(9), 845–848. (Not cited.)

Petford, N., A. R. Cruden, K. McCaffrey, and J. L. Vigneresse (2000), Granite magma formation, transport and emplacement in the Earth's crust, *Nature*, *408*(6813), 669–673. (Not cited.)

Pinel, V., and C. Jaupart (2000), The effect of edifice load on magma ascent beneath a volcano, ... *Transactions of the Royal* .... (Not cited.)

Pinel, V., and C. Jaupart (2004), Magma storage and horizontal dyke injection beneath a volcanic edifice, *Earth and Planetary Science Letters*, *221*(1-4), 245–262. (Not cited.)

Pollard, D. D., and A. M. Johnson (1973), Mechanics of growth of some laccolithic intrusions in the Henry Mountains, Utah, II: bending and failure of overburden layers and sill formation, *Tectonophysics*, *18*(3-4), 311–354. (Not cited.)

Rocchi, S., D. S. Westerman, A. Dini, F. Innocenti, and S. Tonarini (2002), Two-stage growth of laccoliths at Elba Island, Italy, *Geology*, *30*(11), 983–986. (Not cited.)

Rocchi, S., D. S. Westerman, A. Dini, and F. Farina (2010), Intrusive sheets and sheeted intrusions at Elba Island, Italy, *Geosphere*. (Not cited.)

Roman, A., and C. Jaupart (2014), The impact of a volcanic edifice on intrusive and eruptive activity, *Earth and Planetary Science Letters*, *408*(C), 1–8. (Not cited.)

Rubin, A. M. (1995), Propagation of magma-filled cracks, *Annual Review of Earth and Planetary Sciences*. (Not cited.)

Schultz, P. H. (1976), Floor-fractured lunar craters, *The Moon*, *15*(3-4), 241–273. (Not cited.)

Taisne, B., and S. Tait (2009), Eruption versus intrusion? Arrest of propagation of constant volume, buoyant, liquid-filled cracks in an elastic, brittle host, *J. Geophys. Res.*, *114*(B6), B06,202. (Not cited.)

Taisne, B., S. Tait, and C. Jaupart (2011), Conditions for the arrest of a vertical propagating dyke, *Bull Volcanol*, *73*(2), 191–204. (Not cited.)

Tarbuck, E. J., F. J. Lutgens, and D. Tassa (1998), *Earth: An Introduction to Physical Geology*, vol. 11, Pearson. (Not cited.)

Thorey, C., and C. Michaut (2014), A model for the dynamics of crater-centered intrusion: Application to lunar floor-fractured craters, *J. Geophys. Res. Planets*, *119*(1), 286–312. (Not cited.)

Walker, G. P. L. (1989), Gravitational (density) controls on volcanism, magma chambers and intrusions, *Australian Journal of Earth Science*, *36*(2), 149–165. (Not cited.)

Weinberg, R. F. (1996), Ascent mechanism of felsic magmas: news and views, *Geological Society of America Special ...*. (Not cited.)

Weinberg, R. F., and Y. Podladchikov (1994), Diapiric ascent of magmas through power law crust and mantle, *J. Geophys. Res.*, *99*(B5), 9543–9559. (Not cited.)

White, S. M., J. A. Crisp, and F. J. Spera (2006), Long-term volumetric eruption rates and magma budgets, *Geochem. Geophys. Geosyst.*, *7*(3), Q03,010–21. (Not cited.)

Wieczorek, M. A., G. A. Neumann, F. Nimmo, W. S. Kiefer, G. J. Taylor, H. J. Melosh, R. J. Phillips, S. C. Solomon, J. C. Andrews-Hanna, S. W. Asmar, A. S. Konopliv, F. G. Lemoine, D. E. Smith, M. M. Watkins, J. G. Williams, and M. T. Zuber (2013), The crust of the Moon as seen by GRAIL, *Science*, *339*(6120), 671–675. (Not cited.)

Wöhler, C., R. Lena, and J. Phillips (2007), Formation of lunar mare domes along crustal fractures: Rheologic conditions, dimensions of feeder dikes, and the role of magma evolution, *Icarus*, *189*(2), 279–307. (Not cited.)

Chapter 2

Isoviscous elastic-plated gravity current model for shallow magmatic intrusion

Contents

Michaut (2011) proposed a new model for the spreading of a shallow depth intermediate-size intrusions, where magma is continuously injected at the center and is accommodated by the bending of the overlying strata. In particular, the model differs from previous ones by considering the dynamics of the emplacement itself, in a sense that the radius in self-consistently determined, and the driving force associated with the magma weight which were both neglected in older models. In the original paper from *Michaut* (2011), the model was derived in both cartesian and axisymmetric geometry and the results were presented in 2D. A similar model in $2D$ with an additional fracture criterion at the tip of the intrusion has been derived by *Bunger and Cruden* (2011) and *Hewitt et al.* (2014) discussed precisely the dynamics at the contact line and the case of an elastic-plated gravity current spreading over an inclined plane (*Hewitt et al.*, 2014). In this chapter, we present a summary of the model and the results for the spreading of an isoviscous elastic-plated gravity current over a rigid horizontal surface in an axisymmetrical geometry. Results in this geometry have been thoroughly studied by *Lister et al.* (2013) and this model will constitute the reference for more elaborate models in the manuscript.

2.1 Model

The model considers an isoviscous elastic-plated gravity current, i.e. an isoviscous fluid of viscosity η_h and density ρ_m spreading beneath a thin elastic sheet of thickness d_c and above a semi infinite rigid layer (*Michaut*, 2011; *Bunger and Cruden*, 2011) (Figure 2.1). The fluid is injected continuously at the base and center of the current at a rate Q_0 through a cylindrical conduit of diameter a.

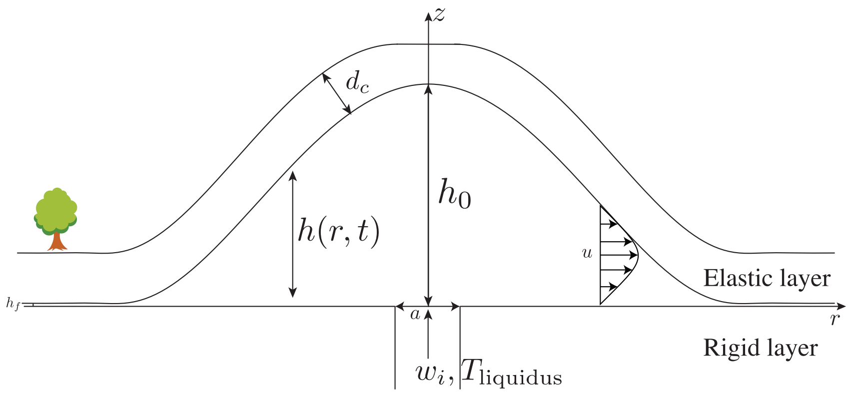

Figure 2.1: Model geometry and parameters.

2.1.1 Governing equation

Driving pressure

The intrusion develops over a length scale Λ that is much larger than its thickness H ($\varepsilon = H/\Lambda << 1$). In the laminar regime and in axisymmetrical coordinates (r,z), the Navier-stokes equations within the lubrication assumption are

$$-\frac{\partial P}{\partial r} + \frac{\partial}{\partial z}\left(\eta \frac{\partial u}{\partial z}\right) = 0 \tag{2.1}$$

$$-\frac{\partial P}{\partial z} - \rho_m g = 0 \tag{2.2}$$

where $u(r, z, t)$ is the radial velocity, g is the standard acceleration due to gravity and $P(r, z, t)$ is the pressure within the fluid. Integration of (2.2) thus gives the total pressure $P(r, z, t)$ within the flow. When the vertical deflection deflection $h(r, t)$ of the upper elastic layer is small compared to its thickness d_c, i.e $h << d_c$, we can neglect stretching of the upper layer and only consider bending stresses. Therefore, the total pressure $P(r, z, t)$ at a level z in the intrusion is the sum of four contributions: the weight of the magma and of the upper layer, the bending pressure P_b and the atmospheric pressure P_0

$$P = \rho_m g(h - z) + \rho_r g d_c + P_b + P_0 \tag{2.3}$$

where $h(r, t)$ is the intrusion thickness and ρ_r the density of the surrounding rocks. The bending pressure is given by the force per unit area that is necessary for a vertical displacement h of the thin elastic plate (*Turcotte and Schubert*, 1982)

$$P_d = D\nabla^4 h \tag{2.4}$$

where D is the flexural rigidity of the thin elastic layer, that depends on the Young's modulus E, Poisson's ratio ν^* and on the elastic layer thickness d_c as $D = Ed_c^3/\left(12(1 - \nu^*)\right)$.

Velocity field

At the contact with the elastic sheet $z = h(r, t)$, the no-slip boundary condition is present and so, the tangential velocity is zero and the normal velocity is the change in height $(\partial h/\partial t)$. With $\vec{n}$ the normal to the surface and $\vec{t}$ the tangent, we have

$$\vec{n} \cdot (u, w) = \frac{\partial h}{\partial t} \tag{2.5}$$

$$\vec{t} \cdot (u, w) = 0. \tag{2.6}$$

The tangent vector is $\vec{t} = (1, \partial h/\partial r)$. However, within the lubrication assumption, the vertical component of the tangent vector scales as ε and thus, is negligible compared to the radial component. Therefore, the boundary condition (2.6) reduces to $u(r, z = h, t) = 0$. At the base of the flow, the same boundary condition hold and $u(r, z = 0, t) = 0$.

Equation (2.1) is integrated twice as a function of z using these boundary conditions and the horizontal velocity is

$$u(r, z, t) = \frac{1}{2\eta}\frac{\partial P}{\partial r}\left(z^2 - hz\right) \tag{2.7}$$

Injection rate

The effective overpressure ΔP^* driving the flow in the feeder conduit decreases as the intrusion thickens and is given by

$$\Delta P^* = \Delta P - \rho_m g h_0 \tag{2.8}$$

where $h_0(t)$ is the maximum intrusion thickness at the center $r = 0$ and ΔP is the initial driving pressure or the overpressure at the base of the dyke ($z = -Z_c$).

In (2.8), the bending pressure at then center, which scale as $\mathrm{D}h_0(t)/R(t)^4$ where $R(t)$ is the blister radius, has been neglected. Although it tends to infinity at the initiation of the flow, it rapidly vanishes as the blister spreads and the hydrostatic pressure $\rho_m g h_0$ becomes the main contribution to the pressure at the center. In addition, the model assumes a large aspect ratio for the blister and does not consider the initiation of the flow.

Finally, assuming a Poiseuille flow within the cylindrical feeding conduit, the vertical injection velocity $w_i(r,t)$ and injection rate $Q(t)$ are given by

$$w_i = \begin{cases} \frac{\Delta P^*}{4\mu Z_c}(\frac{a^2}{4} - r^2) & r \leq \frac{a}{2} \\ 0 & r > \frac{a}{2} \end{cases} \tag{2.9}$$

$$Q = Q_0(1 - \frac{\rho_m g h_0}{\Delta P}) \tag{2.10}$$

where $Q_0 = (\pi \Delta P^* a^4) \,/\, (128 \eta Z_c)$.

Mass conservation

The fluid is assumed incompressible and a global statement of mass conservation gives

$$\frac{\partial h}{\partial t} + \frac{1}{r}\frac{\partial}{\partial r}\left(r \int_0^h u dz\right) = w_i \tag{2.11}$$

and using (2.7), we find that the equation for the evolution of the thickness in time and space reads

$$\frac{\partial h}{\partial t} = \frac{\rho_m g}{12\eta r}\frac{\partial}{\partial r}\left(r h^3 \frac{\partial h}{\partial r}\right) + \frac{D}{12\eta r}\left(r h^3 \frac{\partial}{\partial r}\nabla^4 h\right) + w_i. \tag{2.12}$$

It is composed of three different terms on the right hand side. The first term represents gravitational spreading, i.e. spreading of the blister under its own weight. The second term represents the squeezing of the flow by the upper elastic layer. Both term are negative and induces spreading. The last term represents fluid injection and is positive.

2.1.2 Dimensionless equations

Equations (3.78) and (2.12) are nondimensionalized using a horizontal scale Λ, a vertical scale H and a time scale τ given by

$$\Lambda = \left(\frac{D}{\rho_m g}\right)^{1/4} \tag{2.13}$$

$$H = \left(\frac{12\eta Q_0}{\rho_m g \pi}\right)^{\frac{1}{4}} \tag{2.14}$$

$$\tau = \frac{\pi \Lambda^2 H}{Q_0} \tag{2.15}$$

where scales are chosen such that $Q_0 = \pi\Lambda^2 H/\tau$. The length scale represents the flexural wavelength of the upper elastic layer, i.e. the length scale at which bending stresses and gravity contributes equally to flow. The height scale H is the thickness of a typical gravity current and the time scale τ is the characteristic time to fill up a cylindrical flow of radius Λ and thickness H at constant rate Q_0. In addition, we can define a horizontal velocity scale $U = \Lambda/\tau = (\rho_m g H^3)\,/\,(12\eta_h \Lambda)$.

The dimensionless equation is

$$\begin{aligned}\frac{\partial h}{\partial t} &= \frac{1}{r}\frac{\partial}{\partial r}\left(rh^3\frac{\partial h}{\partial r}\right) + \frac{1}{r}\left(rh^3\frac{\partial}{\partial r}\nabla^4 h\right)\\ &+ \frac{32}{\gamma^2}\left(\frac{1}{4} - \frac{r^2}{\gamma^2}\right)\left(1 - \frac{h_0}{\sigma}\right)\end{aligned} \tag{2.16}$$

where the last term is replaced by zero for $r > \gamma/2$. γ and σ are two dimensionless numbers that control the dynamics of the flow

$$\gamma = \frac{a}{\Lambda} \tag{2.17}$$

$$\sigma = \frac{\Delta P}{\rho_m g h}. \tag{2.18}$$

γ is the dimensionless radius of the conduit, it does not significantly influence the flow and is set to 0.02 in the following (*Michaut and Bercovici*, 2009; *Michaut*, 2011). σ is the normalized pressure head, i.e., the ratio between the initial overpressure driving the flow and the weight of the magma at the center.

2.1.3 Need for regularization

One of the main mathematical difficulty in solving equation (2.16) arises at the contact line. Indeed, the assumption that the thickness of the fluid tends to zero at the contact line leads to divergent viscous stresses, i.e. $\eta \partial u/\partial z \to \infty$ and hence, the theoretical immobility of the blister (*Flitton and King*, 2004; *Lister et al.*, 2013; *Hewitt et al.*, 2014). This problem, known a the contact-line paradox, is a well know problem for surface-tension driven flow such as the spreading of a water droplet (*Bertozzi*, 1998; *Snoeijer and Andreotti*, 2013).

The formal proof have been derived by *Flitton and King* (2004) and can be derived as follow. Suppose that (2.16) has a solution and the solution has the form $h \sim A(t)(R(t)-r)^{\alpha}$ near the contact line. As $r \to R(r)$, the bending term dominates the gravitational term and (2.16) reduces to

$$\frac{\partial h}{\partial t} = \frac{1}{r}\frac{\partial}{\partial r}\left(rh^3\frac{\partial}{\partial r}\nabla^4 h\right). \tag{2.19}$$

Injecting the solution into (2.19) and keeping only the leading powers of $R-r$ gives

$$\begin{aligned}\frac{\partial R}{\partial t}A\alpha\left(R-r\right)^{\alpha-1}+\frac{\partial A}{\partial t}\left(R-r\right)^{\alpha} &= A^4\alpha(\alpha-1)(\alpha-2)\\ &\quad(\alpha-3)(\alpha-4)(\alpha-5)(R-r)^{4\alpha-6}\end{aligned}$$

The time derivative is locally dominated by its convective part at the tip, the second term on the left is small compared to the first and therefore, by equating the exponent of $R-r$, we obtain $\alpha = 5/3$, and by equating the coefficients, we deduce

$$\frac{\partial R}{\partial r} = -\frac{280}{243}A^3. \tag{2.20}$$

It shows that (2.16) can only have retreating contact line ($dR/dt < 0$) but not with advancing contact line ($dR/dt > 0$) (*Lister et al.*, 2013; *Flitton and King*, 2004).

To mitigate this problem, one common approach is to add a thin prewetting film, with thickness h_f such that $h \to h_f$ as $r \to \infty$. While the solution will depend upon the prewetting film thickness h_f and will not show any convergence properties when $h_f \to 0$, we will see that the dependence in h_f is weak and the difference between different values for h_f will be relatively small (*Lister et al.*, 2013; *Hewitt et al.*, 2014). Unless otherwise specified, we will consider $h_f = 5 \cdot 10^{-3}$ in the manuscript.

2.2 Results

For a small prewetting film thickness, i.e. $h_f/H << 1$, the numerical resolution of the equation (3.25) shows three spreading regimes: a bending regime where gravity is negligible, a viscous gravity current regime where bending is negligible and a regime of lateral propagation (*Michaut*, 2011; *Bunger and Cruden*, 2011; *Lister et al.*, 2013).

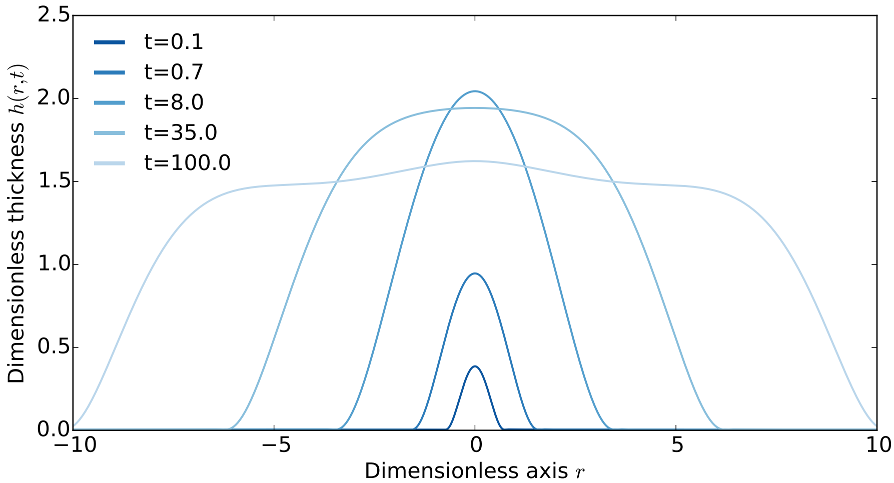

Figure 2.2: Shape of the flow, i.e. thickness $h(r,t)$ as a function of the radial axis r at five different times indicated on the plot. Variables are dimensionless and one needs to multiply by the characteristic scales (thickness, length or time given by (3.23), (3.22) or (3.24)) to obtain dimensional values. For $t < 10$, the intrusion is in the bending regime whereas for $t > 10$ the intrusion is in the gravity current regime.

2.2.1 Bending regime

At early times, when $R << \Lambda$, gravity is negligible and the dynamics of the spreading is governed by the bending of the upper layer. In addition, if $h_0 << \sigma$, the overpressure ΔP driving the flow is much larger than the weight of the blister at the center and the injection rate can be considered constant.

In that case, the spreading is very slow and the interior has uniform pressure $P = \nabla^4 h$. The flow is bell-shaped and its thickness is given by

$$h(r,t) = h_0(t)\left(1 - \frac{r^2}{R^2(t)}\right)^2 \tag{2.21}$$

with $h_0(t)$ the thickness of the intrusion at the center (*Michaut*, 2011; *Lister et al.*, 2013). In this regime, *Lister et al.* (2013) have shown that the spreading is controlled by the propagation of a peeling by bending wave at the intrusion front with dimensionless velocity c

$$c = \frac{\partial R}{\partial t} = h_f^{1/2}\left(\frac{\kappa}{1.35}\right)^{5/2} \tag{2.22}$$

where $\kappa = \partial^2 h/\partial r^2$ is the dimensionless curvature of the interior solution. Using the propagation law (3.50) and the form of the interior solution (3.49),

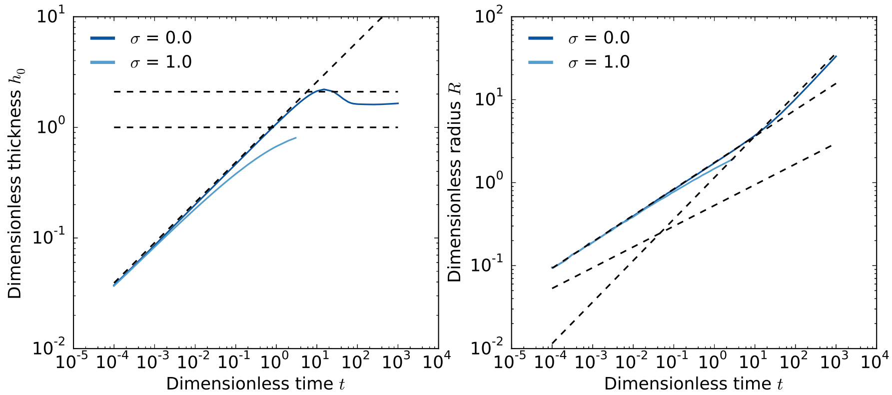

Figure 2.3: Left: Dimensionless thickness at the center h_0 versus dimensionless time t for different dimensionless number σ indicated on the plot. Dashed-lines represent the scaling laws in the different regimes. Right: Dimensionless radius R versus dimensionless time t for the same dimensionless number σ. Dashed-lines represent the scaling laws in the different regimes.

they find that the radius and the height of the intrusion are given by similarity solutions

$$R(t) = 2.2h_f^{1/22}t^{7/22} \tag{2.23}$$

$$h_0(t) = 0.7h_f^{-1/11}t^{8/22}. \tag{2.24}$$

where the numerical pre-factor have been matched to our simulations.

2.2.2 Gravity current regime

In contrast, when the radius R becomes much larger than Λ ($R >> \Lambda$), the weight of the intrusion becomes dominant over the bending terms. The pressure is given by the hydrostatic pressure $P = h$ and the intrusion enters a classical viscous gravity current regime where bending terms only affect the solution near the intrusion edge (*Huppert*, 1982; *Michaut*, 2011; *Lister et al.*, 2013). In this second regime, the radius evolves as $t^{1/2}$ and the thickness tends to a constant

$$R(t) = 0.715t^{1/2} \tag{2.25}$$

$$h_0 = 1.86 \tag{2.26}$$

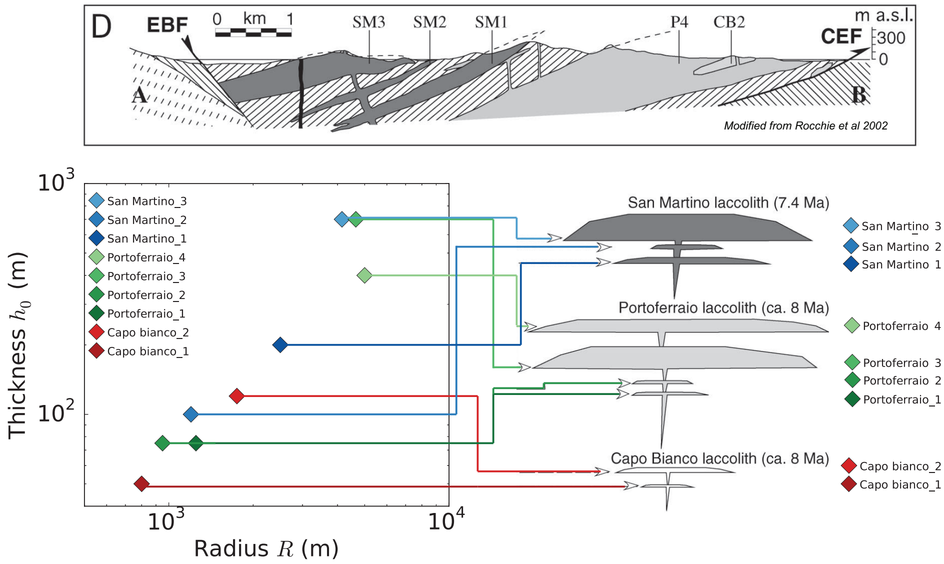

Figure 2.4:

2.2.3 Lateral propagation

Once $h_0 \to \sigma$, the flow is thick enough to compensate for the initial overpressure. The thickness at the center remains constant and the flow enters a regime of lateral propagation, where only its radius $R(t)$ is to increase (*Michaut*, 2011). In this regime, except at the center when it redistributes the pressure over a length scale Λ, the bending term is negligible compared to the gravitational term. *Michaut* (2011) has shown that in this regime, the thickness is constant and the radius evolves as $t^{1/4}$

$$R(t) = \left(\frac{\sigma^3 t}{4\pi}\right)^{1/4} \tag{2.27}$$

$$h_0 = \sigma \tag{2.28}$$

2.3 Application to laccoliths

In the following, we apply the isoviscous-gravity current.

2.4 Discussion

Table 2.1: Range of values for the model parameters

Parameters	Symbol	Range of values	Unit
Depth of intrusion	d_c	$0.1 - 5$	km
Young's Modulus	E	$10 - 100$	GPa
Poisson's ratio	ν^*	0.25	
Gravity	g	9.81	m s^{-2}
Magma density	ρ_m	$2800 - 3200$	kg m^{-3}
Magma viscosity	η	$1 - 10^4$	Pa s
Feeder dyke width	a	$1 - 100$	m
Depth of the melt source	Z_c	$5 - 500$	km
Initial overpressure	ΔP	$5 - 50$	MPa
Injection rate	Q_0	$10p{-}3 - 0.1$	m^3 s^{-1}
Crust density	ρ_r	2500	kg m^{-3}
Characteristic scales	**Symbol**	**Range of values**	**Unit**
Height scale	H	$0.1 - 10$	m
Length scale	Λ	$1 - 12$	km
Time scale	τ	$10^{-1} - 10$	years

Table 2.2: Dimensionless numbers

		Complex craters	Simple craters
Symbol	Description	Range of values	Range of values
γ	Normalized source width	$10^{-4} - 10^{-2}$	$10^{-4} - 10^{-2}$
ζ	Normalized wall zone width	$0.05 - 0.13$	0.25
Ψ	Thickening term	$0.3 - 8$	$0.2 - 4$
Ξ	Hydrostatic term	$20 - 400$	$20 - 200$
Θ	Elastic term	$10^{-7} - 0.1$	$10^{-3} - 10$
Ω	Density ratio	1.2	1.2
Φ	Upper layer aspect ratio	4500	1200
σ	Normalized pressure head	$0.6 - 100$	$0.6 - 100$

Bibliography

Bertozzi, A. L. (1998), The mathematics of moving contact lines in thin liquid films, *Notices AMS*. (Not cited.)

Bunger, A. P., and A. R. Cruden (2011), Modeling the growth of laccoliths and large mafic sills: Role of magma body forces, *J. Geophys. Res.*, *116*(B2), B02,203. (Not cited.)

Flitton, J. C., and J. R. King (2004), Moving-boundary and fixed-domain problems for a sixth-order thin-film equation, *European Journal of Applied Mathematics*, *15*(06), 713–754. (Not cited.)

Hewitt, I. J., N. J. Balmforth, and J. R. De Bruyn (2014), Elastic-plated gravity currents, pp. 1–29. (Not cited.)

Huppert, H. E. (1982), The propagation of two-dimensional and axisymmetric viscous gravity currents over a rigid horizontal surface, *J. Fluid Mech.*, *121*(-1), 43–58. (Not cited.)

Lister, J. R., G. G. Peng, and J. A. Neufeld (2013), Viscous Control of Peeling an Elastic Sheet by Bending and Pulling, *Phys. Rev. Lett.*, *111*(15), 154,501. (Not cited.)

Michaut, C. (2011), Dynamics of magmatic intrusions in the upper crust: Theory and applications to laccoliths on Earth and the Moon, *J. Geophys. Res.*, *116*(B5), B05,205. (Not cited.)

Michaut, C., and D. Bercovici (2009), A model for the spreading and compaction of two-phase viscous gravity currents, *J. Fluid Mech.*, *630*, 299–329. (Not cited.)

Snoeijer, J. H., and B. Andreotti (2013), Moving Contact Lines: Scales, Regimes, and Dynamical Transitions, *Annu. Rev. Fluid Mech.*, *45*(1), 269–292. (Not cited.)

Turcotte, D. L., and G. Schubert (1982), Geodynamics: Applications of continuum physics to geological problems, John Wiley, New York. (Not cited.)

Part II

Evolution thermique des intrusions magmatiques ible profondeur

Chapter 3

Elastic-plated gravity current with temperature-dependent viscosity

Contents

Temperature-dependent elastic-plated gravity current has numerous applications in the nature science, from the intrusion of magma is the shallow layer of the crust to the flowing of melt-water below ice sheet. We develop the general equations for the elastic-plated gravity current with temperature-dependent viscosity for constant influx conditions. Crystallization is also taken into account as a source/sink of heat when the fluid crystallizes/melts during emplacement. We show that the coupling between the thermal structure and the flow itself results in important deviations from the isoviscous case. In particular, both regimes, taken individually, split in three phases. In the first phase, the thermal anomaly has the size of the current itself, the effective viscosity is minimal and the current spreads as in the isoviscous case. The second phase is triggered by the detachment of the thermal anomaly and followed by an important increase in the effective viscosity of the flow. The current slows down and thickens. Finally, when the cold front region becomes about 10% of the flow itself, the effective viscosity stabilizes to its maximum value and the current return in an isoviscous dynamics, but with cold viscosity. Further analyses show that the effective viscosity is the average viscosity of a small region a the front of the current in the bending regime and the average viscosity of the current in the gravity regime. Therefore, the evolution of an elastic-plated gravity current depends on the relative phase changes within the two regime and the transition between the two regime itself. Application to terrestrial laccolith, which is a major process in the crust formation, show that they should preferentially solidify in the third phase of the bending regime.

3.1 Introduction

Elastic-plated gravity currents involve the spreading of viscous material beneath an elastic sheet. The applications range from the emplacement of lava in the shallow crust (*Michaut*, 2011; *Bunger and Cruden*, 2011) and melt-water drainage below ice sheet (*Das et al.*, 2008; *Tsai and Rice*, 2010) in geological setting to the the manufacture of flexible electronics and microelectromechanical systems (MEMS) in engineering (*Hosoi and Mahadevan*, 2004).

When the thickness of the flow is small compared to its extent, lubrication approximation applies and the study of elastic-plated gravity currents resumes to the study of a sixth order, non-linear partial differential equation (*Michaut*, 2011; *Lister et al.*, 2013; *Hewitt et al.*, 2014) . However, the assumption that the thickness of the fluid tends to zero at the contact line leads to divergent viscous stresses, and hence, the need of a regularization condition at the front (*Flitton and King*, 2004; *Lister et al.*, 2013; *Hewitt et al.*, 2014). One common approach is to add a thin pre-wetted film of fluid, thus avoiding the requirement for any boundary conditions at a genuine contact line (*Lister et al.*, 2013; *Hewitt et al.*, 2014).

The dynamics of the spreading has been described in an axisymmetric geometry for a Newtonian fluid with constant viscosity (*Michaut*, 2011; *Lister et al.*, 2013; *Thorey and Michaut*, 2014). In particular, they show the presence of two distinct regimes of evolution. First, gravity is negligible and the peeling of the front is driven by bending; the interior is bell-shaped, the radius evolves as $t^{8/22}$ and the thickness evolves as $t^{7/22}$. When the radius becomes larger 4Λ, where Λ is the flexural wavelength of the upper layer, the weight of the current becomes dominant over the bending terms and the evolution enters a gravity current regime (*Huppert*, 1982a). In this second regime, the thickness profile shows a flat top with bent edges, the radius evolves as $t^{1/2}$ and the thickness tends to a constant. Different analogue experiments of isoviscous flows confirm these theoretical results (*Dixon and Simpson*, 1987; *Lister et al.*, 2013).

However, in many real geological settings, the isothermal/isoviscous assumption are not valid. Indeed, many geological elastic-plated gravity currents are comprised of fluid whose viscosity can vary by several orders of magnitude depending on its temperature. This is the case for magmas produced by partial melting of the upper mantle and intruding the shallow layers of the crust (*Shaw*, 1972; *Lejeune and Richet*, 1995). Therefore, as the fluid is cooling, its composition and crystal content changes which, in turn, modifies the viscosity and the dynamics of the flow. Several studies have shown that this coupling between the cooling and the flow itself in a gravity current results in important deviations from the isoviscous case (*Bercovici*, 1994; *Balmforth* *and Craster*, 2004; *Garel et al.*, 2014).

In this paper, we examine how the spreading of an elastic-plated gravity current is affected by the cooling itself. In particular, we consider the problem of an elastic-plated gravity current whose viscosity depends on temperature according to a prescribed rheology $\eta(T)$. This gives rise to a set of two coupled non-linear equations that we solve numerically. We study the flow thermal structure and its effect on the dynamics through the rheology in each regime separately. In both regimes, we identify different "thermal" phases of propagation that we characterize by different scaling laws. We then discuss our result implications concerning the emplacement of terrestrial laccoliths.

3.2 Theory

3.2.1 Formulation

We model the axisymmetric flow of fluid below an elastic layer of constant thickness d_c and above a semi infinite rigid layer (*Michaut*, 2011) (Figure 3.1). The assumption that the thickness of the fluid $h(r,t)$ tends to zero at the contact line leads to divergent viscous stresses and to the theoretical immobility of the current (*Flitton and King*, 2004). To avoid problem at the contact line, we consider a thin pre-wetting film of thickness h_f (*Lister et al.*, 2013) (Figure 3.1).

The fluid is injected continuously at the base and center of the current at a constant rate Q_0 through a conduit of diameter a. The hot fluid is intruded at temperature T_i and cools through the top and bottom by conduction in the surrounding medium, whose temperature is considered constant and equal to T_0. In using a fixed temperature at the flow boundary, we essentially assume the fluid is bounded by a medium with infinite thermal conductivity.

As it cools, the viscosity of the fluid increases following a prescribed rheology $\eta(T)$ given by

$$\eta(T) = \frac{\eta_h \eta_c (T_i - T_0)}{\eta_h (T_i - T_0) + (\eta_c - \eta_h)(T - T_0)} \tag{3.1}$$

where η_h and η_c are the viscosities of the hottest and coldest fluid at the temperature T_i and T_0 respectively (*Bercovici*, 1994). Although this rheology is largely simplified, the inverse dependence of viscosity on temperature captures the essential behavior of a viscous fluid, i.e. the viscosity variations are the largest where the temperature is the coldest (*Shaw*, 1972; *Marsh*, 1981; *Lejeune and Richet*, 1995; *Giordano et al.*, 2008).

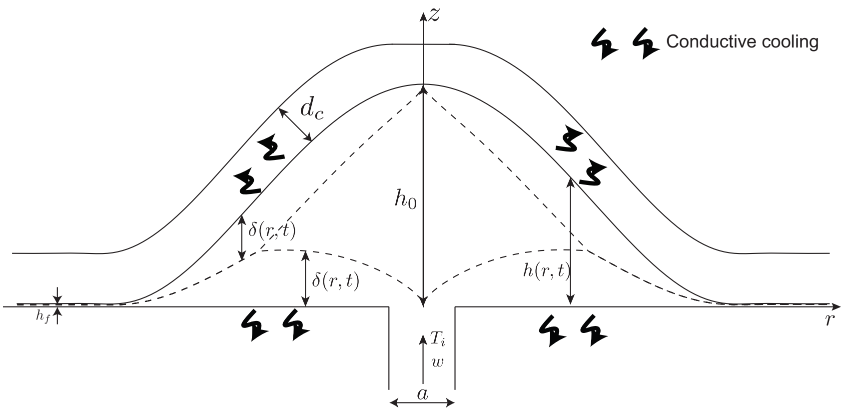

Figure 3.1: Model geometry and parameters. The vertical scale is exaggerated.

3.2.2 Pressure

The intrusion develops over a length scale Λ that is much larger than its thickness H ($\Lambda >> H$). In the laminar regime and in axisymmetrical coordinates (r,z), the Navier-Stokes equations under the lubrication assumption are

$$-\frac{\partial P}{\partial r} + \frac{\partial}{\partial z}\left(\eta(T)\frac{\partial u}{\partial z}\right) = 0 \tag{3.2}$$

$$-\frac{\partial P}{\partial z} - \rho_m g = 0 \tag{3.3}$$

where $u(r,z,t)$ is the radial velocity, ρ_m the fluid density, g the standard acceleration due to gravity and $P(r,z,t)$ the pressure within the fluid. Integration of (3.3) gives the total pressure $P(r,z,t)$ within the flow. When the vertical deflection $h(r,t)$ of the upper elastic layer is small compared to its thickness d_c, i.e $h << d_c$, we can neglect stretching of the upper layer and only consider bending stresses. Therefore, the total pressure $P(r,z,t)$ at a level z in the current is the sum of three contributions: the weight of the magma and of the upper layer and the bending pressure

$$P = \rho_m g(h - z) + \rho_r g d_c + D\nabla_r^4 h \tag{3.4}$$

where $h(r,t)$ is the flow thickness, ρ_r the density of the surrounding rocks and D is the flexural rigidity of the thin elastic layer, that depends on Young's modulus E, Poisson's ratio ν^* and on the elastic layer thickness d_c as $D = Ed_c^3/\left(12(1-\nu^*)\right)$.

3.2.3 Injection rate

Assuming a Poiseuille flow within the cylindrical feeding conduit, the vertical injection velocity $w_i(r,t)$ and injection rate Q_0 are given by

$$w_i(r,t) = \begin{cases} \frac{\Delta P}{4\eta_h Z_c}(\frac{a^2}{4} - r^2) & r \leq \frac{a}{2} \\ 0 & r > \frac{a}{2} \end{cases} \tag{3.5}$$

$$Q_0 = \frac{\pi \Delta P a^4}{128 \eta_h Z_c} \tag{3.6}$$

where ΔP is the initial overpressure within the melt at $z = Z_c$.

3.2.4 Heat transport equation

3.2.4.1 Local energy conservation

In the laminar regime and in axisymmetrical coordinates (r,z), the local energy conservation equation within the lubrication assumption is written as

$$\frac{D}{Dt}\left(\rho_m C_{p,m} T + \rho_m L(1-\phi)\right) = k_m \frac{\partial^2 T}{\partial z^2} \tag{3.7}$$

where $T(r,z,t)$ is the fluid temperature and ρ_m, k_m and $C_{p,m}$ are the density, thermal conductivity and specific heat of the fluid. Here, we also account for energy release by crystallization of the fluid, which is a non negligible source of heat for magmas; $\phi(r,z,t)$ is the crystal fraction in the melt and L the latent heat. In this model, the crystals are considered only as a source/sink of energy as they melt/form during flow emplacement. In particular, the physical properties of the fluid are not modified by the presence of crystals.

Following a common approximation, we assume that the crystal fraction is a linear function of temperature over the melting interval

$$\phi = \frac{T_L - T}{T_L - T_s} \tag{3.8}$$

where T_S and T_L are the solidus and liquidus temperatures of the magma (*Hort*, 1997; *Michaut and Jaupart*, 2006). In addition, we assume that the fluid is injected as its liquidus temperature , i.e. $T_L = T_i$ and, for simplicity, that the solidus temperature is equal to the surrounding rock temperature $T_S = T_0$. With these approximations, the local energy equation (3.7) resumes to

$$\frac{\partial T}{\partial t} + u\frac{\partial T}{\partial r} + w\frac{\partial T}{\partial z} = \frac{St}{St+1}\kappa_m \frac{\partial^2 T}{\partial z^2} \tag{3.9}$$

where $u(r,z,t)$ and $w(r,z,t)$ are the radial and vertical fluid velocities, $St = (C_{p,m}(T_i - T_0))/L$ is the Stephan number and κ_m is the fluid thermal diffusivity $\kappa_m = k_m/(\rho_m C_{p,m})$. We use an integral balance method to solve the heat transport equation (3.9). This theory is based on the integral-balance method of heat-transfer theory of *Goodman* (1958), in which the vertical structure of the temperature field is represented by a known function of depth that approximates the expected solution.

3.2.4.2 Integral balance solution for the temperature $T(r,z,t)$

Following *Balmforth and Craster* (2004), we model the cooling of the flow through the growth of two thermal boundary layers: one growing downward from the top and a second growing upward from the base. As we consider homogeneous thermal properties for the surrounding rocks, we assume that the two thermal boundary layers grow symmetrically and have the same thickness $\delta(r,t)$. We use the following approximation for the vertical temperature profile $T(r,z,t)$

$$T = \begin{cases} T_b - (T_b - T_0)(1 - \frac{z}{\delta})^2 & 0 \leq z \leq \delta \\ T_b & \delta \leq z \leq h - \delta \\ T_b - (T_b - T_0)(1 - \frac{h-z}{\delta})^2 & h - \delta \leq z \leq h \end{cases} \tag{3.10}$$

where $T_b(r,t)$ is the temperature at the center of the flow. The integral balance solution in (3.10) assumes a symmetry around $z = h/2$ and a decrease of the temperature in the two thermal boundary layers down to the surrounding rock temperature T_0 (*Balmforth and Craster*, 2004). In addition, it assumes a uniform temperature T_b in between the thermal boundary layers. As the fluid is injected at temperature T_i, we have $T_b(r,t) = T_i$ as long as $\delta < h/2$. However, if the two thermal boundary layers connect, then $\delta = h/2$ and T_b becomes such that $T_b \leq T_i$. This profile assures the continuity of the temperature and heat flux within the flow.

3.2.4.3 Integral balance equation

We begin by integrating the local energy conservation equation (3.9) separately over the two thermal boundary layers. The integration over the bottom thermal layer, i.e. from the base, $z = 0$ to a level $z = \delta$ gives

$$\begin{aligned} &\frac{\partial}{\partial t}\left(\delta(\bar{T} - T_b)\right) + \frac{1}{r}\frac{\partial}{\partial r}\left(r\delta(\overline{uT} - \bar{u}T_b)\right) + \delta\left(\frac{\partial T_b}{\partial t} + \bar{u}\frac{\partial T_b}{\partial r}\right) \\ = \quad &-\frac{\kappa_m}{1+St}\left.\frac{\partial T}{\partial z}\right|_{z=0} + w_i(T_i - T_b) \end{aligned} \tag{3.11}$$

where the bars indicate the vertical average over the bottom thermal boundary layer

$$\overline{f} = \frac{1}{\delta}\int_0^{\delta} f dz,$$

$T_b(r,t)$ is the temperature at $z=\delta$, $w_i(r)$ is the vertical injection velocity and we have used the nullity of the thermal gradient at $z=\delta$ and the local mass conservation

$$\frac{1}{r}\frac{\partial ru}{\partial r} + \frac{\partial w}{\partial z} = 0. \tag{3.12}$$

The integration over the top thermal layer, i.e., from the level, $z = h-\delta$ to the top $z=h$ gives

$$\begin{aligned} &\frac{\partial}{\partial t}\left(\delta(\bar{T}-T_b)\right) + \frac{1}{r}\frac{\partial}{\partial r}\left(r\delta(\overline{uT}-\bar{u}T_b)\right) + \delta\left(\frac{\partial T_b}{\partial t} + \overline{u}\frac{\partial T_b}{\partial r}\right) \\ = \;& \frac{\kappa_m}{1+St^{-1}}\left.\frac{\partial T}{\partial z}\right|_{z=h}. \end{aligned} \tag{3.13}$$

where, in addition to the local mass conservation (3.12) and the fact that the thermal gradient at $z=h-\delta$ is equal to zero, we have used the kinematic boundary condition in $z=h(r,t)$

$$\frac{\partial h}{\partial t} + u\frac{\partial h}{\partial r} = w \tag{3.14}$$

Therefore, the heat balance equation, i.e. the heat equation (3.9) integrated over the flow thickness, is obtained by adding (3.11) and (3.13). Introducing (3.10) to derive the conductive fluxes, we finally obtain

$$\begin{aligned} &\frac{\partial}{\partial t}\left(\delta(\bar{T}-T_b)\right) + \frac{1}{r}\frac{\partial}{\partial r}\left(r\delta(\overline{uT}-\bar{u}T_b)\right) + \delta\left(\frac{\partial T_b}{\partial t} + \overline{u}\frac{\partial T_b}{\partial r}\right) \\ = \;& -\frac{2\kappa_m}{(1+St^{-1})}\frac{(T_b-T_0)}{\delta} + \frac{w_i}{2}(T_i-T_b) \end{aligned} \tag{3.15}$$

3.2.5 Equation of motion

A global statement of mass conservation gives

$$\frac{\partial h}{\partial t} + \frac{1}{r}\frac{\partial}{\partial r}\left(r\int_0^h u dz\right) = w_i. \tag{3.16}$$

To obtain an equation for the flow thickness, we first note that the chosen vertical structure of the temperature field (3.10) is symmetric around $h/2$, and thus, the viscosity and velocity u possess the same symmetry. Taking advantage of this symmetry, we integrate once (3.2) using $\frac{\partial u}{\partial z}\big|_{z=h/2} = 0$ to get

$$\frac{\partial u}{\partial z} = \frac{1}{\eta}\frac{\partial P}{\partial r}\left(z - \frac{h}{2}\right). \tag{3.17}$$

Using no-slip boundary conditions at the top and the bottom of the flow, i.e. $u(r, z = 0, t) = u(r, z = h, t) = 0$ equation (3.16) can be rewritten as

$$\frac{\partial h}{\partial t} = \frac{1}{r}\frac{\partial}{\partial r}\left(r\int_0^h \frac{\partial u}{\partial z} z dz\right) + w_i \tag{3.18}$$

and injecting (3.17) into (3.18) finally gives the equation for the flow thickness evolution in axisymmetric coordinates

$$\frac{\partial h}{\partial t} = \frac{1}{r}\frac{\partial}{\partial r}\left(r\left(\rho_m g\frac{\partial h}{\partial r} + D\frac{\partial}{\partial r}\left(\nabla_r^4 h\right)\right)\left(\int_0^h \frac{1}{\eta(y)}\left(y - \frac{h}{2}\right) y dy\right)\right) + w_i \tag{3.19}$$

In addition, integration of (3.17) using the no-slip boundary condition at the base of the flow gives

$$u(r, z, t) = \frac{\partial P}{\partial r}\int_0^z \frac{1}{\eta(y)}\left(y - \frac{h}{2}\right) dy. \tag{3.20}$$

3.2.6 Dimensionless equations

We use the characteristic temperature interval $\Delta T = T_i - T_0$ to nondimensionalize temperatures. The dimensionless integral balance approximation (3.10) becomes

$$\theta(z) = \begin{cases} \Theta_b\left(1 - (1 - \frac{z}{\delta})^2\right) & 0 \leq z \leq \delta \\ \Theta_b & \delta \leq z \leq h - \delta \\ \Theta_b\left(1 - (1 - \frac{h-z}{\delta})^2\right) & h - \delta \leq z \leq h \end{cases} \tag{3.21}$$

where $\theta(r, z, t)$ is the dimensionless temperature and $\Theta_b = \frac{T_b - T_0}{T_i - T_0}$. Finally, equations (3.15) and (3.19) are nondimensionalized using a horizontal scale Λ, a vertical scale H and a time scale τ given by

$$\Lambda = \left(\frac{D}{\rho_m g}\right)^{1/4} \tag{3.22}$$

$$H = \left(\frac{12\eta_h Q_0}{\rho_m g \pi}\right)^{1/4} \tag{3.23}$$

$$\tau = \frac{\pi \Lambda^2 H}{Q_0} \tag{3.24}$$

where Λ represents the flexural wavelength of the upper elastic layer (*Michaut*, 2011), H the characteristic thickness of an isoviscous constant flux gravity current with viscosity η_h (*Huppert*, 1982b) and τ the characteristic time to fill up a cylindrical flow of radius Λ and thickness H at a constant rate Q_0. In addition, we can define a horizontal velocity scale $U = \Lambda/\tau = (\rho_m g H^3) / (12\eta_h \Lambda)$.

The dimensionless equations are

$$\frac{\partial h}{\partial t} = \frac{12}{r}\frac{\partial}{\partial r}\left(r\left(\frac{\partial h}{\partial r}+\frac{\partial}{\partial r}\left(\nabla_r^4 h\right)\right)I_1(h)\right)+w_i \quad (3.25)$$

$$\frac{\partial}{\partial t}\left(\delta(\bar{\theta}-\Theta_b)\right) = -\frac{1}{r}\frac{\partial}{\partial r}\left(r\delta(\overline{u\theta}-\bar{u}\Theta_b)\right)-\delta\left(\frac{\partial \Theta_b}{\partial t}+\bar{u}\frac{\partial \Theta_b}{\partial r}\right) - 2Pe^{-1}St_m\frac{\Theta_b}{\delta}+\frac{w_i}{2}(1-\Theta_b) \quad (3.26)$$

$$w_i = \frac{32}{\gamma^2}\left(\frac{1}{4}-\frac{r^2}{\gamma^2}\right) \text{ if } r<\gamma/2, \quad w_i = 0 \text{ if } r\geq\gamma/2 \quad (3.27)$$

$$u(r,z,t) = 12\left(\frac{\partial h}{\partial r}+\frac{\partial}{\partial r}\left(\nabla_r^4 h\right)\right)I_0(z) \quad (3.28)$$

with

$$I_0(z) = \int_0^z (\nu+(1-\nu)\theta(y))\left(y-\frac{h}{2}\right)dy \quad (3.29)$$

$$I_1(z) = \int_0^z (\nu+(1-\nu)\theta(y))\left(y-\frac{h}{2}\right)ydy \quad (3.30)$$

and where γ, Pe, St_m and ν are the four dimensionless numbers that control the dynamics of the flow

$$\gamma = \frac{a}{\Lambda} \quad (3.31)$$

$$Pe = \frac{H^2}{\kappa_m \tau} \quad (3.32)$$

$$St_m = \frac{C_{p,m}(T_i-T_0)}{C_{p,m}(T_i-T_0)+L} \quad (3.33)$$

$$\nu = \frac{\eta_h}{\eta_c}. \quad (3.34)$$

γ is the dimensionless radius of the conduit, it does not significantly influence the flow and is set to 0.02 in this study (*Michaut and Bercovici*, 2009; *Michaut*, 2011); Pe is the Peclet number which compares the vertical diffusion of heat to the horizontal advection in the interior; St_m is a modified Stephan number which represents the ratio of sensible heat between solidus and liquidus to the total energy of the fluid at liquidus temperature and ν is the maximum viscosity contrast, i.e. the ratio between the hottest and coldest viscosity.

3.2.7 Further simplifications

3.2.7.1 Heat equation

The heat balance equations (3.26) can reduce to

$$\frac{\partial}{\partial t}\left(\delta(\bar{\theta}-1)\right)+\frac{1}{r}\frac{\partial}{\partial r}\left(r\delta(\overline{u\theta}-\bar{u})\right) \quad = \quad -2Pe^{-1}St_m\frac{\Theta_b}{\delta} \tag{3.35}$$

Indeed, if the thermal boundary layers exist, $\Theta_b = 1$, δ is the variable and (3.26) directly reduces to (3.35). In contrast, if the thermal boundary layers merge, $\delta = h/2$ and the variable is Θ_b. In this case, the heat balance equation (3.26) reduces to

$$\frac{\partial h\bar{\theta}}{\partial t}+\frac{1}{r}\frac{\partial}{\partial r}\left(rh\overline{u\theta}\right)-\Theta_b\left(\frac{\partial h}{\partial t}+\frac{1}{r}\frac{\partial}{\partial r}\left(rh\bar{u}\right)\right) \quad = \quad -8St_mPe^{-1}\frac{\Theta_b}{h}+w_i(1-\Theta_b) \tag{3.36}$$

which, by using (3.16), rewrites

$$\frac{\partial h\bar{\theta}}{\partial t}+\frac{1}{r}\frac{\partial}{\partial r}\left(rh\overline{u\theta}\right)=w_i-8St_mPe^{-1}\frac{\Theta_b}{h}. \tag{3.37}$$

Equation (3.37) also corresponds to (3.35) when $\delta = h/2$.

Following *Balmforth and Craster* (2004), we rewrite (3.35) using a new variable $\xi = \delta(1-\bar{\theta})$

$$\frac{\partial \xi}{\partial t}+\frac{1}{r}\frac{\partial}{\partial r}\left(r\bar{u}\xi\right)-\frac{1}{r}\frac{\partial}{\partial r}\left(r\delta(\overline{u\theta}-\bar{u}\bar{\theta})\right)=2Pe^{-1}St_m\frac{\Theta_b}{\delta}. \tag{3.38}$$

where Θ_b and δ can be calculated directly from the expression of ξ such that

$$\Theta_b(r)=\begin{cases}1 & \text{if} \quad \xi\leq\xi_t\\ \frac{3}{2}-\frac{3\xi}{h} & \text{if} \quad \xi>\xi_t\end{cases} \qquad \delta(r)=\begin{cases}3\xi & \text{if} \quad \xi\leq\xi_t\\ h(r,t)/2 & \text{if} \quad \xi>\xi_t\end{cases}$$

with $\xi_t = h/6$.

The second term on the left hand side of (3.38) contains advection by the vertically integrated radial velocity while the third term contains a correction accounting for the vertical structure of the temperature field. The term on the right is the loss of heat by conduction in the surrounding medium.

3.2.7.2 Average quantities

The average velocity over a thermal boundary layer $\overline{u}$ reads

$$\overline{u}=\frac{1}{\delta}\int_0^\delta u dz \quad = \quad u(r,\delta,t)-\frac{1}{\delta}\int_0^\delta\frac{\partial u}{\partial z}zdz \tag{3.39}$$

$$\quad = \quad \frac{12}{\delta}\frac{\partial P}{\partial r}\left(\delta I_0(\delta)-I_1(\delta)\right) \tag{3.40}$$

where $P(r,z,t) = h + \nabla_r^4 h$ is the dimensionless pressure and we have used (3.17) in (3.39). The average rate of heat advected $\overline{u\theta}$ over a thermal boundary layer reads

$$\begin{aligned}\overline{u\theta} = \frac{1}{\delta}\int_0^\delta u\theta dz &= \frac{1}{\delta}\left([uG(z)]_0^\delta - \int_0^\delta G(z)\frac{\partial u}{\partial z}dz\right) \\ &= \frac{12}{\delta}\frac{\partial P}{\partial r}\left(G(\delta)I_0(\delta) - I_2(\delta)\right) \end{aligned} \tag{3.41}$$

where

$$G(z) = \Theta_b\left(z + \frac{\delta}{3}\left(1 - \frac{z}{\delta}\right)^3\right) \tag{3.42}$$

denotes a primitive of θ when $z < \delta$ and

$$I_2(z) = \int_0^y \left(\nu + (1-\nu)\theta(y)\right) G(y)\left(y - \frac{h}{2}\right) dy. \tag{3.43}$$

Therefore, we have

$$\overline{u\theta} - \overline{u}\overline{\theta} = \frac{12}{\delta}\frac{\partial P}{\partial r}\left(I_0(\delta)\left(G(\delta) - \delta\overline{\theta}\right) + \overline{\theta}I_1(\delta) - I_2(\delta)\right) \tag{3.44}$$

where the average temperature over a thermal boundary layer is $\overline{\theta} = 2\Theta_b/3$

3.2.8 Summary of the equations

The coupled equations governing the cooling of an elastic-plated gravity current are summarized in term of the integrals (3.29), (3.30) and (3.43) as follow

$$\frac{\partial h}{\partial t} - \frac{12}{r}\frac{\partial}{\partial r}\left(rI_1(h)\frac{\partial P}{\partial r}\right) = \mathcal{H}\left(\frac{\gamma}{2} - r\right)\frac{32}{\gamma^2}\left(\frac{1}{4} - \frac{r^2}{\gamma^2}\right) \tag{3.45}$$

$$\frac{\partial \xi}{\partial t} + \frac{1}{r}\frac{\partial}{\partial r}\left(r\left(\bar{u}\xi - \Sigma\right)\right) = 2Pe^{-1}St_m\frac{\Theta_b}{\delta} \tag{3.46}$$

with

$$\Theta_b(r) = \begin{cases} 1 & \text{if} \quad \xi \le \xi_t \\ \frac{3}{2} - \frac{3\xi}{h} & \text{if} \quad \xi > \xi_t \end{cases} \qquad \delta(r) = \begin{cases} 3\xi & \text{if} \quad \xi \le \xi_t \\ h(r,t)/2 & \text{if} \quad \xi > \xi_t \end{cases}$$

$$\overline{u} = \frac{12}{\delta}\frac{\partial P}{\partial r}\left(\delta I_0(\delta) - I_1(\delta)\right) \tag{3.47}$$

$$\Sigma = \frac{\partial P}{\partial r}\left(8I_1(\delta)\Theta_b - 12I_2(\delta)\right) \tag{3.48}$$

$P = h + \nabla_r^4 h$ is the dimensionless pressure and $\mathcal{H}$ the Heaviside function. The expression of $I_0(\delta)$, $I_1(h)$, $I_1(\delta)$ and $I_2(\delta)$ as well as the numerical scheme are given in appendix 3.8.

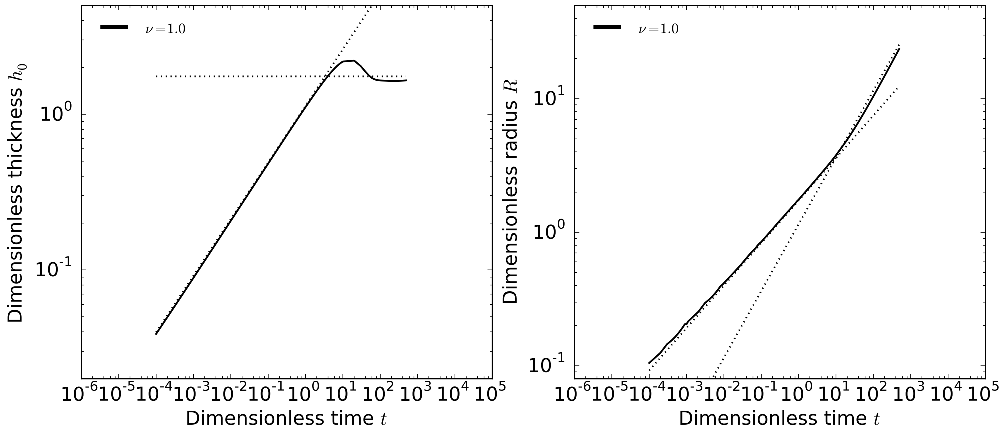

Figure 3.2: Left: Dimensionless thickness at the center h_0 versus dimensionless time t. Dotted-lines: scaling laws in the bending regime $h_0 = 0.7 h_f^{-1/11} t^{8/22}$ and the gravity regime h_0 tends to a constant. Right: Dimensionless radius R versus dimensionless time t. Dotted-lines: scaling laws in the bending regime $R = 2.2 h_f^{1/22} t^{7/22}$ and in the gravity current regime $R \propto t^{1/2}$.

3.2.9 Preliminary results for an isothermal flow

For a constant injection rate, a small pre-wetting film thickness, i.e. $h_f << 1$ and a viscosity contrast ν set to 1, numerical resolution of (3.45) shows two asymptotic spreading regimes (*Michaut*, 2011; *Lister et al.*, 2013).

At early times, when $R << \Lambda$, gravity is negligible and the spreading dynamics is governed by the bending of the upper layer. The spreading is very slow and the interior has uniform pressure $P = \nabla_r^4 h$. The flow is bell-shaped and its thickness is given by

$$h(r,t) = h_0(t) \left(1 - \frac{r^2}{R^2(t)}\right)^2 \tag{3.49}$$

with $h_0(t)$ the thickness of the current at the center (*Michaut*, 2011; *Lister et al.*, 2013). In this regime, *Lister et al.* (2013) have shown that the spreading is controlled by the propagation of a peeling by bending wave at the flow front with dimensionless velocity c

$$c = \frac{\partial R}{\partial t} = h_f^{1/2} \left(\frac{\kappa}{1.35}\right)^{5/2} \tag{3.50}$$

where $\kappa = \partial^2 h / \partial r^2$ is the dimensionless curvature of the interior solution. Using the propagation law (3.50) and the form of the interior solution (3.49), they find that the flow radius and height are given by the following solutions

$$h_0(t) = 0.7h_f^{-1/11}t^{8/22} \quad (3.51)$$
$$R(t) = 2.2h_f^{1/22}t^{7/22}. \quad (3.52)$$

where the numerical pre-factor obtained in our simulations match those of *Lister et al.* (2013) (Figure 3.2).

In contrast, when the radius R becomes larger than 4Λ ($R >> \Lambda$), the weight of the current becomes dominant over the bending terms. The pressure is given by the hydrostatic pressure $P = h$ and the current enters a classical gravity current regime where bending terms only affect the solution near the edge of the current (*Huppert*, 1982a; *Michaut*, 2011; *Lister et al.*, 2013). In this second regime, the radius evolves as $t^{1/2}$ and the thickness tends to a constant (Figure 3.2).

In the following, we study the effect of the cooling on the flow dynamics in both regimes separately. We first describe the thermal structure for an isoviscous flow, i.e. $\nu = 1$ and then study the effect of the temperature-dependent viscosity on the flow dynamics without crystallization, i.e $St_m = 1$. Finally, we look at the effect of crystallization by setting $St_m < 1$. For simplicity, we present the results for a given film thickness ($h_f = 5 \cdot 10^{-3}$). Results for different film thicknesses are shown in Appendix 3.8.

3.3 Numerical approach

3.3.1 General procedure

The coupled nonlinear partial differential equations (3.45) and (3.46) are solved on a grid of size M defined by the relation $r_i = (i - 0.5)\Delta r$ for $i = 1, .., M$. The grid is shifted at the center to avoid problem arising from the axisymmetrical geometry. We index the grid point by the indice i and denote the solution on this grid h_i and ξ_i and the secondary variables $\Theta_{b,i}$, $\Theta_{s,i}$ and δ_i. Both equations can be expressed on the convenient form

$$\frac{\partial u}{\partial t} - f = 0 \quad (3.53)$$

where u is the function we want to integrate and f a non-linear function that depends on u. We solve these equations by first discretizing all the spatial derivatives using Finite Difference. The accuracy of the scheme is determined by the higher order derivatives since their numerical approximation requires the largest number of sample points. We then get two systems of M ordinary differential equations with the form

$$\frac{\partial u_i}{\partial t} - f_i = 0 \qquad i = 1, ..., M \tag{3.54}$$

The time derivatives are first order and, since explicit schemes tend to be very sensitive and unstable, we use a fully implicit backward Euler scheme to get

$$\frac{u_i^{n+1} - u_i^n}{\Delta t} - f_i(u_i^{n+1}) = 0 \qquad i = 1, ..., M \tag{3.55}$$

Since $f_i(u_i^{n+1})$ is not a linear function, the system above cannot be re-arranged to solve u_i^{n+1} in term of u_i^n and an iterative method has to be employed instead. Fixed point iteration method have shown poor results in converging toward the solution and we finally apply second order Newton's method to obtain the solution at each time step. In particular, we first linearize u^{n+1} around a guess of the solution by assuming $u^{n+1} = u^* + \delta u^n$, where u^* is a guess and δu^n is the error and we drop the i for clarity. Then, we expressed the non-linear part using a Taylor's expansion

$$f^{n+1} = f(u^{n+1}) = f(u^* + \delta u^n) = f(u^*) + J_f^h(u^*)\delta u^n$$

where $J_f^u(u^*)$ is the jacobian matrix for the function f evaluated in h^*. Injecting the expansion into (3.55) finally gives a system of M linear equations for the correction term δ_h^n which can be expressed as

$$(I - \Delta t J_f^u(u^*))\delta u^n = u^n - u^* + \Delta t f(u^*) \tag{3.56}$$

where I is the identity matrix. Therefore, each iteration solves for δu^n and we use $u_n + \delta u^n$ as a new guess u^* in each iteration. This is repeated until δu^n becomes sufficiently small. Finally, since the equations are coupled, we use a fixed-point iteration method to converge toward the solution (h, ξ) at each time step. Therefore, the algorithm is the following at each time step

- Start with a guess for the values of all variables.
- Solve the thickness equation (3.45) for h^{n+1} using Newton-Rhapsod method.
- Solve the heat equation (3.46) for ξ^{n+1} using h^{n+1} as a new guess for h^* and Newton-Rhapsod method.
- Repeat step one until further iterations cease to produce any significant changes in the values of both h^{n+1} and ξ^{n+1}.

The computational scheme is summarized in the following.

3.3.2 Thickness equation

The thickness equation (3.45) is written as

$$\frac{\partial h}{\partial t} - f(h,\xi) \quad = \quad 0 \tag{3.57}$$

with

$$\begin{aligned} f &= \frac{1}{r}\frac{\partial}{\partial r}\left(r\phi\left(\frac{\partial}{\partial r}(h+P)\right)\right) + w_i & (3.58)\\ \phi &= 12 I_1(h) & (3.59)\end{aligned}$$

and where P is the dimensionless bending pressure $P = \nabla^4 h$.

Spatial discretization of f

The spatial discretization is obtained using a central difference scheme over a sub-grid shifted by $0.5\Delta r$ from the main grid. Therefore, we have

$$\begin{aligned} f_i &= \frac{1}{r_i\Delta_r}\left(r_{i+1/2}\phi_{i+1/2}\left(\frac{\partial h}{\partial r}+\frac{\partial P}{\partial r}\right)\bigg|_{i+1/2} - r_{i-1/2}\phi_{i-1/2}\left(\frac{\partial h}{\partial r}+\frac{\partial P}{\partial r}\right)\bigg|_{i-1/2}\right)\\ &= A_i\phi_{i+1/2}\left(h_{i+1}-h_i\right) - B_i\phi_{i-1/2}\left(h_i-h_{i-1}\right)\\ &+ A_i\phi_{i+1/2}\left(P_{i+1}-P_i\right) - B_i\phi_{i-1/2}\left(P_i-P_{i-1}\right)\\ &+ w_i \end{aligned} \tag{3.60}$$

where $A_i = r_{i+1/2}/(r_i\Delta_r^2)$ and $B_i = r_{i-1/2}/(r_i\Delta_r^2)$. The bending pressure term P is very stiff and needs a careful treatment. In particular, the fourth order derivative requires a fourth order central difference scheme and therefore, P_i is expressed over a seven point stencil on the main grid such that

$$P_i = \alpha_i h_{i-3} + \beta_i h_{i-2} + \gamma_i h_{i-1} + \lambda_i h_i + \kappa_i h_{i+1} + \delta_i h_{i+2} + \varepsilon_i h_{i+3} \tag{3.61}$$

with

$$\begin{aligned} \alpha_i &= \frac{1}{24\Delta r^4}\left(-4 + 3p_3\Delta_r\right)\\ \beta_i &= \frac{1}{24\Delta r^4}\left(48 - 24p_3\Delta_r - 2p_2\Delta_r^2 + 2p_1\Delta_r^3\right)\\ \gamma_i &= \frac{1}{24\Delta r^4}\left(-156 + 39p_3\Delta_r + 32p_2\Delta_r^2 - 16p_1\Delta_r^3\right)\\ \lambda_i &= \frac{1}{24\Delta r^4}\left(224 - 60p_2\Delta r^2\right)\\ \kappa_i &= \frac{1}{24\Delta r^4}\left(-156 - 39p_3\Delta_r + 32p_2\Delta_r^2 + 16p_1\Delta_r^3\right)\\ \delta_i &= \frac{1}{24\Delta r^4}\left(48 + 24p_3\Delta_r - 2p_2\Delta_r^2 - 2p_1\Delta_r^3\right)\\ \varepsilon_i &= \frac{1}{24\Delta r^4}\left(-4 - 3p_3\Delta_r\right)\end{aligned}$$

and where $p_1 = 1/r_i^3$, $p_2 = 1/r_i^2$ and $p_3 = 2/r_i$. Finally, the term $\phi_{i-1/2}$ and $\phi_{i-1/2}$, which depend on the variable Θ_b, δ as well as different power of h, are evaluated in $i-1/2$ and $i+1/2$ respectively. Different choices for the value of the variable at the mid-cell grid point do not show any significant difference and a simple average is taken such that the variable $u_{i+1/2}$ is taken as $0.5(u_i + u_{i+1})$.

Expression of the jacobian J_f^h

The discretized function f_i can be break down in three part, the gravitational part f_i^g which is expressed in term of the value of h on three grid points $\{i-1, i, i+1\}$, the bending part f_i^b which is expressed in term of the value of h on nine grid points $\{i-4, i-3, ..., i+3, i+4\}$ and the injection term which depends only on the grid point i such that

$$f_i = f_i^g + f_i^b + w_i \tag{3.62}$$

Therefore, the jacobian is nona-diagonal and its coefficient J_{il} are

$$J_{il} = \begin{cases} \frac{\partial f_i^b}{\partial h_l} & l = \{i-4, i-3, i-2, i+2, i+3, i+4\} \\ \frac{\partial f_i^g}{\partial h_l} + \frac{\partial f_i^b}{\partial h_l} & l = \{i-1, i, i+1\} \\ 0 & \text{otherwise} \end{cases} \tag{3.63}$$

The different terms can be easily derived from (3.60) and (3.61) with just slight adjustment coming from the boundary conditions.

Boundary condition

We begin with $h_i = h_f$ for $i = 1, .., M$. Since the flow is symmetric in $r = 0$, we require that

$$\left.\frac{\partial h}{\partial r}\right|_{r=0} = \left.\frac{\partial P}{\partial r}\right|_{r=0} = 0 \tag{3.64}$$

and therefore for $i = 1$, we have

$$\begin{aligned} f_i &= A_1 \phi_{i+1/2} (h_{i+1} - h_i) \\ &+ A_i \phi_{i+1/2} (P_{i+1} - P_i) \\ &+ w_i \end{aligned} \tag{3.65}$$

The expression of the bending pressure, evaluated over a 7 point stencils, is problematic close to the boundary and reflection formulae will be used in order to accommodate the boundary conditions *Patankar* (1980). In particular, we have $h_0 = h_1$, $h_{-1} = h_2$ and $h_{-2} = h_3$. Similarly, boundary condition at the end of the mesh is accounted by using a grid much larger than the flow itself and requiring

$$\left.\frac{\partial h}{\partial r}\right|_{r=r_M} = \left.\frac{\partial P}{\partial r}\right|_{r=r_M} = 0 \tag{3.66}$$

which gives for $i = M$

$$\begin{aligned} f_i &= B_i\phi_{i-1/2}\left(h_i - h_{i-1}\right) \\ &+ B_i\phi_{i-1/2}\left(P_i - P_{i-1}\right) \\ &+ w_i \end{aligned} \tag{3.67}$$

with $h_{i>=M} = h_f$.

Newton-Rhapsod method

The Newton-Rhapsod method reads

$$(I - \Delta t J_f^h(h_k^*))\delta h_k^n = h^n - h_k^* + \Delta t f(h_k^*) \tag{3.68}$$

where the k refers to the k iterations, I is a $M \times M$ diagonal matrix and $J_f^h(h^*)$ is a $M \times M$ nona-diagonal matrix. This system of linear equations can be solved using a nona-diagonal algorithm. At the first iteration, we use $h_1^* = h^n$ as a first guess and then we iterate using $h_k^* = h^n + \delta h_{k-1}^n$ as a new guess for each iterations until δh_k^n becomes sufficiently small. In particular, we require that

$$\delta h_k^n / h_k^* < \varepsilon \tag{3.69}$$

with $\varepsilon = 10^{-4}$.

3.3.3 Heat equation

The heat equation (3.46) is written as

$$\frac{\partial \xi}{\partial t} - g(h,\xi) \;=\; 0 \tag{3.70}$$

with

$$g = \frac{1}{r}\frac{\partial}{\partial r}\left(r\Gamma\xi\right) + \frac{1}{r}\frac{\partial}{\partial r}\left(r\Sigma\right) + 2Pe^{-1}St_m\frac{(\Theta_b - \Theta_s)}{\delta} \tag{3.71}$$

$$\Gamma = -\overline{u} \tag{3.72}$$

Spatial discretization of g

As for the thickness equation, the spatial discretization is obtained using a central difference scheme over a sub-grid shifted by $0.5\Delta r$ from the main grid. Therefore, we have

$$\begin{aligned} g_i &= \left(C_i\Gamma_{i+1/2}\xi_{i+1/2} - D_i\Gamma_{i-1/2}\xi_{i-1/2}\right) && (3.73)\\ &+ \left(C_i\Sigma_{i+1/2} - D_i\Sigma_{i-1/2}\right) && (3.74)\\ &+ 2Pe^{-1}St_m\frac{\Theta_{b,i} - \Theta_{s,i}}{\delta_i} && (3.75) \end{aligned}$$

with $C_i = r_{i+1/2}/(r_i\Delta r)$ and $D_i = r_{i-1/2}/(r_i\Delta r)$. We use the average between the grid point i and $i-1$ (resp. $i+1$) to evaluate the quantity in Γ and Σ at $i-1/2$ (resp. $i+1/2$). In addition, we use a classical upwind scheme to handle ξ at the mid grid point which requires

$$\begin{aligned} \xi_{i+1/2} &= \xi_i && (3.76)\\ \xi_{i-1/2} &= \xi_{i-1} && (3.77) \end{aligned}$$

Expression of the Jacobian J_g^ξ

The expression of the Jacobian is much straightforward in that case and its coefficient J_{il} are

$$J_{il} = \begin{cases} -D_i\Gamma_{i-1/2} & l = i-1 \\ C_i\Gamma_{i+1/2} & l = i \\ 0 & \text{otherwise} \end{cases} \qquad (3.78)$$

with only slight adjustment coming from the boundary conditions.

Boundary conditions

We consider $\Theta_b = 1$ and $\delta = 10^{-4}$ in the film at $t = 0$. In this way, we ensure that the average temperature across the film at $t = 0$ is close to 1. By construction, $D_1 = 0$ and therefore, for $i = 1$ we have

$$g_i = C_i\Gamma_{i+1/2}\xi_i + C_i\Sigma_{i+1/2} + 2Pe^{-1}St_m\frac{\Theta_{b,i} - \Theta_{s,i}}{\delta_i} \qquad (3.79)$$

For $i = M$, we consider that $\Gamma_{i+1/2} = \Gamma_i$ and $\Sigma_{i=1/2} = \Sigma_i$. However, the choice for the boundary condition at the border of the grid $i = M$ is not important as we solve the problem over a grid much larger than the flow itself.

Newton-Rhapsod method

The Newton-Rhapsod method reads

$$(I - \Delta t J_g^{\xi}(\xi_k^*))\delta\xi_k^n = \xi^n - \xi_k^* + \Delta t f(\xi_k^*) \tag{3.80}$$

where the k refers to the k iterations, I is a $M \times M$ diagonal matrix and $J_f^h(\xi^*)$ is a $M \times M$ tri-diagonal matrix. This system of linear equations can be solved using a tri-diagonal algorithm. As for the thickness equation, at the first iteration, we use $\xi_1^* = \xi^n$ as a first guess and then we iterate using $\xi_k^* = \xi^n + \delta\xi_{k-1}^n$ as a new guess for each iterations until $\delta\xi_k^n$ becomes sufficiently small. In particular, we require that

$$\delta\xi_k^n / \xi_k^* < \varepsilon \tag{3.81}$$

with $\varepsilon = 10^{-4}$. In addition, at each iteration the quantity $\Theta_{s,k}^*$, $\Theta_{b,k}^*$ and δ_k^*, that are needed to evaluate Γ and Σ, are derived from the value of ξ_k^* using (??), (??) and (??) respectively.

3.4 Evolution in the bending regime

We first concentrate on the case in which only bending contributes to the dynamics pressure. The governing equations are thus (3.45) and (3.46) where $P = \nabla_r^4 h$.

3.4.1 Thermal structure for an isoviscous flow, effect of Pe

The current cools by conduction and thermal boundary layers form at the contact with the surrounding medium. These boundary layers first connect at the tip of the flow, where the small thickness induces an important cooling (Figure 3.3). A region of cold fluid forms at the front.

As the current thickens with time, a balance between advection and diffusion of heat is never reached in the interior of the current. The hot thermal anomaly grows in extent with time but it extends slower than the current itself and the cold fluid region at the tip grows even faster. For instance, for $Pe = 100$, while the region of cold fluid extends over about 10% of the current at $t = 0.5$, it extends over about 20% at $t = 10$ (Figure 3.3). The smaller Pe, the more important the conductive cooling and the larger the cold fluid region is (Figure 3.4 and 3.5). For instance, at $t = 10$, while the cold fluid region extends over about 20% of the current for $Pe = 100$, it extends over more than 70% for $Pe = 1$ (Figure 3.5).

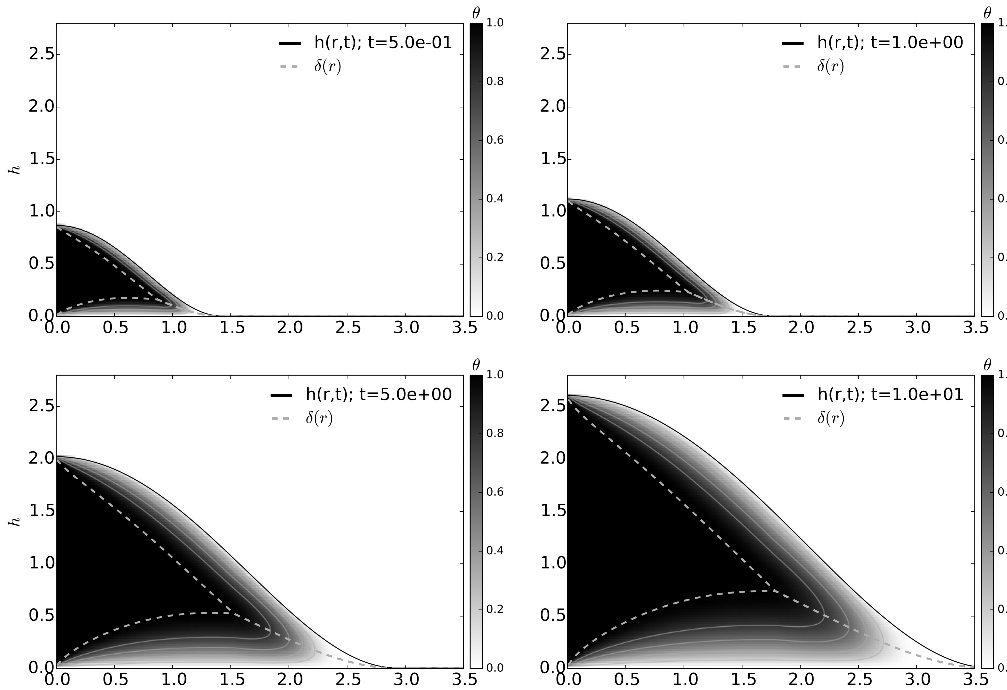

Figure 3.3: Snapshots of the flow thermal structure $\theta(r, z, t)$ at different times indicated on the plot. Dashed lines represent the thermal boundary layers. Solid grey lines are isotherms for $\theta = 0.2$, 0.4, 0.6 and 0.8. Here, $\nu = 1$, $Pe = 100$, $St_m = 1$.

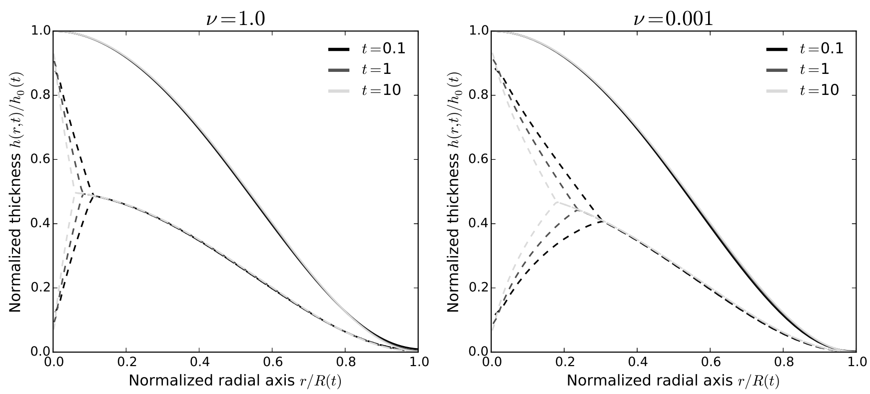

Figure 3.4: Left: thickness normalized by the thickness at the center $h(r, t)/h_0(t)$ versus radial axis normalized by the current radius $r/R(t)$ at different times indicated on the plot for $Pe = 1$ and $\nu = 1.0$. Solid-lines represent the thickness profiles. Dashed-lines represent the thermal boundary layers. Right: Same plot but for $\nu = 10^{-3}$.

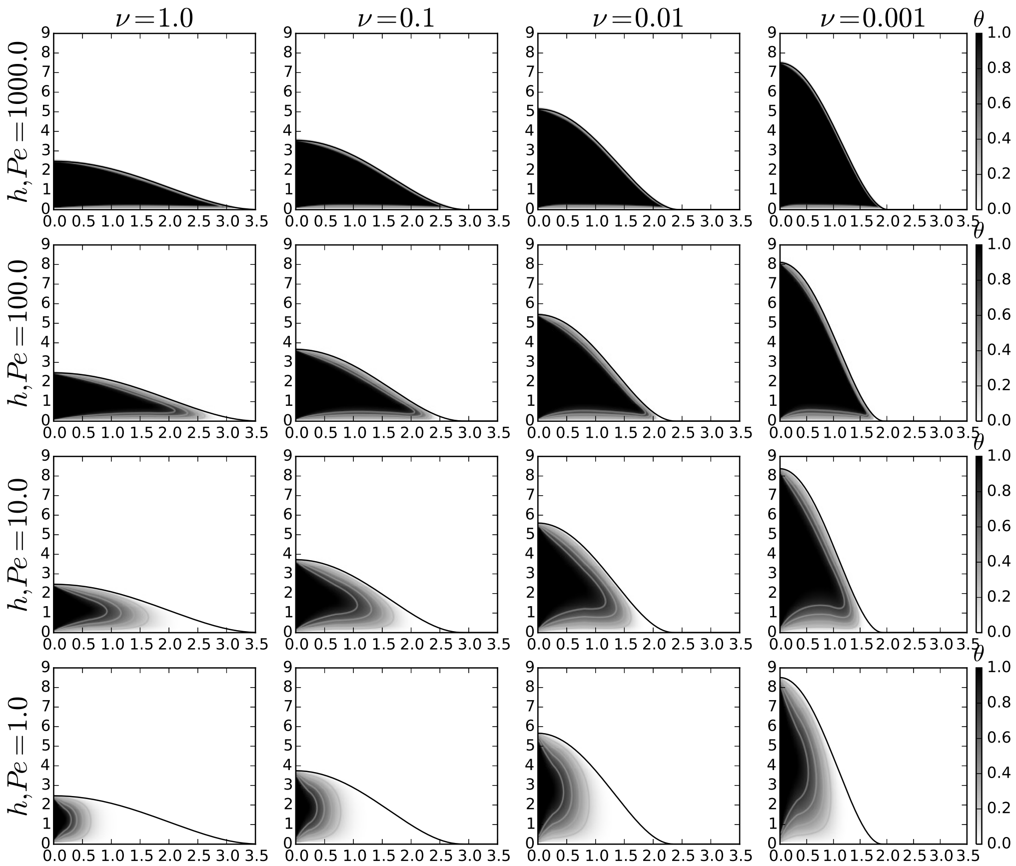

Figure 3.5: Snapshots of the flow thermal structure $\theta(r, z, t)$ for different set (ν,Pe) with ν = 1, 0.1, 0.01 and 0.001 and Pe = 1, 10, 100 and 1000 at t = 10. While Pe controls the thermal structure of the flow, it has only a small influence on the flow aspect ratio which is controlled by ν.

3.4.2 Thickness and temperature profile, effect of ν

When accounting for the temperature dependence of the viscosity, the region of cold fluid at the tip is marked by a higher viscosity and enhances flow thickening at the expense of spreading. The larger the viscosity contrast, the larger the aspect ratio h_0/R (Figure 3.5). For instance, for the same value of $Pe = 1$, while the aspect ratio is 0.7 for $\nu = 1$ at $t = 10$, it is 4.2 for the same time and $\nu = 10^{-3}$ (Figure 3.5). Nevertheless, the shape of the flow remains essentially self-similar (3.49) and cannot be differentiated from the shape of an isoviscous current if the thickness and the radial coordinates are rescaled by the thickness at the center $h_0(t)$ and radius $R(t)$ (Figure 3.4).

The flow thermal structure is similar to the isoviscous case (Figure 3.5), the thermal anomaly rapidly detaches from the tip of the current and a region of cold fluid develops at the front where the heat loss is largest. However, the important thickening induced by the viscosity increase limits heat loss to the surrounding. The larger the viscosity contrast ν, the more important the thickening and the larger the thermal anomaly at a given time. For instance, for $Pe = 1$, while the thermal anomaly extends over about 30% of the flow for $\nu = 1$ at $t = 10$, it extends over more than 50% for $\nu = 10^{-3}$ (Figure 3.5).

As expected, a larger Peclet number leads to a larger thermal anomaly (Figure 3.5). However, although different Peclet numbers cause very different thermal structures, the influence of the Peclet number on the flow morphology is small, much smaller than the effect of the viscosity contrast ν (Figure 3.5). For instance, for $\nu = 10^{-3}$ at $t = 10$, the thermal anomaly is still attached to the tip of the current for $Pe = 1000$ whereas it makes about 50% of the current for $Pe = 1$; but, the thickness h_0 and the radius R in both cases differ only by a few percents (Figure 3.5). This suggests that the spreading of the flow is not controlled by the mean temperature or average viscosity of the flow.

3.4.3 Evolution of the thickness and the radius

The dynamics show three different spreading phases. The thickness as well as the radius first follow the isoviscous scaling laws for a hot viscosity current $h_0 \propto t^{8/22}$ (3.51) and $R \propto t^{7/22}$ (3.52) (Figure 3.6). In the second phase, thickening occurs at the expense of spreading because the thermal anomaly has detached from the current radius and the viscous cold fluid region at the front slows down the spreading. Finally, the dynamics enters a third phase where the thickness and radius follow the scaling laws for the spreading of an isoviscous current characterized by a dimensionless cold viscosity $1/\nu$. These scaling laws are obtained from (3.51) and (3.52) by rescaling the characteristic

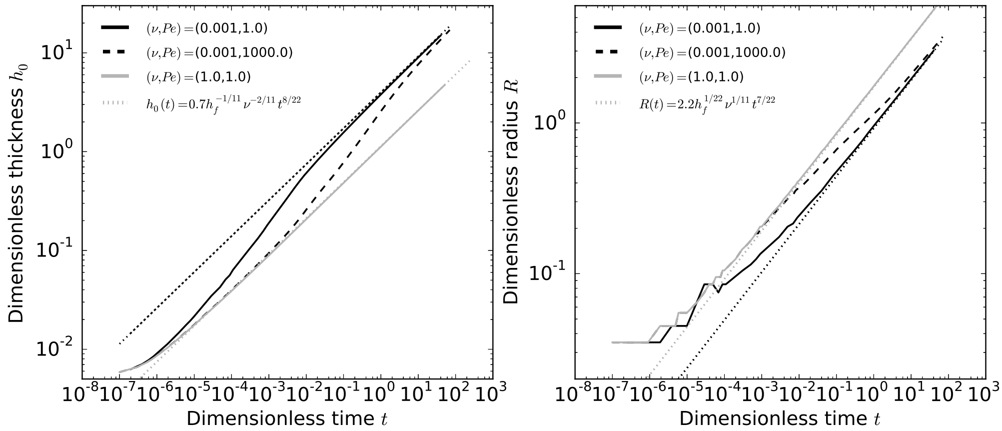

Figure 3.6: Left: Dimensionless thickness at the center h_0 versus dimensionless time t for different sets (ν, Pe) indicated on the plot. Dotted-lines: scaling laws $h_0 = 0.7 h_f^{-1/11} \nu^{-2/11} t^{8/22}$ for $\nu = 1.0$ and 0.001. Right: Dimensionless radius R versus dimensionless time t for the same sets (ν, Pe). Dotted-lines: the scaling laws $R = 2.2 h_f^{1/22} \nu^{1/11} t^{7/22}$ for $\nu = 1.0$ and 0.001.

thickness and time by $\nu^{1/4}$ and read

$$h_0 = 0.7 \nu^{-2/11} h_f^{-2/22} t^{8/22} \tag{3.82}$$

$$R = 2.2 \nu^{1/11} h_f^{1/22} t^{7/22}. \tag{3.83}$$

The dependence on the viscosity contrast ν indeed fits very well the third phase of the flow observed in the numerical simulations (Figure 3.6). These results suggest that the effective viscosity η_e that governs the flow dynamics is first close to the viscosity of the hot fluid; it rapidly increases in the second phase to asymptotically tend to the one of the cold fluid in the third phase.

The time the flow spends in each phase depends on the Peclet number Pe. For instance, for $\nu = 10^{-3}$, while the current leaves the first phase at $t \sim 10^{-6}$ for $Pe = 1.0$, this transition happens only after $t \sim 10^{-2}$ for $Pe = 10^3$ (Figure 3.6). The larger the Peclet number, the less efficient the cooling, and thus the longer the flow remains in the first phase and the later it reaches the third phase.

3.4.4 Characterization of the thermal anomaly

Following *Garel et al.* (2012), we quantify the size of the thermal anomaly through a critical thermal radius $R_c(t)$ where the temperature at the center of the flow Θ_b is 1% of the injection temperature, i.e. $\Theta_b(r = 0) - \Theta_b(r = R_c) = 0.99$.

The thermal anomaly is first advected at the same velocity as the current itself, i.e. $R(t) = R_c(t)$ (Figure 3.7 left). After a time that depends on Pe and ν, the thermal anomaly detaches from the tip and $R(t) - R_c(t)$ increases with time (Figure 3.7) .

In the bending regime, the interior pressure is constant and the thickness profile $h(r)$ is given by (3.49) (Figure 3.4). The size of the thermal anomaly $R_c(t)$ is given by the radius where advection of heat is equal to heat loss

$$\frac{d}{dt}\left(\theta(r = R_c, t)\right) \propto Pe^{-1}\frac{\partial^2}{\partial z^2}\left(\theta(r = R_c, t)\right). \tag{3.84}$$

Assuming that, at the edge of the thermal anomaly, θ is constant and close to Θ_b, i.e. $\theta \approx \Theta_b$, we obtain by integrating (3.84) over h and using (3.21)

$$\begin{aligned} \frac{d}{dt}\left(\int_0^h \theta dz\right) &\propto Pe^{-1}\frac{\Theta_b}{h} \\ \Theta_b\frac{dh}{dt} &\propto Pe^{-1}\frac{\Theta_b}{h} \\ \frac{dh}{dt} &\propto \frac{Pe^{-1}}{h}. \end{aligned} \tag{3.85}$$

Using the thickness profile (3.49), (3.85) becomes

$$\alpha^2\left(1+\frac{R_c}{R}\right)^2\frac{\partial h_0}{\partial t} + \frac{4h_0R_c^2}{R^3}\frac{\partial R}{\partial t}\alpha\left(1+\frac{R_c}{R}\right) = \frac{Pe^{-1}}{\alpha^2\left(1+\frac{R_c}{R}\right)^2 h_0}$$

where we introduce $\alpha(t) = \left(R(t) - R_c(t)\right)/R(t)$, i.e. the normalized region beyond $r = R_c(t)$. In the limit $\alpha << 1$, i.e. $R_c/R \sim 1$ and discarding higher-order terms, we finally get

$$\alpha^3 \propto \frac{Pe^{-1}}{h_0^2(t)}\frac{R}{\frac{\partial R}{\partial t}}. \tag{3.86}$$

Substituting the thickness $h_0(t)$ and the radius $R(t)$ by their respective scaling laws (3.82) and (3.83), the relative size of the normalized cold front region α reads

$$\alpha(t) \propto Pe^{-1/3}\nu^{4/33}h_f^{2/33}t^{1/11}. \tag{3.87}$$

which is equivalent to

$$R(t) - R_c(t) = 2.1Pe^{-1/3}\nu^{7/33}h_f^{7/66}t^{9/22} \tag{3.88}$$

where the numerically prefactor, which depends on the definition of the thermal anomaly, has been chosen to fit the simulations.

The predicted scaling law for the extent of the cold fluid region (3.88) indeed closely fits the numerical simulations for $\nu < 1$ and the different Peclet numbers (Figure 3.7). For $\nu = 1$ and $Pe = 1$, the condition $R - R_c << R$ is no more respected for $t > 0.1$, the thermal anomaly is much smaller than the flow itself and the scaling law (3.88) is no more applicable as expected.

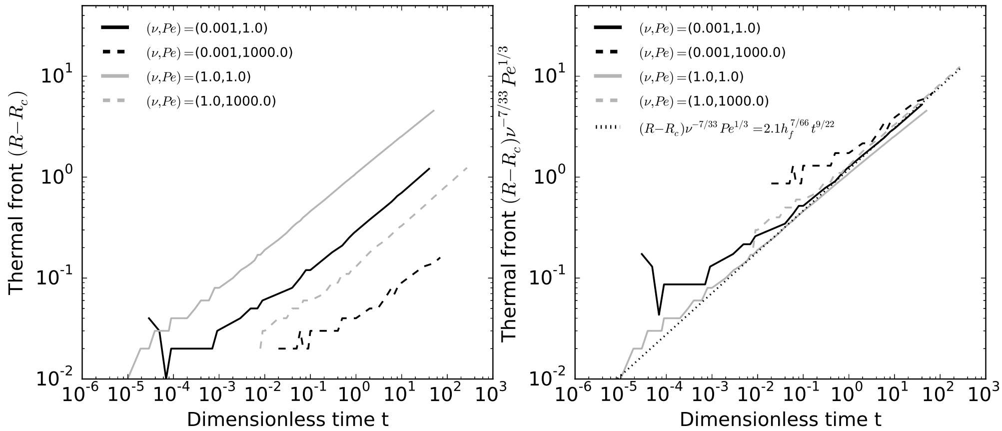

Figure 3.7: Left: Extent of the cold fluid region $R(t)-R_c(t)$ versus dimensionless time for different combinations (ν, Pe) indicated on the plot. Right: Same plot but where we rescale the extent of the cold fluid region by $Pe^{-1/3}\nu^{7/33}$. Dotted-line: scaling law $(R(t)-R_c(t))Pe^{1/3}\nu^{-7/33} = 2.1h_f^{7/66}t^{9/22}$.

3.4.5 Effective viscosity of the current

We use the predicted scaling law for the thickness $h_0(t)$ (3.82) to infer the time evolution of the effective viscosity $\eta_e(t)$. Indeed, substituting ν by $\eta_h/\eta_e(t)$ in (3.82) and inverting for $\eta_e(t)/\eta_h$, we get

$$\eta_e(t)/\eta_h \quad = \quad \left(\frac{h_0(t)t^{-8/22}}{0.7h_f^{-2/22}}\right)^{11/2} \tag{3.89}$$

where $h_0(t)$ is given by the simulation.

As suggested by the results of section 3.4.3, the effective viscosity is first close to the hot viscosity η_h, i.e. $\eta_e/\eta_h \sim 1$. It rapidly increases in the second phase of propagation and finally tends to the cold viscosity η_c in the third phase, i.e. $\eta_e/\eta_h \sim 1/\nu$ (Figure 3.8 top). The spreading in the isoviscous case is controlled by the propagation of a peeling by bending wave at the tip of the current (*Lister et al.*, 2013). In agreement, the behavior of the effective viscosity has to be linked with the rapid cooling of the front. To test this hypothesis, we calculate the average viscosity $\eta_f(t)$ over a fixed front region of size L in between $R(t)-L$ and $R(t)$ such that

$$\eta_f/\eta_h = \frac{1}{V_f}\int_{R-L}^{R}\int_0^h r\eta(\theta)drdz \tag{3.90}$$

where $V_f(t)$ is the volume of this region. The numerical evaluation of $\eta_f(t)$ for a constant size $L \sim 0.1$ gives a good agreement with the evolution of

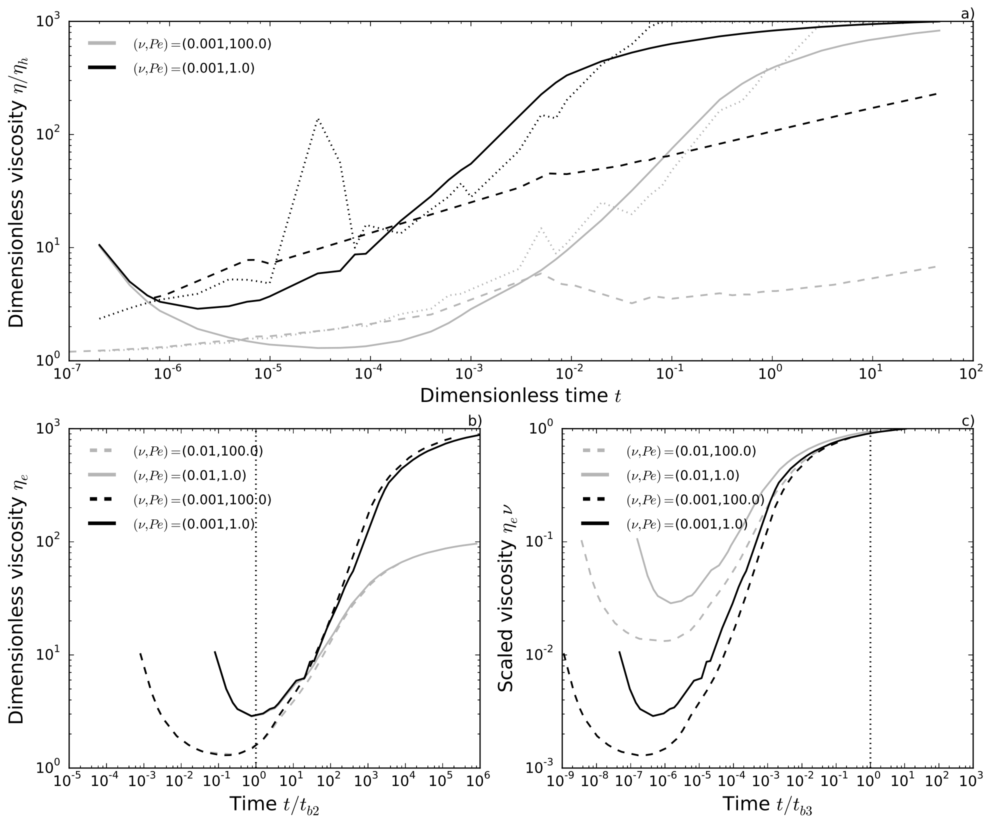

Figure 3.8: Top: Dimensionless viscosity $\eta(t)/\eta_h$ versus dimensionless time t for different combinations (ν, Pe) indicated on the plot. Solid lines: effective viscosity η_e/η_h defined by (3.89). Dashed-lines: average flow viscosity defined by $\overline{\eta_a(t)}/\eta_h = \frac{1}{V(t)}\int_0^{R(t)}\int_0^{h(r,t)} r\eta(\theta)drdz$ where $V(t)$ is the current volume. Dotted-lines: average front viscosity η_f/η_h defined by (3.90). Bottom left: dimensionless effective viscosity η_e versus time where the time has been rescaled by the time for the flow to enter the second phase t_{b2}. Bottom right: Same as left but where the time has been rescaled by the time for the flow to enter the third phase t_{b3}.

the effective viscosity η_e for the second phase of propagation (Figure 3.8). Therefore, the effective viscosity, and thus the different phases of propagation, are controlled by the average viscosity of a small region at the front of the current.

At the initiation of the flow, the pre-wetted film is composed by fluid at the injection temperature, the thermal anomaly is attached to the front and the current spreads with a hot viscosity η_h. As soon as the film has cooled, the thermal anomaly detaches from the tip of the current and the effective viscosity increases. The time t_{b2} the current enters this second phase of the flow thus scales as the time to cool the pre-wetted film thickness by conduction, i.e. $t_{b2} = 0.1 Pe h_f^2$ where the numerical prefactor has been matched to the simulations. Indeed, when rescaling the time of the simulations by t_{b2}, the different combinations (ν, Pe) enter the second phase simultaneously (Figure 3.8, bottom left). Then, the size of the cold fluid region at the front increases, the effective viscosity increases, and when $R(t) - R_c(t)$ becomes larger than ~ 0.1, the current behaves as an isoviscous current with cold viscosity η_c. Therefore, the time t_{b3} for the flow to enter this third phase scales as the time for the cold fluid region, whose size is given by (3.88), to be larger than ~ 0.1. In particular, we define the time t_{b3} as the time for the effective to reach 90% of its maximum value η_c. Inverting (3.88) and matching the numerical prefactor to the simulation thus gives $t_{b3} \sim 0.01 Pe^{22/27} \nu^{-14/27} h_f^{-7/27}$. Indeed, when rescaling the time of the simulations by t_{b3}, the different combinations (ν, Pe) enter the third phase simultaneously (Figure 3.8, bottom right).

3.4.6 Note on the effect of crystallization

Here, we examine the effect of crystallization on the flow dynamics and use values of $St_m < 1$. Crystallization induces a release of latent heat in the fluid, increasing the amount of available energy at a given time. When $St_m < 1$, the tip of the current remains hot for a longer time and the flow transitions to the second phase later than in the case where $St_m = 1$ (Figure 3.9). As the crystallization acts only to reduce the cooling term by a factor St_m in (3.46), one can easily rewrite (3.88) to acount for the effect of crystallization on the size of the cold fluid region

$$R(t) - R_c(t) = 2.1 Pe^{-1/3} St_m^{1/3} \nu^{7/33} h_f^{7/66} t^{9/22}. \tag{3.91}$$

Indeed, the dependence with the dimensionless number St_m is well described by the scaling law (3.91) (Figure 3.10). Accordingly, the time t_{b2} and t_{b3} for the current to enter the second and third phase of the flow respectively are

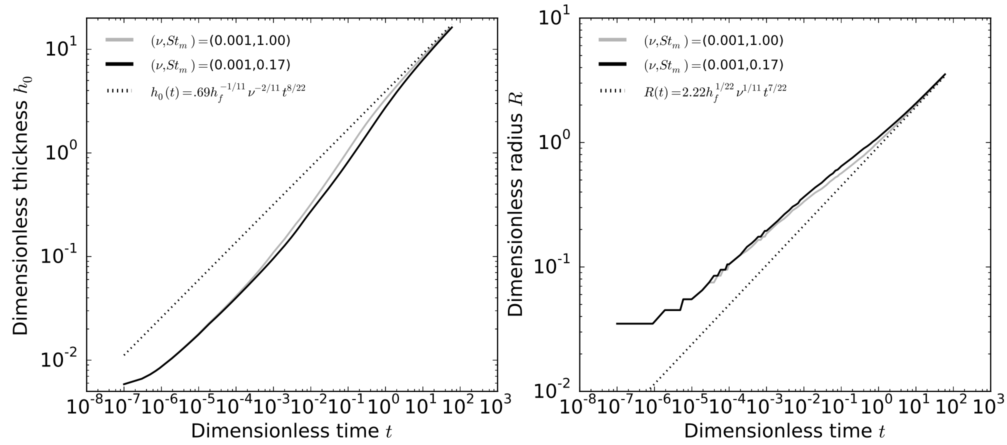

Figure 3.9: Left: Dimensionless thickness at the center h_0 versus dimensionless time t for different values of St_m indicated on the plot, $\nu = 0.001$ and $Pe = 10.0$. Dotted-line: scaling law $h_0 = 0.7 h_f^{-1/11} \nu^{-2/11} t^{8/22}$ for $\nu = 0.001$. Right: Dimensionless radius R versus dimensionless time t for the same combinations of dimensionless numbers. Dotted lines: scaling law $R = 2.2 h_f^{1/22} \nu^{1/11} t^{7/22}$ for $\nu = 0.001$.

delayed and when accounting for crystallization read

$$t_{b2} \sim 0.1 Pe St_m^{-1} h_f^2 \tag{3.92}$$

$$t_{b3} \sim 10^{-2} St_m^{-22/27} Pe^{22/27} \nu^{-14/27} h_f^{-7/27} \tag{3.93}$$

3.5 Evolution in the gravity current regime

To study the late time behavior, we concentrate on the case where only the weight of the fluid contributes to the pressure. The governing equation are thus (3.45) and (3.46) where $P = h$. We follow the same development as in Section 3.4. In particular, we first describe the thermal structure for an isoviscous flow, i.e. $\nu = 1$, then we study the effect of the temperature-dependent viscosity on the current dynamics without crystallization, i.e. $\nu < 1$ and $St_m = 1$. Finally, we look at the effect of crystallization by setting $St_m < 1$.

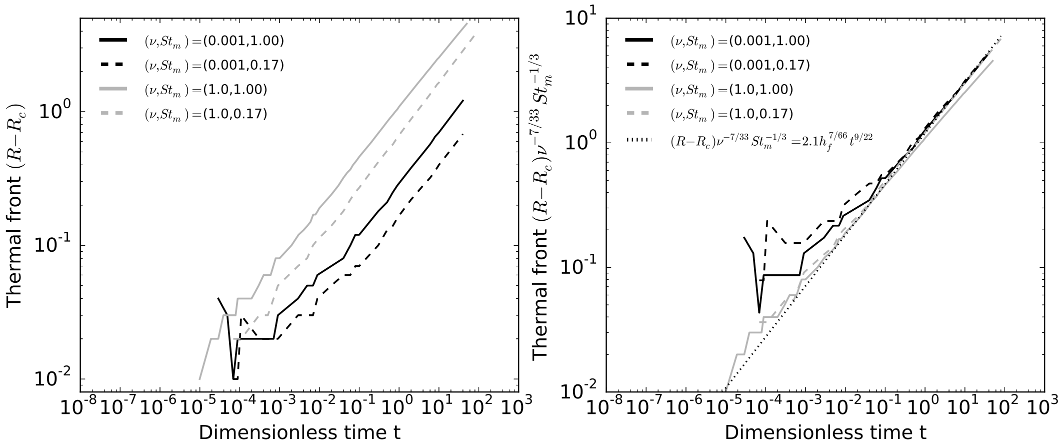

Figure 3.10: Left: Extent of the cold fluid region $R(t)-R_c(t)$ versus dimensionless time for different combinations (ν,St_m) indicated on the plot and $Pe = 1$. Right: Same plot but where we have rescaled the extent of the cold fluid region by $St_m^{1/3}\nu^{7/33}$. Dotted-line: scaling law $(R(t) - R_c(t))St_m^{-1/3}\nu^{-7/33} = 2.1h_f^{7/66}t^{9/22}$.

3.5.1 Thermal structure for an isoviscous flow, effect of Pe

As in the bending regime, the bulk of the fluid first expands at the injection temperature and $R_c \sim R$. As the bottom and the top cool by conduction, thermal boundary layers form at the contact with the surrounding medium and connect at the tip of the current. However, in the gravity current regime, the thickness of the current tends to a constant. Therefore, conduction in the surrounding medium rapidly balances the input of heat at the center and when the thermal anomaly detaches from the tip of the current, its extent reaches a steady state profile (Figure 3.11).

The radius of the steady state thermal anomaly R_c depends on Pe. In particular, the larger the number Pe, the larger the radius R_c is. For instance, for $\nu = 1$, while the thermal anomaly R_c is less than 1 in the steady state regime for $Pe = 1$, it is about 12 for $Pe = 10^3$ (Figure 3.12).

3.5.2 Thickness and temperature profile, effect of ν

For a current with a viscosity that depends on temperature, as soon as the thermal anomaly detaches from the current radius, the cold fluid at the front tends to slow down the spreading and enhance the thickening of the flow

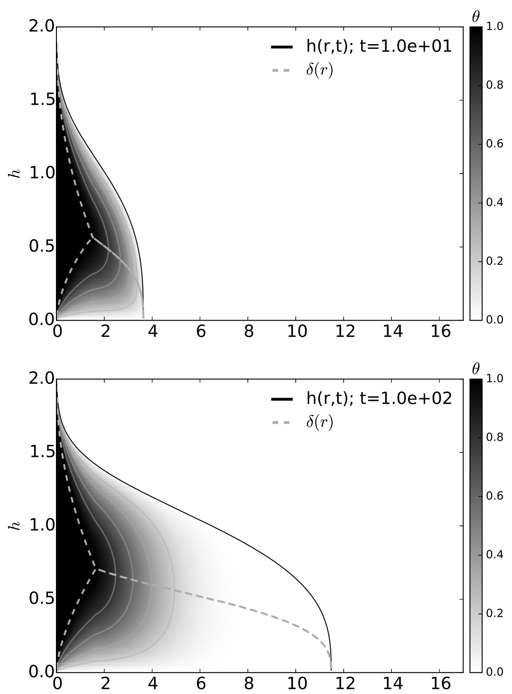

Figure 3.11: Snapshots of the flow thermal structure $\theta(r, z, t)$ at different times indicated on the plot. Dashed lines: thermal boundary layers. Here, $\nu = 1$, $Pe = 100$ and $St_m = 1$.

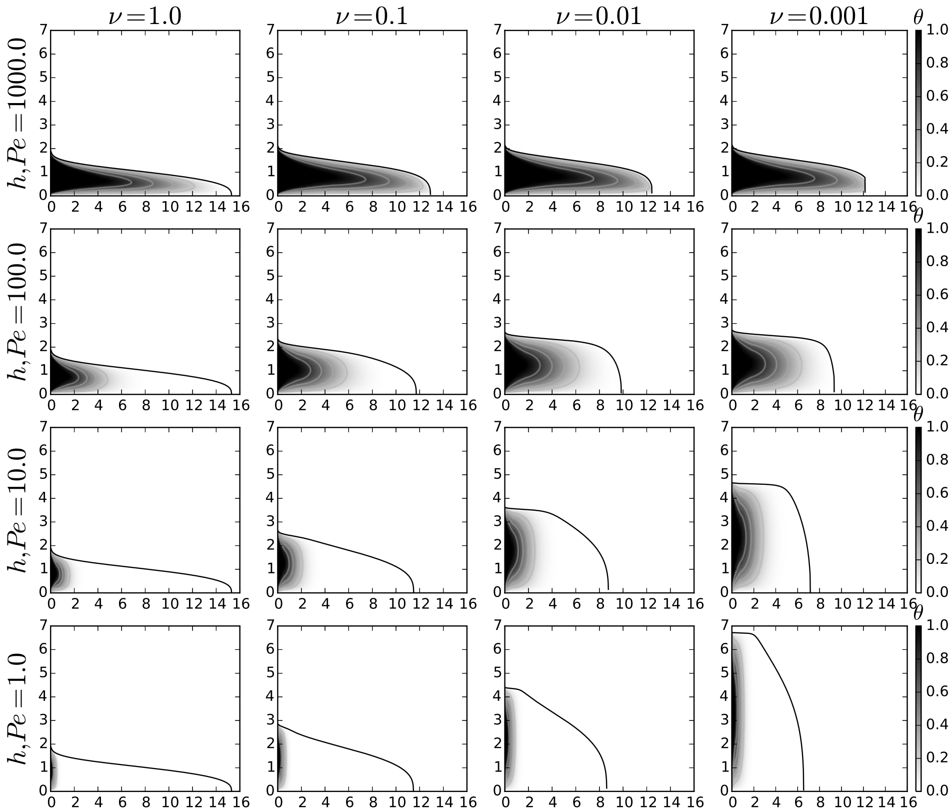

Figure 3.12: Snapshots of the flow thermal structure $\theta(r, z, t)$ for different sets (ν,Pe) with $\nu = 1$,0.1 ,0.01 and 0.001 and $Pe = 1$, 10, 100 and 1000 at $t = 200$.

(Figure 3.12). For instance, for $Pe = 1$, while the aspect ratio h_0/R is about 0.12 for $\nu = 1$ at $t = 200$, it is ~ 1 for $\nu = 10^{-3}$ (Figure 3.12). The shape of the current is not self-similar and the front steepens when the viscosity increases in comparison to the isoviscous case as in *Bercovici* (1994). However, when the current becomes much larger than the thermal anomaly, the current side slumps to become less steep (Figure 3.12) and recovers a shape similar to the isoviscous flow with cold viscosity.

The thermal structure is similar to the isoviscous case. In particular, after a time that depends on Pe, the thermal anomaly reaches a steady-state profile (Figure 3.12). As in the bending regime, the thickening at the center limits heat loss to the surrounding for large values of the viscosity contrast ν. Therefore, the extent of the thermal anomaly in the steady-state is slightly larger for a larger viscosity contrast. For instance, for $Pe = 10$ at $t = 200$, while the thermal anomaly extends over less than 2 for $\nu = 1$, it reaches $Rc \sim 3$ for $\nu = 10^{-3}$.

The flow morphology is more sensitive to the Pe number in the gravity current regime than in the bending regime and different Pe lead to different current morphologies for a given ν (Figure 3.12). For instance, for $\nu = 10^{-3}$ at $t = 200$, the thermal anomaly is still attached to the tip of the current for $Pe = 10^3$ and the aspect ratio of the flow h_0/R is close to 0.15. In contrast, for $Pe = 1$, the thermal anomaly radius R_c is less than 30% of the current radius and the aspect ratio of the flow is much larger $h_0/R = 1.15$ (Figure 3.12).

3.5.3 Evolution of the thickness and the radius

As in the bending regime, the dynamics show three different spreading phases. The thickness as well as the radius first follow the isoviscous scaling laws for a given hot viscosity η_h, i.e. h_0 tends to a constant and $R \propto t^{1/2}$ (Figure 3.13). In a second phase, the thickness rapidly increases and the spreading slows down. Finally, the thickness and radius follow the isoviscous scaling laws but for a cold viscosity flow.

These dimensionless scaling laws read, as a function of ν

$$h_0 = 2.1\nu^{-1/4} \tag{3.94}$$

$$R(t) = 1.1\nu^{1/8}t^{1/2} \tag{3.95}$$

They perfectly matched our numerical simulations (Figure 3.13). Therefore, the effective viscosity η_e that controls the flow dynamics is first close to the viscosity of the hot fluid η_h; it then rapidly increases to asymptotically tend to the viscosity of the cold fluid η_c in the third phase.

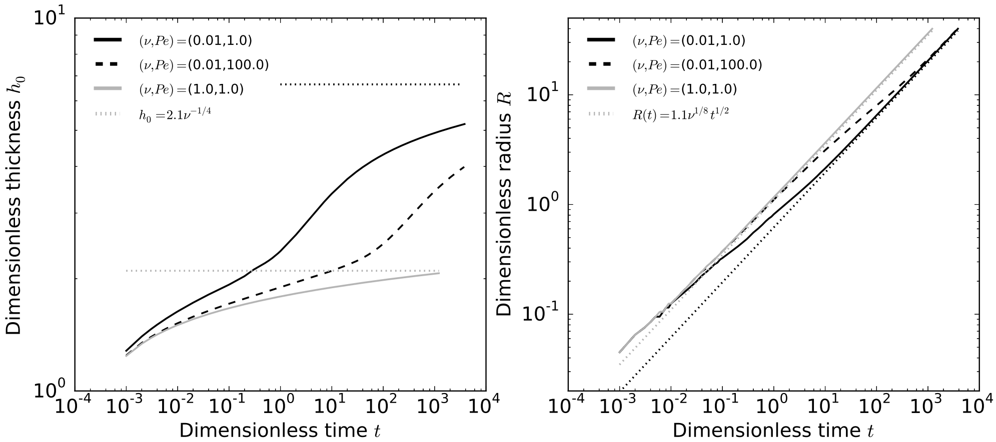

Figure 3.13: Left: Dimensionless thickness at the center h_0 versus dimensionless time t for different sets (ν, Pe) indicated on the plot. Dotted-lines represent the scaling laws $h_0 = 2.1\nu^{-1/4}$ for $\nu = 1.0$ and 10^{-2}. Right: Dimensionless radius R versus dimensionless time t for the same sets (ν, Pe). Dotted-lines represent the scaling laws $R = 1.1\nu^{1/8}t^{1/2}$ for $\nu = 1.0$ and 10^{-2}.

As in the bending regime, the time the current spends in each phase depends on Pe (Figure 3.13). For instance, for $\nu = 10^{-2}$, while the current leaves the first phase at $t \sim 10^{-1}$ for $Pe = 1.0$, the transition occurs after $t \sim 10^1$ for $Pe = 10^2$. In general, the larger Pe, the longer the current remains in the first phase and the later is reached the third phase.

3.5.4 Characterization of the thermal anomaly

The thermal anomaly is first advected at the same velocity as the current itself, i.e. $R_c(t)/R(t) \sim 1$ (Figure 3.14 left). After a time that depends on Pe and ν, the thermal anomaly detaches from the front and reaches a steady-state profile (Figure 3.12 and 3.14).

We propose a simple thermal budget to predict the extent of the thermal anomaly in the steady-state regime. When the size of the thermal anomaly reaches a steady state, a balance between heat advection and diffusion in the surrounding medium in a dimensional form gives

$$\rho C_p U_0 \frac{\Delta T}{R_c} = \frac{8k\Delta T}{h_0^2} \tag{3.96}$$

where ΔT hold for a mean temperature contrast between the fluid and the surroundings advected at a mean velocity U_0. For a gravity current, and by opposition to the bending regime, the thickness h_0 reaches a constant. Taking

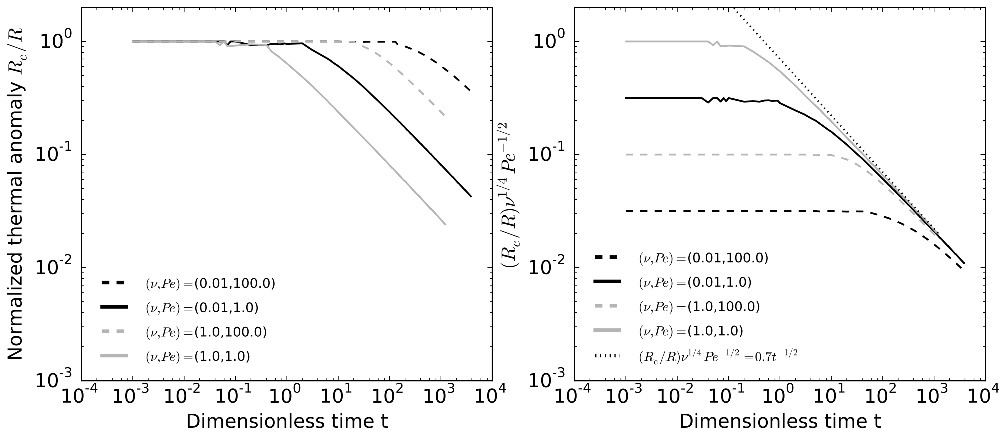

Figure 3.14: Left: Normalized thermal anomaly radius $R_c(t)/R(t)$ versus dimensionless time for different combinations (ν,Pe) indicated on the plot. Right: Same plot but where we rescale the normalized thermal anomaly radius $R_c(t)/R(t)$ by $Pe^{1/2}\nu^{-1/4}$.

U_0 as a horizontal redistribution of the injection rate, we write

$$U_0 = Q_0/(2\pi R_c h_0) \tag{3.97}$$

which gives

$$R_c = \frac{1}{4}\sqrt{\frac{h_0 Q_0}{\pi\kappa}} \tag{3.98}$$

By non-dimensionalizing (3.98), we finally get the expression for the thermal anomaly radius R_c in the steady state regime. In particular, we have $R_c \propto Pe^{1/2}\nu^{-1/8}$ and then

$$\frac{R_c}{R(t)} = 0.7Pe^{1/2}\nu^{-1/4}t^{-1/2} \tag{3.99}$$

where we have used (3.95) and the numerical prefactor, which depends on the definition of the thermal anomaly, has been chosen to fit the simulations.

The analytical solution for the normalized thermal anomaly radius $R_c/R(t)$ (3.99) closely fits the numerical simulations (Figure 3.14). Indeed, when the thermal anomaly enters the steady state, the thermal anomaly radius remains constant and the normalized thermal anomaly radius $R_c(t)/R(t)$ evolves as the inverse of the current radius, i.e. as $t^{-1/2}$ (Figure 3.14). Furthermore, both the dependence with Pe and ν vanish when rescaling $R_c/R(t)$ by $Pe^{1/2}\nu^{-1/4}$ in the steady state regime (Figure 3.14, right).

3.5.5 Effective viscosity of the current

Repeating the same exercise as in section (3.4.5), we use the predicted scaling law for the radius $R(t)$ (3.95) to infer the effective viscosity $\eta_e(t)$ of the current

$$\eta_e(t)/\eta_h = \left(\frac{R(t)t^{-1/2}}{1.1}\right)^{-8}. \tag{3.100}$$

As expected, the effective viscosity in the gravity current regime represents the average viscosity of the current and the different phases of propagation reflect changes in the average viscosity of the flow (Figure 3.15).

At flow initiation, the thermal anomaly is advected at the same velocity as the current itself and the current spreads with hot viscosity η_h. When the thermal anomaly detaches from the tip and enters a steady state, η_e increases. The time t_{g2} to enter this second phase scales with the time to cool the current by conduction, i.e. $t_{g2} = 10^{-2}Pe$ where the numerical pre-factor has been matched to the simulations. Indeed, when rescaling the time by t_{g2}, the different combinations (ν, Pe) enter the second phase simultaneously (Figure 3.15, bottom left). Then, the size of the cold fluid region at the front increases, the effective viscosity increases and, when the current is large compared to the steady-state thermal anomaly radius, i.e. $R_c/R < 0.6$ the current behaves as an isoviscous current with cold viscosity η_c. Therefore, the time t_{g3} for the flow to enter this third phase scales as the time for the normalized thermal anomaly radius to be smaller than ~ 0.6. As in the bending regime, we define the time t_{g3} as the time for the effective to reach 90% of its maximum value η_c. Inverting (3.88) and matching the numerical prefactor to the simulation thus gives $t_{g3} = 5Pe\nu^{-1/2}$. In agreement, when rescaling the time of the simulations by t_{g3}, the different combinations (ν, Pe) enter the third phase simultaneously (Figure 3.15, bottom right).

3.5.6 Note on the effect of crystallization

As in the bending regime, crystallization induces a release of latent heat to the fluid, increasing the amount of available energy at a given time. As a result, when $St_m < 1$, the current is hotter on average and it transitions to the second phase later than in the case where $St_m = 1$ (Figure 3.16). As in section (3.4.6), one can easily rewrite (3.99) to account for the effect of crystallization on the thermal anomaly evolution

$$\frac{R_c}{R(t)} = 0.7St_m^{-1/2}Pe^{1/2}\nu^{-1/4}t^{-1/2} \tag{3.101}$$

Indeed, the dependence with the dimensionless number St_m is well described by the scaling law (3.101) (Figure 3.17). Accordingly, the time t_{g2} and t_{g3} for

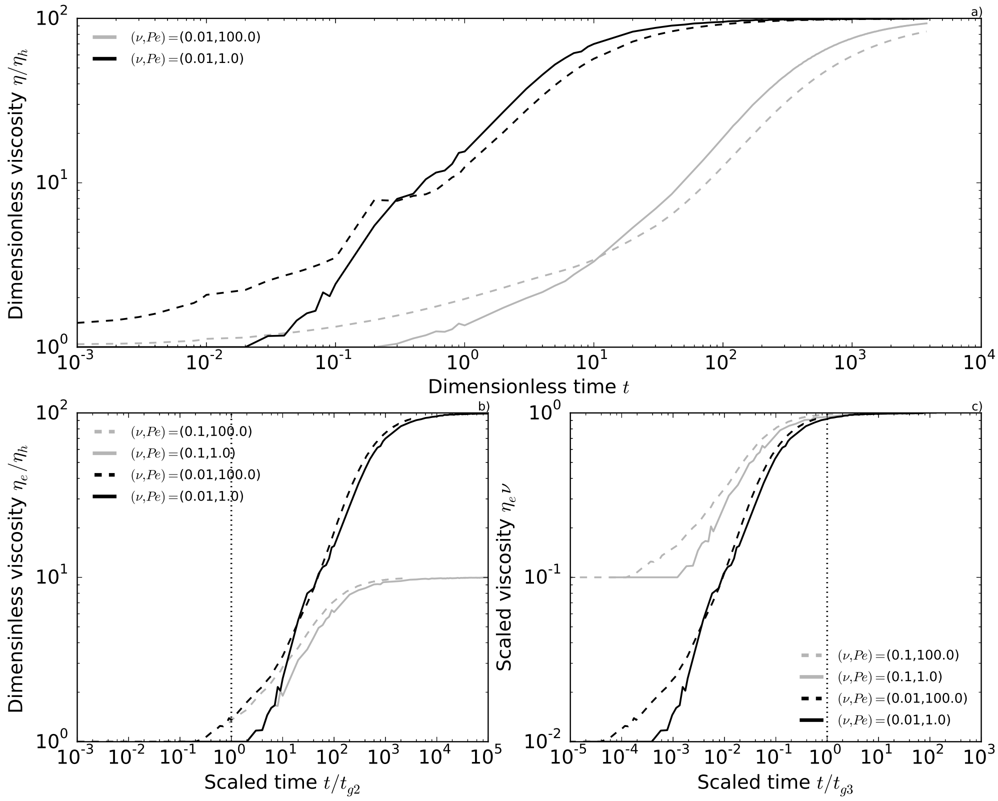

Figure 3.15: Top: Dimensionless viscosity $\eta(t)/\eta_h$ versus dimensionless time t for different combinations (ν, Pe) indicated on the plot. Solid lines: effective viscosity η_e/η_h defined by (3.89). Dashed-lines: average flow viscosity defined by $\overline{\eta_a(t)}/\eta_h = \frac{1}{V(t)}\int_0^{R(t)}\int_0^{h(r,t)} r\eta(\theta)drdz$ where $V(t)$ is the current volume. Bottom left: dimensionless effective viscosity η_e versus time where the time has been rescaled by the time t_{g2} (3.102). Bottom right: Same as left but where the time has been rescaled by t_{g3} (3.103).

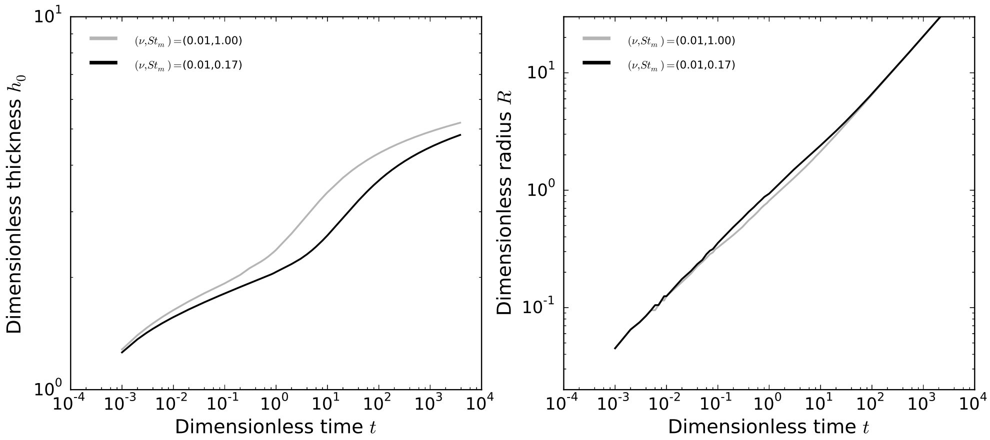

Figure 3.16: Left: Dimensionless thickness at the center h_0 versus dimensionless time t for different sets (ν, St_m) indicated on the plot and $Pe = 1$. Right: Dimensionless radius R versus dimensionless time t for the same sets (ν, St_m) and $Pe = 1$.

the current to enter the second and third phase of the flow are both delayed and finally read

$$t_{g2} \sim 10^{-2} Pe St_m^{-1} \tag{3.102}$$

$$t_{g3} \sim 5 Pe St_m^{-1} \nu^{-1/2} \tag{3.103}$$

3.6 Different evolutions with bending and gravity

For an isoviscous flow with $h_f << h << d_c$, the flow passes through three asymptotic dynamical regimes (*Michaut*, 2011; *Lister et al.*, 2013). When the radius R is much smaller than a critical radius $R_c \sim 4$, the interior solution is bell-shaped and peeling by bending controls propagation. In contrast, when $R >> R_c$, bending stresses can be neglected almost everywhere and the flow enters a gravity current regime. In between, *Lister et al.* (2013) also describe a short intermediate regime where the peeling by bending continues to control the propagation but where the flow shows an interior flat-topped region due to the increasing effect of gravity. For simplicity, we only consider the two asymptotic regimes. At the transition, the isoviscous current is characterized by $R \sim 4$, $h_0 \sim 2$ and $t \sim 10$. In the following, we consider a modified Peclet number $Pe_m = Pe St_m^{-1}$ which integrates the effect of crystallization for clarity.

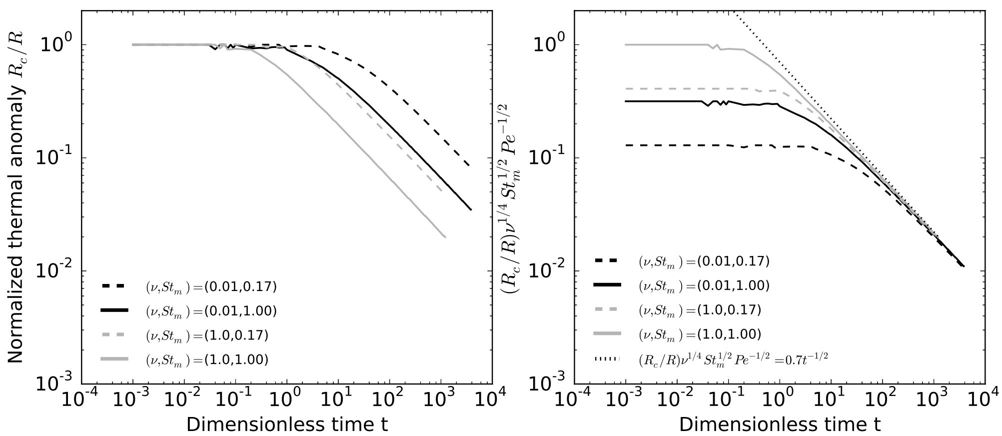

Figure 3.17: Left: Normalized thermal anomaly radius $R_c(t)/R(t)$ versus dimensionless time for different combinations (ν,St_m) indicated on the plot and $Pe = 1$. Right: Same plot but where we have rescaled the normalized thermal anomaly radius $R_c(t)/R(t)$ by $St_m^{-1/2}Pe^{1/2}\nu^{-1/4}$.

For a current with a temperature dependent viscosity, the transition between the bending regime and the gravity regime also occurs when the radius of the current is close to $R \sim 4$ (Figure 3.18). However, the time and thickness of the current at the transition depends on the thermal state of the flow, i.e. on the combination of (ν,Pe_m) considered (Figure 3.18). For instance, for $\nu = 0.01$ and a small value of Pe, i.e. $Pe = 1.0$ the current transitions to the gravity regime when it is in the third thermal phase of the bending regime, i.e. at $t \sim 50$ with $h_0 \sim 8$, as an isoviscous current with given cold viscosity $\eta_c = 100$. In contrast, for a larger value of Pe, i.e. $Pe = 10^5$, the current remains longer in the first phase of the bending regime and it spreads with hot viscosity η_h for a longer period of time. As a consequence, it reaches the transition sooner at $t \sim 30$ and with a smaller thickness $h_0 \sim 5$ when it is still in the second thermal phase of the bending regime. For an even larger Peclet number Pe, the current will transition in the first thermal phase of the bending regime at $t \sim 10$ and with $h_0 \sim 2$, as in the isoviscous case with viscosity η_h.

Overall, the time for the current to reach the transition t_t is the time for its radius to be larger than 4. It can be obtained from the scaling law followed by the radius $R(t)$ in the bending regime (3.83) and is equal to $6.5(\eta_e/\eta_h)^{2/7}h_f^{-1/7}$ where η_e is the effective viscosity of the current (see Section 3.4.5). In particular, it is bound by two values corresponding to two end-member cases: the case where the current transitions to the gravity regime while it is in the first bending phase, i.e. when $\eta_e = \eta_h$ and $t_h \sim 6.5h_f^{-1/7}$

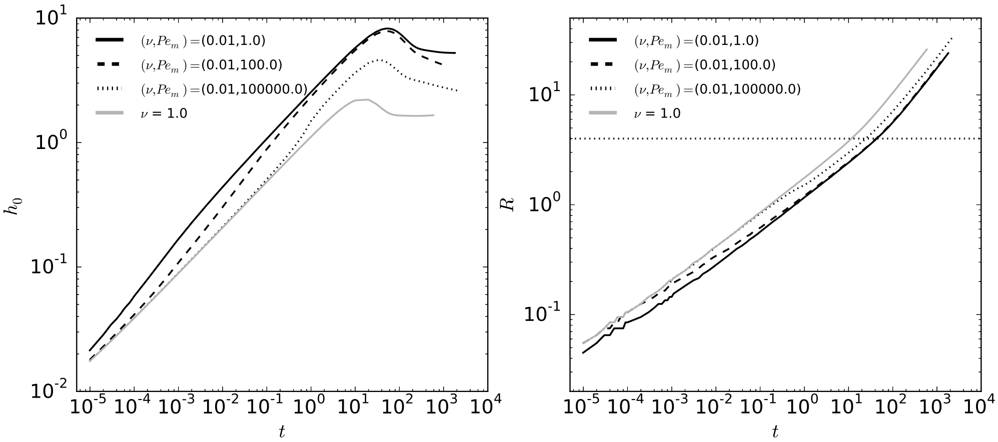

Figure 3.18: Left: Dimensionless thickness at the center h_0 versus dimensionless time for different sets (ν, Pe) indicated on the plot. The grey line represents the isoviscous case $\nu = 1$. Right: Same plot but for the dimensionless radius R. Horizontal black dotted-line represents the transition radius between the bending and the gravity regime.

and the case where the current transitions to the gravity regime while it is in the third bending phase, i.e. $\eta_e = \eta_c$ and $t_c \sim 6.5\nu^{-2/7}h_f^{-1/7}$. Indeed, when rescaling the time of the simulation by t_c, the different combinations (ν,Pe_m), for which the third thermal phase of the bending regime has been reached before the transition to the gravity regime, collapse on the same curve (Figure 3.19, right).

The subsequent evolution in the gravity regime also depends on the combinations (ν,Pe_m) considered. Indeed, in contrast to the bending regime where the effective viscosity is that of a small region at the tip, the effective viscosity is the average flow viscosity in the gravity regime. Therefore, the effective viscosity of the flow can drastically decrease when entering the gravity regime and a flow in the ith thermal phase of the bending regime can transition in the jth thermal phase of the gravity regime with $i \geq j$ which results in 6 possible scenarios (see Appendix 3.8 for more details). For instance, a current in the second thermal phase of the bending regime can transition into the first or second thermal phase of the gravity current regime. However, the case where a current in the third thermal phase of the bending regime transitions to the first thermal phase of the gravity regime is not possible and in the following, we details the five remaining scenarios as a function of the combination (ν, Pe_m) considered.

We first consider the case where the current transitions to the gravity

Name	From	To	Expression
t_t	Bending	Gravity	$6.5(\eta_e/\eta_h)^{2/7}h_f^{-1/7}$
t_h	Bending	Gravity	$6.5h_f^{-1/7}$
t_c	Bending	Gravity	$6.5\nu^{-2/7}h_f^{-1/7}$
Bending regime			
t_{b2}	Phase 1	Phase 2	$0.1PeSt_m^{-1}h_f^2$
t_{b3}	Phase 2	Phase 3	$10^{-2}St_m^{-22/27}Pe^{22/27}\nu^{-14/27}h_f^{-7/27}$
Gravity regime			
t_{g2}	Phase 1	Phase 2	$10^{-2}PeSt_m^{-1}$
t_{g3}	Phase 2	Phase 3	$5PeSt_m^{-1}\nu^{-1/2}$

Table 3.1: Summary of the different transition times. t_t is the transition time between bending and gravity which is bound by t_h, when the current transitions in the first bending thermal phase, and t_c, when the current transitions in the third bending thermal phase. t_{b2} (resp. t_{b3}) represents the time to transition from phase 1 to phase 2 (resp. from phase 2 to phase 3) in the bending regime. t_{g2} (resp. t_{g3}) represents the time to transition from phase 1 to phase 2 (resp. from phase 2 to phase 3) in the gravity regime.

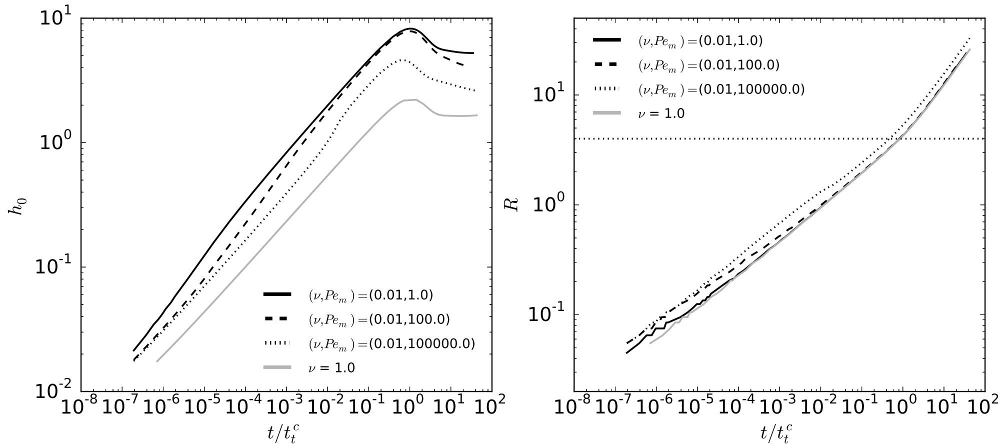

Figure 3.19: Left: Dimensionless thickness at the center h_0 versus time where the time has been rescaled by the time t_c the current transitions to the gravity regime while it is in the third bending phase (Table 3.1). The grey line represents the isoviscous case with given viscosity η_h. Right: Same plot but for the dimensionless radius R. Horizontal black dotted-line represents the transition radius between the bending and the gravity regime.

regime in the first thermal phase of the bending regime. In that case, the time for the transition is t_h and is less than the time for the second bending thermal phase change t_{b2}; comparing t_h and t_{b2} gives $Pe > 65h_f^{-15/7}$ (Figure 3.20, Table 3.1). As $t_h < t_{g2}$ for $Pe > 65h_f^{-15/7}$, the current then transitions to the first thermal phase of the gravity current regime (B_1G_1 in Figure 3.20 and Figure 3.22, Table 3.2 in Appendix 3.8).

At the opposite, if the current has reached the third thermal bending phase, the transition occurs at t_c and is necessarily larger than t_{b3}; comparing t_c and t_{b3} gives $\nu > 8.3 \cdot 10^{-13} Pe_m^{7/2} h_f^{-1/2}$ (Figure 3.20, Table 3.1). As $t_c > t_{g2}$ for $\nu > 8.3 \cdot 10^{-13} Pe_m^{7/2} h_f^{-1/2}$, the current can either transition to the second or third thermal phase of the bending regime (Figure 3.22, Table 3.2 in Appendix 3.8). If it transitions to the second phase of the gravity regime, then comparing t_c and t_{g3} gives $\nu < 0.3 Pe_m^{14/3} h_f^{2/3}$ (B_3G_2 on Figure 3.20) and if it transitions to the third phase of the gravity current, then $\nu > 0.3 Pe_m^{14/3} h_f^{2/3}$ (B_3G_3 on Figure 3.20).

In the case where the transition occurs when it is in the second bending phase, the time for the transition is not exactly known. However, it is bounded by t_h and t_c and we can therefore predict some evolution scenarios. Indeed, the transition time is necessarily smaller than t_c. Therefore, if $t_c < t_{g2}$, i.e. $\nu > 7.0 \cdot 10^9 Pe_m^{-7/2} h_f^{-1/2}$, the transition time is also smaller than t_{g2} and the current transitions to the first gravity thermal phase (B_2G_1 on Figure 3.20). Similarly, if $t_h > t_{g2}$, i.e. $Pe_m < 650h_f^{-1/7}$, then the transition time is larger than t_{g2} and the current transitions to the second gravity current phase (B_2G_2 on Figure 3.20).

3.7 Application to the arrest of terrestrial laccoliths

At shallow depth in the upper crust, roof lifting is the dominant process by which magma makes room for itself, which leads to the formation of laccoliths by bending of the overlying strata (*Johnson and Pollard*, 1973; *Pollard and Johnson*, 1973). The isoviscous elastic-plated gravity current model has been used to study their formation and show that their bell-shaped morphology is consistent with their arrest in the bending regime (*Michaut*, 2011; *Bunger and Cruden*, 2011). However, their radius is too small to be fractured controlled and their arrest might be better explained by their cooling (*Michaut*, 2011).

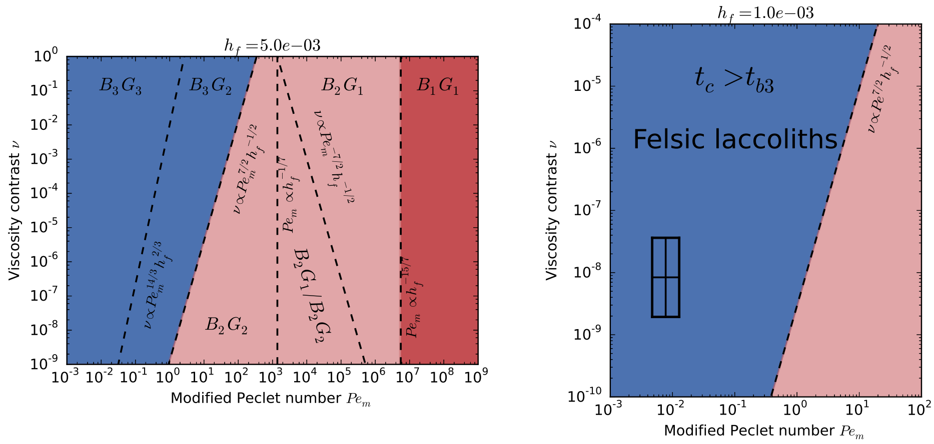

Figure 3.20: Left: Phase diagram for the evolution with bending and gravity for different combinations (ν,Pe_m) and a given value of $h_f = 0.005$. B_iG_j refers to the case where the current transitions from the ith bending thermal phase to the jth gravity thermal phase where i and $j \in \{1, 2, 3\}$. Right: Application to the spreading of laccoliths on a subset of the parameter space relevant for the study of terrestrial laccoliths described in Section 3.7.2. Rectangle: subset of the parameter space containing the laccoliths from *Rocchi et al.* (2002)

3.7.1 Range of values for the dimensionless numbers

For a lava density ρ_m of 2500 kg m^{-3}, Young's modulus values between 10 and 100 GPa and intrusion depths between 0.5 and 5 km, the characteristic length scale Λ varies between 1 and 10 km. The overpressure in magma reservoirs driving dykes is typically between a few to several tens of MPa (*Tait et al.*, 1988; *Martí*, 2000) and the conduit length Z_c varies from a few to several tens of kilometers. Lava viscosity at eruption temperature η_h depends mainly on its composition and water content; close to its liquidus temperature, it can varies from 10^3 to 10^6 Pa s for felsic lavas (*Shaw*, 1972; *Giordano et al.*, 2008; *Whittington et al.*, 2009; *Chevrel et al.*, 2013). Hence, injection rate Q_0 are in a range $0.01 - 1$ m^3 s^{-1}, the height scale H varies between 0.1 m and 2 m and the time scale τ varies from several months to a few years.

For a latent heat of crystallization $L = 4.18\ 10^5$ J kg^{-1}, a difference between solidus temperature T_S and liquidus temperature T_L between 100 K and 300 K, the number St_m varies from 0.1 to 0.5. For a thermal diffusivity for the magma equal to $\kappa_m = 10^{-6}$ m s^{-2}, the Peclet number can varies from 10^{-4} to 10 and therefore, Pe_m varies from 0.001 to 100. Finally, the increase in viscosity upon cooling can varies from 4 to 10 orders of magnitude (*Shaw*, 1972; *Lejeune and Richet*, 1995; *Giordano et al.*, 2008; *Diniega et al.*, 2013). We thus consider values of ν that vary between 10^{-4} and 10^{-10}.

The model also considers a thin pre-wetted film of thickness h_f whose meaning in the application to the spreading of laccolith is unclear. In particular, the model shows no convergence when h_f tends to zero (*Lister et al.*, 2013) and therefore, the thickness h_f might be linked to some structural length scale at the front of the laccolith or to the natural imperfection of the flow geometry. For the purpose of the application, we choose a film thickness of 1 mm, i.e. the minimum length scale with physical signification for the spreading of laccoliths which give a dimensionless h_f that varies between 10^{-2} and 10^{-4}. The limited effect of changing h_f is detailed in Appendix 3.8 and in the following, we set h_f to 10^{-3}.

It is generally assume that magma stops spreading when its crystal content becomes close to its maximum packing, i.e. $\phi \sim 60\%$ (*Pinkerton and Stevenson*, 1992). Beyond this point, crystal collisions dominate and the viscosity jumps to much higher values (*Lejeune and Richet*, 1995; *Giordano et al.*, 2008). We assume that this is equivalent to η_e tending to η_c in our model. With this assumption, the model thus predicts that a magmatic intrusion would solidify as a laccolith upon reaching the third thermal phase of the bending regime. The phase diagram proposed in Section 3.6 simplifies and predicts that most felsic magmatic intrusions should indeed solidify as a laccolith (Figure 3.20, right).

3.7.2 Comparison with observations

Rocchi et al. (2002) provide data for the intrusion size and depth of nine laccoliths at Elba Island, Italy. The length and thickness scales can be estimated for each laccolith such that the data can be nondimensionalized and compare to the model. In particular, the thickness h_0 as a function of its radius R for a current that solidifies in the third phase of the bending regime can be derived from the scaling laws (3.82) and (3.83) and should follow

$$h_0 \sim 0.75\nu^{-2/7}R^{8/7} \tag{3.104}$$

For this example, each laccolith is part of a larger intrusive system, and hence variability of the model parameters should be limited, except for the overlying elastic layer thickness, taken to be the intrusion depth, whose variation between laccoliths is accounted for in the nondimensionalization. The observations show a very good agreement with the model for a viscosity contrast close to 8 orders of magnitude, which is consistent with the felsic composition of these laccoliths (Figure 3.21, left) (*Marsh*, 1981; *Diniega et al.*, 2013).

If the laccoliths have stopped spreading as soon as they reached the third phase of the bending regime, the variance in thickness and radius between the different intrusions should be explained only by variations in the Peclet number, most likely due to variations in intrusion depths in this example. Indeed, in Section (3.5.5), we show that the time t_{b3} the current reaches the third phase of the bending regime, and hence its thickness and its radius at this time, depends on the combination (ν,Pe_m) considered. To test this hypothesis, we estimate for each laccolith its Peclet number Pe using its corresponding depth of intrusion and use for the viscosity contrast $\nu = 8.2 \cdot 10^{-9}$ determined previously (Figure 3.20 and 3.21 right). Then, we rescale the variables using the time t_{b3} (3.93) as follow

$$\hat{t} = Pe_m^{-22/27}\nu^{14/27}t \quad \hat{R} = Pe_m^{-7/27}\nu^{2/27}R \quad \hat{h_0} = Pe_m^{-8/27}\nu^{-10/27}h_0. \tag{3.105}$$

In term of $\hat{h_0}$ and $\hat{R}$, the scaling law (3.104) rewrites $\hat{h_0} \sim 0.75\hat{R}^{8/7}$ and does not depend on the dimensionless numbers anymore. However, the different laccoliths do not collapse on the same dot after rescaling. In particular, the dependence of Pe of our scaling, resulting from different intrusion depths, is not enough to explain the variability in the size of terrestrial laccoliths. An additional cooling mechanism, depending on Pe, is thus required to explain the exact extent of laccoliths, which could be extraction of heat by circulation of fluid or heating of the wall rocks during the intrusion.

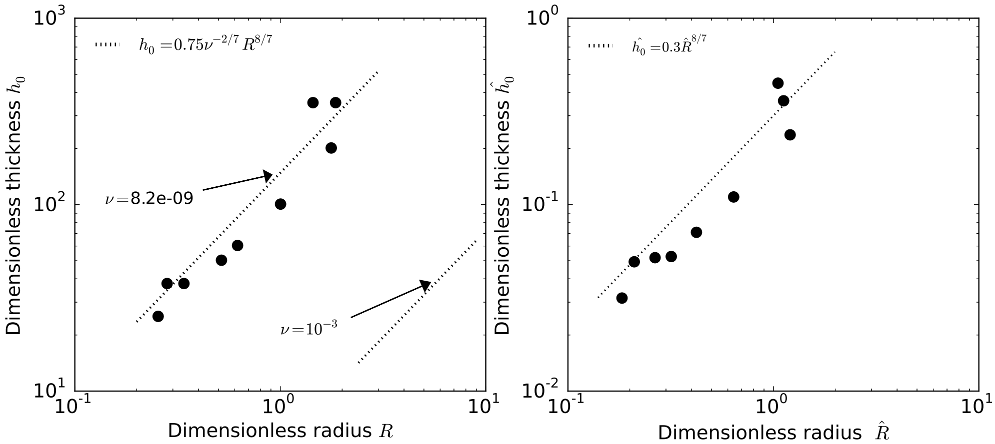

Figure 3.21: Left: Dimensionless maximum thickness h_0 versus radius R for laccoliths from Elba Island, Italy. Thickness, radius and depth for each laccolith are taken from *Rocchi et al.* (2002). Parameters for calculating Λ (3.22) and H (3.23) are $E = 10^9$ GPa, $\nu^* = 0.25$, $\rho_m = 2500$ kg m^{-3}, $g = 9.81$ m s^{-2}, $\eta_h = 10^6$ Pa s and $Q_0 = 0.1$ m^3 s^{-1}. For depth of intrusions between 1.9 and 3.7 km, the length scale Λ is between 2490 m and 3680 m. H is constant and equal to 1.98 m. Dotted lines: scaling laws (3.104) with $h_f = 0.001$ and two values for the viscosity contrast ν indicated on the plot. $\nu = 8.2 \cdot 10^{-9}$ represents the least square best fit for the data. Right: Dimensionless thickness $\hat{h_0}$ versus $\hat{R}$ where $\hat{h_0}$ and $\hat{R}$ are given by (3.105). Substituting (3.24) into (3.32), we obtain $Pe = Q_0H/(\pi\kappa\Lambda^2)$; the parameters for calculating Pe for each laccolith are the same than those used for the nondimensionalization, $\kappa = 10^{-6}$ m s^{-2} and St_m is considered constant and set to 1. The viscosity contrast is set to $\nu = 8.2 \cdot 10^{-9}$ for all laccoliths. Dotted line: scaling law $\hat{h_0} \sim 0.75\hat{R}^{8/7}$.

3.8 Summary and conclusion

Isothermal elastic-plated gravity current shows two asymptotic regimes. At early times, the gravity is negligible and the peeling of the front is driven by the bending of the overlying layer. In contrast, at late times, the own flow weight becomes the driving pressure and the current evolves in a so called gravity current regime. In this study, we have developed a theory for the evolution of an elastic-plated gravity current with a temperature dependent viscosity. In particular, we study the response of the flow to its cooling in each regime separately.

Scaling analyses of the heat transport equation show that the evolution of the thermal structure depends on the regime considered. In the bending regime, since the flow constantly thickens, the thermal anomaly grows with time but slower than the flow itself and a region of cold fluid rapidly forms at the front. The size of the cold fluid region depends on the dimensionless parameters of the system, i.e. the Peclet number, the viscosity contrast and a dimensionless number that accounts for crystallization. In contrast, in the gravity current regime, since the flow tends to a constant thickness, the temperature profile diffuses to an almost stationary profile and the thermal anomaly reaches a steady-state. The time for reaching this steady-state also scales with the dimensionless numbers of the system.

Numerical analyses of the equations show that the combine effect of cooling and temperature-dependent viscosity result in important deviations from the isoviscous case. In particular, each regime is split in three different phases. A first phase where the flow behaves as an isoviscous flow with hot viscosity. A second phase where the flow slows down and drastically thickens. A last phase where the flow returns in an isoviscous flow but with cold viscosity. These three phases are linked to the coupling between the thermal anomaly and the flow itself and in particular, the second phase of the flow is triggered by the detachment of the thermal anomaly. However, we show that the effective viscosity of the flow is drastically different in the two regimes. While the dynamics is governed by the local thermal condition at the front in the bending regime, it is the average thermal structure of the current that controls the flow in the gravity regime.

The final evolution of an elastic-plated gravity current therefore depends on the relative phase change within each regime and the transition between the bending and the gravity regime itself. We provide a general phase diagram that predicts the different evolution scenarios as a function of the dimensionless parameters. We finally apply the results to the spreading of magmatic intrusions and show that, if cooling is indeed an efficient mechanism for the arrest of laccolith in the bending regime, as confirmed by observations, an additional cooling mechanism is needed to explain the exact size of laccoliths.

Appendix A: Numerical scheme

The coupled nonlinear partial differential equations (3.45) and (3.46) are solved on a grid much larger than the flow itself and shifted at the center to avoid problems arising from the axisymmetrical geometry. The procedure used to solve both equations, (3.45) and (3.46), is to use a finite-difference scheme for spatial discretization coupled with an implicit backward Euler scheme in time. In addition, since each equation is non-linear, we use Newton-Raphson method to iterate towards the solution at each time step for both equations. We begin the computation with $h = h_f$, $\Theta_b = 1$ and $\delta = 10^{-4}$ over the whole domain. In addition, we impose

$$\left.\frac{\partial h}{\partial r}\right|_{r=0} = \left.\frac{\partial P}{\partial r}\right|_{r=0} = 0 \tag{3.106}$$

and $h = h_f$ at the end of the grid.

The expressions of $I_0(\delta)$, $I_1(h)$, $I_1(\delta)$ and $I_2(\delta)$ are the following

$$I_0(\delta) = -\frac{\delta}{12}\left(-6\delta\nu + (1-\nu)\left(-5\Theta_b\delta + 4\Theta_b h\right) + 6h\nu\right) \tag{3.107}$$

$$I_1(h) = \frac{1}{60}\left((1-\nu)\left(-4\Theta_b\delta^3 + 10\Theta_b\delta^2 h - 10\Theta_b\delta h^2 + 5\Theta_b h^3\right) + 5h^3\nu\right) \tag{3.108}$$

$$I_1(\delta) = -\frac{\delta^2}{120}\left(-40\delta\nu + (1-\nu)\left(-36\Theta_b\delta + 25\Theta_b h\right) + 30h\nu\right) \tag{3.109}$$

$$I_2(\delta) = -\frac{\Theta_b\delta^2}{2520}\left(-882\delta\nu + (1-\nu)\left(-778\Theta_b\delta + 560\Theta_b h\right) + 735h\nu\right) \tag{3.110}$$

and therefore, (3.47) and (3.48) reduce to

$$\overline{u} = -\frac{\delta}{10}\left(-20\delta\nu + (1-\nu)\left(-14\Theta_b\delta + 15\Theta_b h\right) + 30h\nu\right) \tag{3.111}$$

$$\Sigma = -\frac{\Theta_b\delta^2}{630}\left(-2058\delta\nu + (1-\nu)\left(-1784\Theta_b\delta + 1330\Theta_b h\right) + 1785h\nu\right) \tag{3.112}$$

Appendix B: Phase transitions

A current in the *ith* thermal phase can transition in the jth phase of the gravity regime. In the following, we show that a transition from i to j where $i < j$ is not possible. Indeed, the effective viscosity is that of a small region at the tip in the bending regime whereas it is the average viscosity of the flow in the gravity regime. Therefore, it cannot increase during the transition and

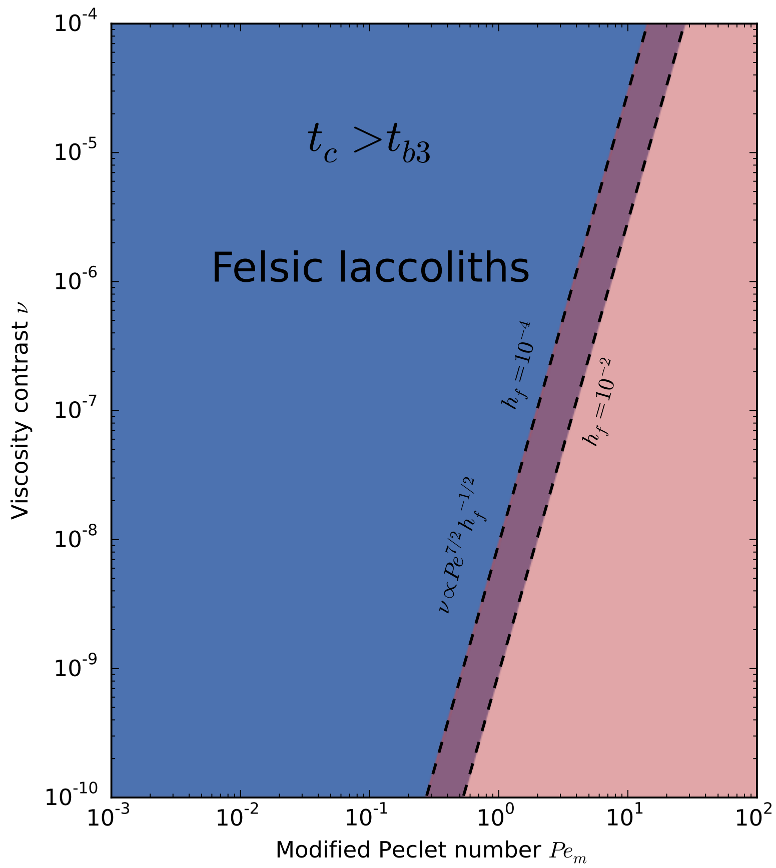

Figure 3.22: Phase transitions reported in Table 3.2

indeed, B_1G_2, B_1G_3 and B_2G_3 are unfeasible (Table 3.2 and Figure 3.22). In addition, the transition from the third thermal phase of the bending regime to the first thermal phase of the gravity regime implies that $t_c < t_{b2}$ and $t_c > t_{g3}$, which is not possible (Table 3.2 and Figure 3.22). Therefore, the five possible sequences that remain are B_1G_1, B_2G_1, B_2G_2, B_3G_2 and B_3G_3 (Table 3.2 and Figure 3.22).

Appendix C: Effect of the pre-wetted film thickness

The divergence of the viscous stresses at the contact line imposes the need for a regularization condition at the front (*Lister et al.*, 2013; *Flitton and King*, 2004; *Hewitt et al.*, 2014). In this study, we show the results of the simulations for a thin pre-wettted film of constant dimensionless thickness $h_f = 5\ 10^{-3}$.

Transition	Condition 1	Condition 2	Condition 3	Output
		Transition in the first bending thermal phase $B1$		
$t_t = t_h$	$t_h < t_{b2}$	$t_h < t_{g2}$	-	B_1G_1
	$Pe_m > 65h_f^{15/7}$	$Pe_m > 650h_f^{-1/7}$	-	Feasible
$t_t = t_h$	$t_h < t_{b2}$	$t_h > t_{g2}$	$t_h < t_{g3}$	B_1G_2
	$Pe_m > 65h_f^{15/7}$	$Pe_m < 650h_f^{-1/7}$	$\nu < 0.6Pe_m^2 h_f^{2/7}$	Unfeasible
$t_t = t_h$	$t_h < t_{b2}$	$t_h > t_{g3}$	-	B_1G_3
	$Pe_m > 65h_f^{15/7}$	$\nu > 0.6Pe_m^2 h_f^{2/7}$	-	Unfeasible
		Transition in the second bending thermal phase $B2$		
$t_h < t_t < t_c$	$t_h > t_{b2}$	$t_c < t_{b3}$	$t_c < t_{g2}$	B_2G_1
	$Pe_m < 65h_f^{-15/7}$	$\nu < \alpha Pe_m^{7/2} h_f^{-1/2}$	$\nu > \beta Pe_m^{-7/2} h_f^{-1/2}$	Feasible
$t_h < t_t < t_c$	$t_h > t_{b2}$	$t_c < t_{b3}$	$t_c < t_{g3}$	B_2G_2 or B_2G_1
	$Pe_m < 65h_f^{-15/7}$	$\nu < \alpha Pe_m^{7/2} h_f^{-1/2}$	$\nu < 0.3Pe_m^{14/3} h_f^{2/3}$	Feasible
$t_h < t_t < t_c$	$t_h > t_{b2}$	$t_c < t_{b3}$	$t_h > t_{g2}$	B_2G_2
	$Pe_m < 65h_f^{-15/7}$	$\nu < \alpha Pe_m^{7/2} h_f^{-1/2}$	$Pe_m < 650h_f^{-1/7}$	Feasible
$t_h < t_t < t_c$	$t_h > t_{b2}$	$t_c < t_{b3}$	$t_h > t_{g3}$	B_2G_3
	$Pe_m < 65h_f^{-15/7}$	$\nu < \alpha Pe_m^{7/2} h_f^{-1/2}$	$\nu > 0.6Pe_m^2 h_f^{2/7}$	Unfeasible
		Transition in the third bending thermal phase $B3$		
$t_t = t_c$	$t_c > t_{b3}$	$t_c < t_{g2}$	-	B_3G_1
	$\nu > \alpha Pe_m^{7/2} h_f^{-1/2}$	$\nu > \beta Pe_m^{-7/2} h_f^{-1/2}$	-	Unfeasible
$t_t = t_c$	$t_c < t_{b2}$	$t_c > t_{g2}$	$t_c < t_{g3}$	B_3G_2
	$\nu > \alpha Pe_m^{7/2} h_f^{-1/2}$	$\nu < \beta Pe_m^{-7/2} h_f^{-1/2}$	$\nu < 0.3Pe_m^{14/3} h_f^{2/3}$	Feasible
$t_t = t_c$	$t_c < t_{b2}$	$t_c > t_{g3}$	-	B_3G_3
	$\nu > \alpha Pe_m^{7/2} h_f^{-1/2}$	$\nu > 0.3Pe_m^{14/3} h_f^{2/3}$	-	Feasible

Table 3.2: Parameter space analysis. The coefficients α and β are $\alpha = 8.3 \cdot 10^{-13}$ and $\beta = 7.0 \cdot 10^{9}$

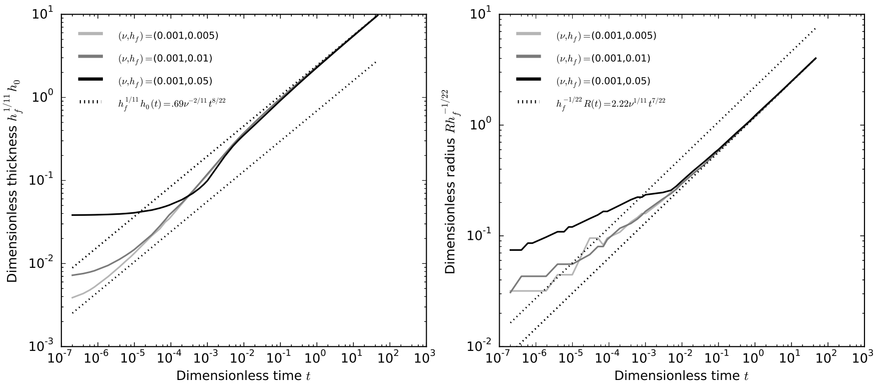

Figure 3.23: Left: Dimensionless thickness at the center $h_0 h_f^{2/22}$ versus dimensionless time t for different sets (ν, h_f) indicated on the plot. Dashed-lines represent the scaling laws $h_0 h_f^{2/22} = 0.7\nu^{-2/11}t^{8/22}$ for $\nu = 1.0$ and 0.001. Right: Dimensionless radius R versus dimensionless time t for the same sets (ν, h_f). Dashed-lines represent the scaling laws $Rh_f^{-1/22} = 2.2\nu^{1/11}t^{7/22}$ for $\nu = 1.0$ and 0.001.

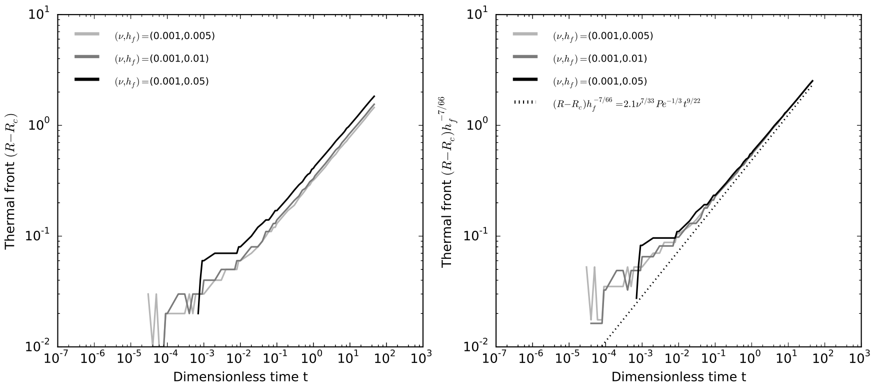

Figure 3.24: Left: Extent of the cold fluid region $R(t) - R_c(t)$ versus dimensionless time for different combinations (ν,h_f) indicated on the plot. Right: Same plot but where we have rescaled the extent of the cold fluid region by $h_f^{7/66}$. Dashed-line: scaling law $(R(t) - R_c(t))h_f^{-7/66} = 2.1Pe^{-1/3}\nu^{7/33}t^{9/22}$.

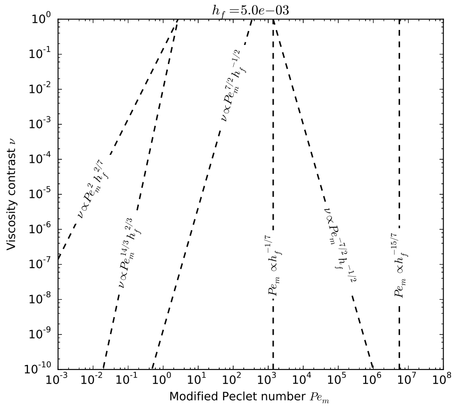

Figure 3.25: Phase diagrams for the evolution with bending and gravity for different combinations (ν,Pe_m) and different values for the film thickness $h_f = 10^{-2}$, 10^{-3} and 10^{-4}.

However, the different scaling laws derived in Section 3.4 depends on the film thickness h_f, as confirmed numerically (Figure 3.23 and 3.24) and in particular, the phase diagram presented in section 3.6 and its application to the spreading of laccolith thus depends on the chosen value for h_f. The meaning of the pre-wetted film thickness in the application to the spreading of laccolith is unclear, however, reasonable values for h_f should range from a few centimeters to no less than 0.1 milimeter $\sim 10^{-4}$. Indeed the height scale has to be linked to some structural length scale at the front of the laccolith. Therefore, as the dependence with h_f is weak, a variation of 2 orders of magnitude does not change significantly the results (Figure 3.25).

The same result hold when we look at the relation between the thickness and the radius of the laccolith (3.104). Indeed, the best fit for the value of the viscosity contrast scales as $h_f^{-1/2}$, i.e. $\nu_{\text{best}} = h_f^{-1/2} 2.59\ 10^{-10}$ and therefore, varying h_f by two orders of magnitudes change the viscosity contrast by one order of magnitude which is acceptable for our application.

Bibliography

Balmforth, N. J., and R. V. Craster (2004), Dynamics of cooling viscoplastic domes, *J. Fluid Mech.* (Not cited.)

Bercovici, D. (1994), A theoretical model of cooling viscous gravity currents with temperature-dependent viscosity, *Geophys. Res. Lett.* (Not cited.)

Bunger, A. P., and A. R. Cruden (2011), Modeling the growth of laccoliths and large mafic sills: Role of magma body forces, *J. Geophys. Res.*, *116*(B2), B02,203. (Not cited.)

Chevrel, M. O., T. Platz, E. Hauber, D. Baratoux, Y. Lavallée, and D. B. Dingwell (2013), Lava flow rheology: A comparison of morphological and petrological methods, *Earth and Planetary Science Letters*, *384*(C), 109–120. (Not cited.)

Das, S. B., I. Joughin, M. D. Behn, I. M. Howat, M. A. King, D. Lizarralde, and M. P. Bhatia (2008), Fracture Propagation to the Base of the Greenland Ice Sheet During Supraglacial Lake Drainage, *Science*, *320*(5877), 778–781. (Not cited.)

Diniega, S., S. E. Smrekar, S. Anderson, and E. R. Stofan (2013), The influence of temperature-dependent viscosity on lava flow dynamics, *J. Geophys. Res. Earth Surf.*, *118*(3), 1516–1532. (Not cited.)

Dixon, J. M., and D. G. Simpson (1987), Centrifuge modelling of laccolith intrusion, *9*(1), 87–103. (Not cited.)

Flitton, J. C., and J. R. King (2004), Moving-boundary and fixed-domain problems for a sixth-order thin-film equation, *European Journal of Applied Mathematics*, *15*(06), 713–754. (Not cited.)

Garel, F., E. Kaminski, S. Tait, and A. Limare (2012), An experimental study of the surface thermal signature of hot subaerial isoviscous gravity currents: Implications for thermal monitoring of lava flows and domes, *J. Geophys. Res.*, *117*(B2), B02,205. (Not cited.)

Garel, F., E. Kaminski, S. Tait, and A. Limare (2014), An analogue study of the influence of solidification on the advance and surface thermal signature of lava flows, *Earth and Planetary Science Letters*, *396*(C), 46–55. (Not cited.)

Giordano, D., J. K. Russell, and D. B. Dingwell (2008), Viscosity of magmatic liquids: A model, *Earth and Planetary Science Letters*, *271*(1-4), 123–134. (Not cited.)

Goodman, T. R. (1958), *The heat-balance integral and its application to problems involving a change of phase*, Trans. ASME. (Not cited.)

Hewitt, I. J., N. J. Balmforth, and J. R. De Bruyn (2014), Elastic-plated gravity currents, pp. 1–29. (Not cited.)

Hort, M. (1997), Cooling and crystallization in sheet-like magma bodies revisited, *Journal of Volcanology and Geothermal Research*, *76*(3-4), 297–317. (Not cited.)

Hosoi, A., and L. Mahadevan (2004), Peeling, Healing, and Bursting in a Lubricated Elastic Sheet, *Phys. Rev. Lett.*, *93*(13), 137,802. (Not cited.)

Huppert, H. E. (1982a), The propagation of two-dimensional and axisymmetric viscous gravity currents over a rigid horizontal surface, *J. Fluid Mech.*, *121*(-1), 43–58. (Not cited.)

Huppert, H. E. (1982b), Flow and instability of a viscous current down a slope, *Nature*. (Not cited.)

Johnson, A. M., and D. D. Pollard (1973), Mechanics of growth of some laccolithic intrusions in the Henry mountains, Utah, I: field observations, Gilbert's model, physical properties and flow of the magma, *Tectonophysics*. (Not cited.)

Lejeune, A. M., and P. Richet (1995), Rheology of crystal-bearing silicate melts: An experimental study at high viscosities, *Journal of Geophysical Research: Planets (1991–2012)*, *100*(B3), 4215–4229. (Not cited.)

Lister, J. R., G. G. Peng, and J. A. Neufeld (2013), Viscous Control of Peeling an Elastic Sheet by Bending and Pulling, *Phys. Rev. Lett.*, *111*(15), 154,501. (Not cited.)

Marsh, B. D. (1981), On the crystallinity, probability of occurrence, and rheology of lava and magma, *Contr. Mineral. and Petrol.*, *78*(1), 85–98. (Not cited.)

Martí, J. (2000), Pressure evolution during explosive caldera-forming eruptions, *Earth and Planetary Science Letters*, *175*(3-4), 275–287. (Not cited.)

Michaut, C. (2011), Dynamics of magmatic intrusions in the upper crust: Theory and applications to laccoliths on Earth and the Moon, *J. Geophys. Res.*, *116*(B5), B05,205. (Not cited.)

Michaut, C., and D. Bercovici (2009), A model for the spreading and compaction of two-phase viscous gravity currents, *J. Fluid Mech.*, *630*, 299–329. (Not cited.)

Michaut, C., and C. Jaupart (2006), Ultra-rapid formation of large volumes of evolved magma, *Earth and Planetary Science Letters*, *250*(1-2), 38–52. (Not cited.)

Patankar, S. (1980), Numerical heat transfer and fluid flow. (Not cited.)

Pinkerton, H., and R. J. Stevenson (1992), Methods of determining the rheological properties of magmas at sub-liquidus temperatures, *Journal of Volcanology and Geothermal Research*, *53*(1-4), 47–66. (Not cited.)

Pollard, D. D., and A. M. Johnson (1973), Mechanics of growth of some laccolithic intrusions in the Henry Mountains, Utah, II: bending and failure of overburden layers and sill formation, *Tectonophysics*, *18*(3-4), 311–354. (Not cited.)

Rocchi, S., D. S. Westerman, A. Dini, F. Innocenti, and S. Tonarini (2002), Two-stage growth of laccoliths at Elba Island, Italy, *Geology*, *30*(11), 983–986. (Not cited.)

Shaw, H. R. (1972), Viscosities of magmatic silicate liquids; an empirical method of prediction, *Am J Sci*, *272*(9), 870–893. (Not cited.)

Tait, S., C. Jaupart, and S. Vergniolle (1988), Pressure, gas content and eruption periodicity of a shallow, crystallising magma chamber, *Earth and Planetary Science Letters*, *92*, 107–123. (Not cited.)

Thorey, C., and C. Michaut (2014), A model for the dynamics of crater-centered intrusion: Application to lunar floor-fractured craters, *J. Geophys. Res. Planets*, *119*(1), 286–312. (Not cited.)

Tsai, V. C., and J. R. Rice (2010), A model for turbulent hydraulic fracture and application to crack propagation at glacier beds, *J. Geophys. Res.*, *115*(F3), F03,007. (Not cited.)

Whittington, A. G., B. M. Hellwig, H. Behrens, B. Joachim, A. Stechern, and F. Vetere (2009), The viscosity of hydrous dacitic liquids: implications for the rheology of evolving silicic magmas, *Bull Volcanol*, *71*(2), 185–199. (Not cited.)

CHAPTER 4

Toward a more realistic model- Relaxing the thermal boundary condition and changing the rheology

Contents

The previous Chapter was first step toward the understanding how the cooling of the laccolith interacts with its dynamics. Hereafter, we investigate the changes triggered by both the heating of the surrounding layer and a more realistic rheology.

4.1 Introduction

Contact metamorphism around sill intrusion is a common process (*Everett and Hoisch*, 2008)

4.2 Theory

We consider the model of elastic-plated gravity current with temperature-dependent viscosity described in Section 3.2 where we relax the isothermal boundary condition. In the following, we specify only the change in the theory that comes with the new thermal boundary condition and refer the reader to Section 3.2 for more details about the derivation.

4.2.1 Thermal boundary condition

We now consider the heating of the surrounding medium by the magma itself at the contact with the surrounding rock, the continuity of the temperature imposes to rewrite the vertical temperature profile as

$$T = \begin{cases} T_b - (T_b - T_s)(1 - \frac{z}{\delta})^2 & 0 \le z \le \delta \\ T_b & \delta \le z \le h - \delta \\ T_b - (T_b - T_s)(1 - \frac{h-z}{\delta})^2 & h - \delta \le z \le h \end{cases} \tag{4.1}$$

where $\delta(r,t)$ is the thermal boundary layer thickness, $T(r,z,t)$ is temperature of the fluid, $T_b(r,t)$ is the temperature at the center of the profile and $T_s(r,t)$ is the temperature of the surface, i.e. $T(r, z = 0, t) = T(r, z = h, t) = T_s(r,t)$. As in Section 3.2, this profile assures the continuity of the temperature and heat flux within the flow. In addition, continuity of the heat flux across the boundaries reads

$$k_m \left.\frac{\partial T}{\partial z}\right|_{z=0} = k_r \left.\frac{\partial T_r}{\partial z}\right|_{z=0} \tag{4.2}$$

$$k_m \left.\frac{\partial T}{\partial z}\right|_{z=h} = k_r \left.\frac{\partial T_r}{\partial z}\right|_{z=h} \tag{4.3}$$

where $T_r(r,z)$ is the temperature in the surrounding medium and k_r its thermal conductivity. Assuming a semi infinite layer for the rigid layer below the intrusion, *Carslaw and Jaeger* (1959) show that the temperature T_r in the surrounding rocks can be approximated to a first order by

$$T_r(r,z,t) - T_0 = (T_s - T_0)\,\mathrm{erfc}\left(\frac{-z}{2\sqrt{\kappa_r t}}\right). \tag{4.4}$$

The thickness of the upper layer is equal to the intrusion depth d_c. However, we assume that the depth d_c is large compared to the characteristic length scale for conduction L_c and we use the same approximation to derive T_r above the intrusion

$$T_r(r,z,t) - T_0 = (T_s - T_0)\,\mathrm{erfc}\left(\frac{z-h}{2\sqrt{\kappa_r t}}\right). \tag{4.5}$$

Therefore, the two thermal boundary conditions (4.2) and (4.3) become

$$k_m \left.\frac{\partial T}{\partial z}\right|_{z=0} = k_r \frac{T_s - T_0}{\sqrt{\pi \kappa_r t}} \tag{4.6}$$

$$k_m \left.\frac{\partial T}{\partial z}\right|_{z=h} = -k_r \frac{T_s - T_0}{\sqrt{\pi \kappa_r t}}. \tag{4.7}$$

4.2.2 Dimensionless equations

Except for the conduction term, which now account for the dimensionless surface temperature Θ_s, the coupled equations governing the cooling the current are very similar to (3.45) and (3.46) and reads

$$\frac{\partial h}{\partial t} - \frac{12}{r}\frac{\partial}{\partial r}\left(r I_1(h) \frac{\partial P}{\partial r}\right) = \mathcal{H}(\frac{\gamma}{2} - r)\frac{32}{\gamma^2}\left(\frac{1}{4} - \frac{r^2}{\gamma^2}\right) \tag{4.8}$$

$$\frac{\partial \xi}{\partial t} + \frac{1}{r}\frac{\partial}{\partial r}\left(r\left(\bar{u}\xi - \Sigma\right)\right) = 2Pe^{-1}St_m \frac{\Theta_b - \Theta_s}{\delta} \tag{4.9}$$

with

$$\overline{\theta} = \frac{1}{3}\left(2\Theta_b + \Theta_s\right) \tag{4.10}$$

$$\overline{u} = \frac{12}{\delta}\frac{\partial P}{\partial r}\left(\delta I_0(\delta) - I_1(\delta)\right) \tag{4.11}$$

$$\Sigma = \frac{12}{\delta}\frac{\partial P}{\partial r}\left(I_0(\delta)\left(G(\delta) - \delta\overline{\theta}\right) + \overline{\theta} I_1(\delta) - I_2(\delta)\right). \tag{4.12}$$

where $G(z)$ denotes a primitive of $\theta(z)$ when $z < \delta$. The coupling between equations (4.8) and (4.9), i.e. the rheology is contained in the three integrals $I_0(z)$, $I_1(z)$ and $I_2(z)$ and is discussed in the next section. The thermal boundary conditions (4.6) and (4.7) reduce in a dimensionless form to

$$2\frac{\Theta_b - \Theta_s}{\delta} = \Omega Pe^{1/2}\frac{\Theta_s}{\sqrt{\pi t}}. \tag{4.13}$$

where Ω is a new dimensionless number; it is equal to

$$\Omega = \frac{k_r}{k_m}\left(\frac{\kappa_m}{\kappa_r}\right)^{1/2} \tag{4.14}$$

and represents the ratio between heat conduction at the contact with the encasing rocks and heat diffusion within the fluid.

Finally, using this thermal boundary condition (4.13), we can show that the different variables can be expressed in term of ξ such that (Appendix 4.4)

$$\Theta_s(r,t) = \begin{cases} \frac{3\beta}{4}\xi - \frac{\sqrt{3}}{4}\sqrt{\beta\xi\left(3\beta\xi + 8\right)} + 1 & \text{if} \quad \xi \leq \xi_t \\ \frac{-12\xi + 6h(r,t)}{(\beta h(r,t) + 6)h(r,t)} & \text{if} \quad \xi > \xi_t \end{cases} \tag{4.15}$$

and

$$\Theta_b(r) = \begin{cases} 1 & \text{if} \quad \xi \leq \xi_t \\ \frac{\Theta_s}{4}\left(\beta(t)h(r,t)+4\right) & \text{if} \quad \xi > \xi_t \end{cases} \tag{4.16}$$

$$\delta(r) = \begin{cases} \frac{1}{\Theta_s \beta(t)}\left(-2\Theta_s+2\right) & \text{if} \quad \xi \leq \xi_t \\ h(r,t)/2 & \text{if} \quad \xi > \xi_t \end{cases} \tag{4.17}$$

with

$$\xi_t(t) = \frac{\beta(t)h^2(r,t)}{6\beta(t)h(r,t)+24} \tag{4.18}$$

$$\beta(t) = \Omega Pe^{1/2}\frac{1}{\sqrt{\pi t}} \tag{4.19}$$

4.2.3 Rheology

The model derived in Section 4.2.2 does not assume a specific relation between viscosity and temperature and the choice of the rheology $\eta(T)$, which appears in the integrals $I_0(z)$, $I_1(z)$ and $I_2(z)$ remains to be defined. In Section 3.2, we assume a viscosity inversely dependent on the temperature which reads in a dimension form

$$\eta(T) = \frac{\eta_h \eta_c (T_i - T_0)}{\eta_h (T_i - T_0) + (\eta_c - \eta_h)(T - T_0)}. \tag{4.20}$$

where η_h and η_c are the viscosities of the hottest and coldest fluid at the temperature T_i and T_0 respectively (*Bercovici*, 1994). While this model possesses some nice simplification properties, it restricts the change in viscosity to a very narrow range of temperature close to $T = T_0$, i.e. $\theta = 0$ (Figure 4.1). In contrast, the Arrhenius model ($\eta \sim \exp(-k/T)$), which is a more realistic model to relate temperature and viscosity of lavas (*Blatt et al.*, 2006), describes a viscosity that increases over a much larger range of temperature (Figure 4.1). To get some insights into the effect of a more realistic temperature-dependent viscosity, we thus also use a first-order approximation of the Arrhenius model as a second rheology $\eta_2(T)$ (*Diniega et al.*, 2013)

$$\eta_2(T) = \eta_h \exp\left(-\log\left(\frac{\eta_h}{\eta_c}\right)\left(1 - \frac{T - T_0}{T_i - T_0}\right)\right) \tag{4.21}$$

In a dimensionless form, they read

$$\eta_1(\theta)/\eta_h = \frac{1}{\nu + (1-\nu)\theta} \tag{4.22}$$

$$\eta_2(\theta)/\eta_h = \exp\left(-\log(\nu)\left(1-\theta\right)\right) \tag{4.23}$$

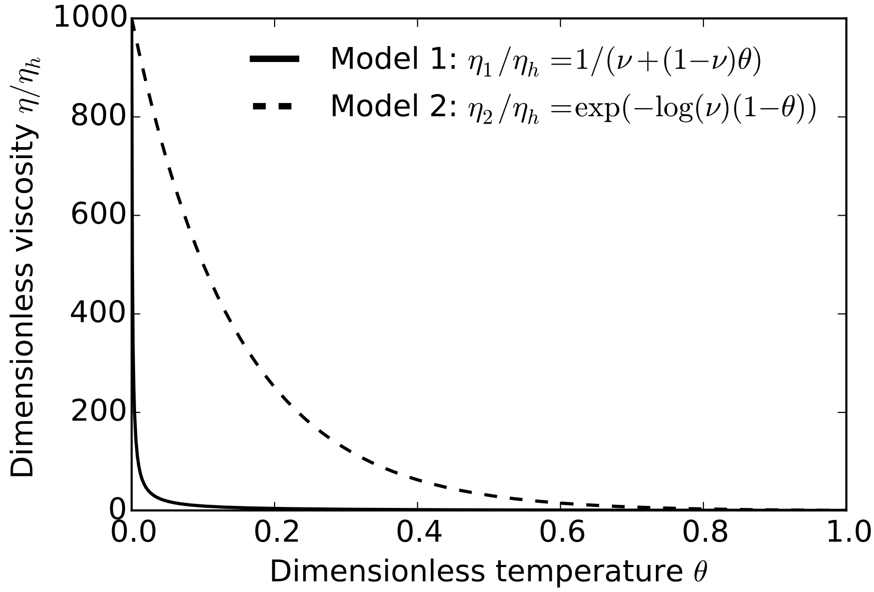

Figure 4.1: Dimensionless viscosity versus dimensionless temperature for both rheology η_1 (4.22) and η_2 (4.23).

where ν is the viscosity contrast described in Section 3.2 and represents the ratio between the hot viscosity η_h and the cold viscosity η_c. The expression of $I_0(\delta)$, $I_1(\delta)$, $I_1(h)$ and $I_2(\delta)$, necessary to close the model, are given in Appendix 4.4 for both rheologies.

4.2.4 Comparison with the isothermal model

We showed that relaxing the isothermal boundary condition introduces a new dimensionless number Ω which controls how much heat can be transferred to the surrounding rocks. In the limit $\Omega \to \infty$, the model should thus reduce to the model described in Section 3.2. Indeed, when $\Omega \to \infty$, the coefficient $\beta \to \infty$ and then $\xi_t \to h/6$ (Section 3.2). When $\xi < \xi_t$, injecting the corresponding expression of Θ_s (4.15) in the corresponding expression of δ (4.17) gives

$$\delta = \frac{3\beta\xi + \sqrt{3}\sqrt{\beta\xi(3\beta\xi + 8)} + 8}{2\beta} \tag{4.24}$$

which tends to 3ξ when $\beta \to \infty$. When $\xi > \xi_t$, injecting the corresponding expression of Θ_s (4.15) in the corresponding expression of Θ_b (4.16) gives

$$\Theta_b = \frac{3(\beta h + 4)(h - 2\xi)}{2h(\beta h + 6)} \tag{4.25}$$

which tends to $3/2 - 3\xi/h$ when $\beta \to \infty$ (Section 3.2). Finally, taking the limit of Θ_s for both $\xi > \xi_t$ and $\xi < \xi_t$ show that Θ_s indeed tends to zero when $\Omega \to \infty$.

For magmatic intrusion, the thermal parameters of the magma and the encasing rocks are close and the dimensionless number Ω is close to 1. In the following, we study the effect of relaxing the isothermal boundary condition on the dynamics by comparing $\Omega = 10^5$ and $\Omega = 1$ in both regimes separately. We also investigate the effect of a more realistic rheology on the flow dynamics.

4.3 Evolution in the bending regime

We follow the same approach as in the previous Chapter and first concentrate on the case in which only bending contributes to the pressure. The governing equations are thus (4.8) and (4.9) where $P = \nabla_r^4 h$. In the previous Chapter, we show that the dynamics in the bending regime depends on the average viscosity of a small region at the front of the current and can be divided in three phases. A first phase where the current behaves as an isoviscous flow with hot viscosity. A second phase where the flow slows down and thickens. A last phase where the flow returns in an isoviscous flow but with cold viscosity. Hereafter, we first describe how the thermal boundary condition influences the timing for the phase transition by looking at two values for the dimensionless number Ω, i.e. $\Omega = 1$ and $\Omega = 10^5$ using the inverse temperature dependence for the rheology $\eta_1(\theta)$, as in Chapter 3. We thus investigate the effect of changing the rheology.

4.3.1 Relaxing the thermal boundary condition, effect of Ω

As for the isothermal boundary condition, the thermal boundary layers first connect at the front and a region of cold fluid forms at the current tip for $\Omega = 1$ (Figure 4.2). However, in that case, the heating of the surrounding medium limits heat loss in the central region of the current and the thermal anomaly extends further into the flow. For instance, for $\nu = 0.001$ and $Pe = 1.0$, while the thermal anomaly extends over 50% of the current for $\Omega = 10^5$ at $t = 10$, it extends over 75% of the flow for $\Omega = 1$ (Figure 4.2).

As for $\Omega = 10^5$, the current first behave has an isoviscous flow with hot viscosity, it then slows down and thickens to finally behave again as an isoviscous flow but with cold viscosity (Figure 4.3). As the current tip remains hot for a longueur period of time, the transition to the second and third bending regime are however delayed relative to the case $\Omega = 10^5$ (Figure 4.3). For

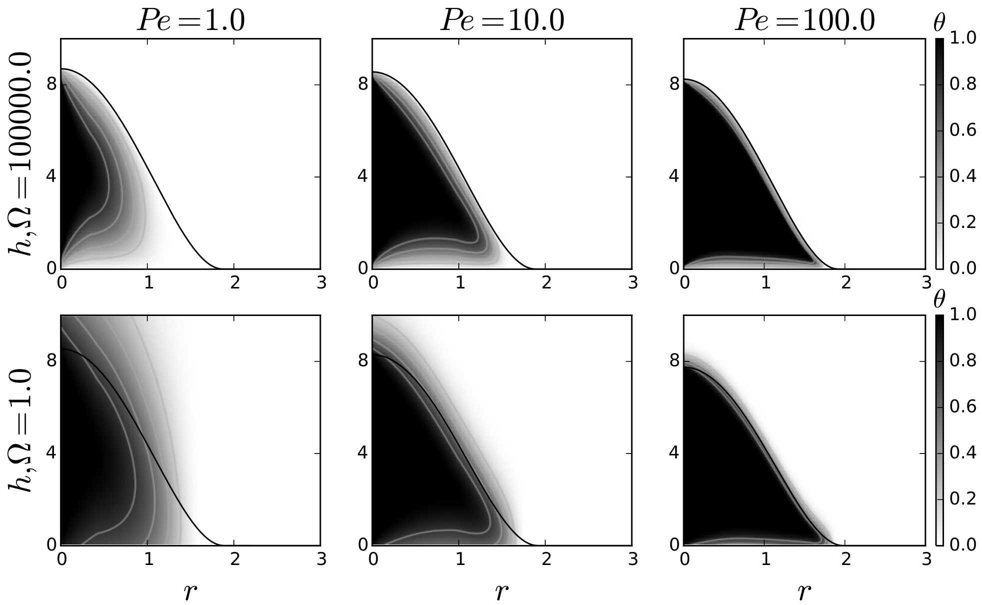

Figure 4.2: Snapshots of the flow thermal structure $\theta(r, z, t)$ for different sets (Pe,Ω) with $Pe = 1.0$,10.0 ,100.0 and $\Omega = 10^5$ and 1.0 at $t = 10$ for $\nu = 0.001$. The thermal structure in the surrounding medium is given by (4.5) and reads in a dimensionless form $\Theta_r(r, z, t) = \Theta_s(r, t)\,\mathrm{erfc}\left(Pe^{1/2}\frac{\kappa_m}{\kappa_r}\frac{(z-h)}{2\sqrt{t}}\right)$ where the ratio κ_m/κ_r is set to 1.

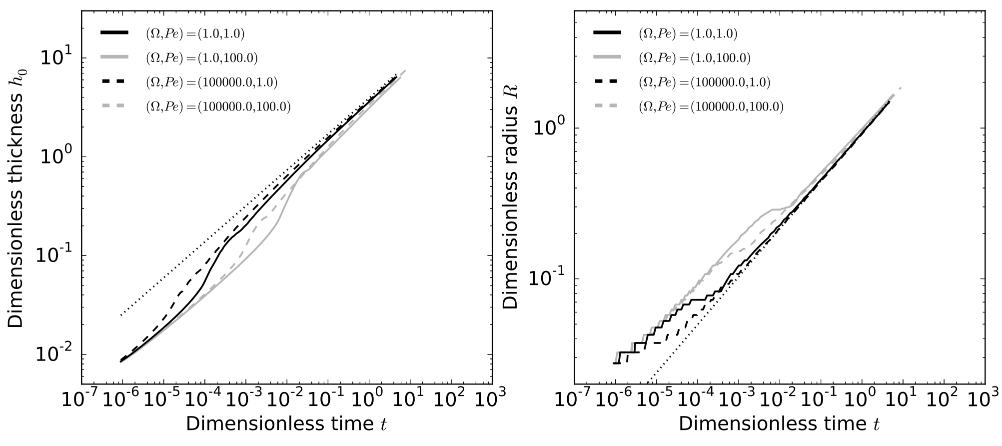

Figure 4.3: Left: Dimensionless thickness at the center h_0 versus dimensionless time t for different sets (ν, Pe) indicated on the plot. Dotted-lines: scaling laws $h_0 = 0.7h_f^{-1/11}\nu^{-2/11}t^{8/22}$ for $\nu = 1.0$ and 0.001. Right: Dimensionless radius R versus dimensionless time t for the same sets (ν, Pe). Dotted-lines: the scaling laws $R = 2.2h_f^{1/22}\nu^{1/11}t^{7/22}$ for $\nu = 1.0$ and 0.001.

instance, for $\nu = 10^{-3}$ and $Pe = 1.0$, while the transitions to the second bending phase occurs at $t \sim 10^{-5}$ for $\Omega = 10^5$, it occurs only after $t \sim 10^{-4}$ for $\Omega = 1.0$ (Figure 4.3).

In addition, the second phase of thickening show two different stages: a first stage where the thickness drastically increases and a second stage where it continues increasing but much slower (Figure 4.3). This transition, enhanced by the smaller spatial resolutions of the simulations in this chapter, reflects the detachment of the thermal anomaly and is discussed in Appendix 4.4.

4.3.2 Characterization of the thermal anomaly

As in Chapter 3, we quantify the size of the thermal anomaly through a critical thermal radius $R_c(t)$ where the temperature at the center of the flow Θ_b is 1% of the injection temperature, i.e. $\Theta_b(r = 0) - \Theta_b(r = R_c) = 0.99$. As expected, the thermal anomaly is larger when considering the heating of the surrounding medium relative to the isothermal boundary condition at a same time (Figure **??**).

The size of the thermal anomaly $R_c(t)$ is given by the radius where advection of heat is equal to heat loss (3.84)

$$\frac{d}{dt}\left(\theta(r = R_c, t)\right) \propto Pe^{-1} \frac{\partial^2}{\partial z^2}\left(\theta(r = R_c, t)\right). \tag{4.26}$$

which, by integration over the thickness of the flow h becomes (3.21)

$$\begin{aligned}
\frac{d}{dt}\left(\int_0^h \theta dz\right) - \Theta_s \frac{dh}{dt} &\propto Pe^{-1} \frac{\Theta_b - \Theta_s}{h} \\
\overline{\theta}\frac{dh}{dt} + h\frac{d\overline{\theta}}{dt} - \Theta_s \frac{dh}{dt} &\propto Pe^{-1} \frac{\Theta_b - \Theta_s}{h} \\
\frac{2}{3}\left(\Theta_b - \Theta_s\right)\frac{dh}{dt} &\propto Pe^{-1} \frac{\Theta_b - \Theta_s}{h} \\
\frac{dh}{dt} &\propto \frac{Pe^{-1}}{h}
\end{aligned} \tag{4.27}$$

where $\overline{\theta}$ is equal to $(\int_0^h \theta dz)/h$ here and we have assumed that $\overline{\theta}$ is constant at $r = R_c$. Therefore, relaxing the thermal boundary condition does not modify (3.85) and the larger size of the thermal anomaly when $\Omega = 1$ must be linked to the heat advection rate, i.e. the left hand side term in the balance (4.27).

Using the thickness profile (3.49), the left hand side term of (4.27) becomes

$$\frac{dh}{dt} = \alpha^2 \left(1 + \frac{R_c}{R}\right)^2 \frac{\partial h_0}{\partial t} + \frac{4 h_0 R_c^2}{R^3}\frac{\partial R}{\partial t}\alpha\left(1 + \frac{R_c}{R}\right) \tag{4.28}$$

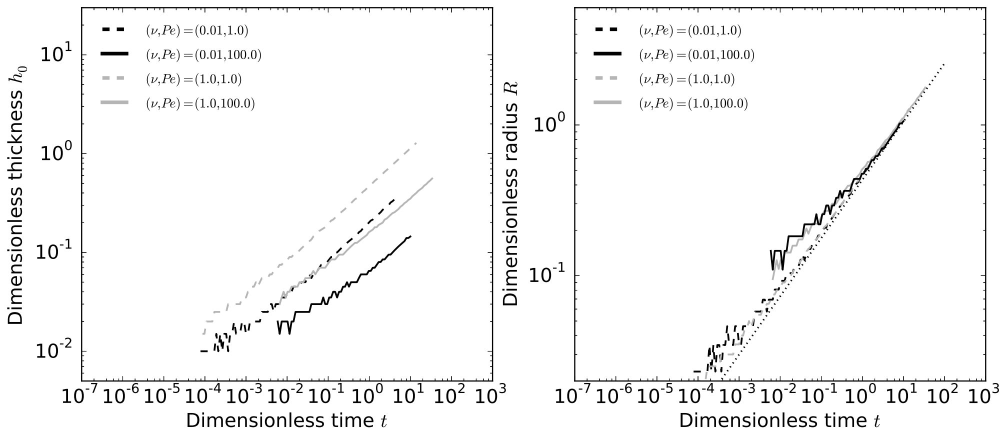

Figure 4.4: Left: Extent of the cold fluid region $R(t) - R_c(t)$ versus dimensionless time for different combinations (ν,Pe) indicated on the plot, the first order Arrhenius rheology $\eta_2(\theta)$ and $\Omega = 1$. Right: Same plot but where we rescale the extent of the cold fluid region by $Pe^{-1/4}\nu^{2/11}$. Dotted-line: scaling law $(R(t) - R_c(t))Pe^{1/4}\nu^{-2/11} = 0.9h_f^{1/11}t^{17/44}$.

where $\alpha(t)$ is the normalized region beyond $r = R_c(t)$, i.e. $\alpha(t) = (R(t) - R_c(t))/R(t)$. While the second term of the right hand side is dominant in the isothermal boundary case, it becomes weaker than the first term when $\Omega = 1$. Indeed, when $\Omega = 1$, the heating of the surrounding medium. Therefore, the balance (4.27) reduces to

$$\alpha^2\left(1+\frac{R_c}{R}\right)^2\frac{\partial h_0}{\partial t} \propto \frac{Pe^{-1}}{\alpha^2\left(1+\frac{R_c}{R}\right)^2 h_0} \tag{4.29}$$

which, in the limit $\alpha << 1$, becomes

$$\alpha^4\frac{\partial h_0}{\partial t} \propto \frac{Pe^{-1}}{h_0\frac{\partial h_0}{\partial t}}. \tag{4.30}$$

Substituting the thickness at the center $h_0(t)$ by its respective scaling law (3.82), the relative size of the normalized cold front region α reads

$$\alpha(t) \propto h_f^{1/22}\nu^{1/11}Pe^{-1/4}t^{7/44} \tag{4.31}$$

which is equivalent to

$$R(t) - R_c(t) = 0.8h_f^{1/11}\nu^{2/11}Pe^{-1/4}t^{17/44} \tag{4.32}$$

where the numerical prefactor, which depends on the definition of the thermal anomaly, has been chosen to fit the simulations.

The predicted scaling law for the evolution of the extent of the cold fluid region (4.32) indeed closely fits the numerical simulations, even for the isoviscous case $\nu = 1$ with $Pe = 1$. The cold fluid region thus cools slightly slower than for isothermal boundary condition, from $t^{9/22}$ to $t^{17/44}$. In addition, the dependence is weaker in the Peclet number, from a power 1/3 to 1/4 when relaxing the isothermal boundary condition. Indeed, for small Pe, the vertical diffusion is efficient on the emplacement time scale, the heat loss in the interior are smaller and the thermal anomaly larger. In contrast, for large values of Pe, the advection dominates and the saving of heat due to the heating of the medium is less important decreasing the overall difference between small and large values of Pe. In the following, we consider the more realistic first order Arrhenius rheology $\eta_2(\theta)$ and we define the final value for the phase transitions within the bending regime.

4.3.3 Influence of the rheology, effect of $\eta(\theta)$

The first order Arrhenius rheology $\eta_2(\theta)$ widens the range of temperature over which significant viscosity variation occurs (Figure 4.1), i.e. $\sim 80\%$ of the temperature range against $\sim 10\%$ for $\eta_1(\theta)$. Therefore, the effective flow viscosity starts to increase sooner and the phase transitions within the bending regime occur sooner than for the rheology previously considered $\eta_1(\theta)$ (Figure 4.5). For instance, for $\nu = 10^{-3}$ and $Pe = 1.0$, while the second phase of the flow starts around $t \sim 10^{-4}$ for the rheology $\eta_1(\theta)$, it starts around $t \sim 10^{-5}$ for the rheology $\eta_2(\theta)$ (Figure 4.5).

4.3.4 Size of the thermal aureole

The size of the thermal aureole, the heated region surrounding the current, scales as $(\kappa_r \tau)^{1/2}$, i.e. $Pe^{-1/2}$ and hence is much larger for small values of Pe. Indeed, for large values of Pe, advection dominates on the emplacement time scale and the thermal aureole is restricted to a small zone around the current (Figure 4.2). For instance, the thickness of the thermal aureole at the center for $Pe = 1.0$ is almost equal to the current thickness h_0 whereas it is only a few percent of h_0 for $Pe = 100.0$ (Figure 4.2).

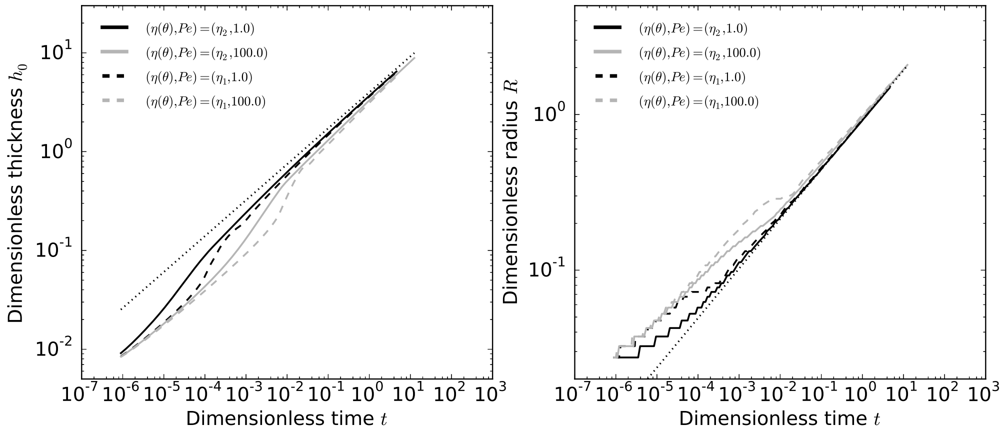

Figure 4.5: Left: Dimensionless thickness at the center h_0 versus dimensionless time t for different sets (ν, Pe) indicated on the plot. Dotted-lines: scaling laws $h_0 = 0.7h_f^{-1/11}\nu^{-2/11}t^{8/22}$ for $\nu = 0.001$. Right: Dimensionless radius R versus dimensionless time t for the same sets (ν, Pe). Dotted-lines: the scaling laws $R = 2.2h_f^{1/22}\nu^{1/11}t^{7/22}$ for $\nu = 0.001$.

4.4 Evolution in the gravity regime

Appendix A: Main variables

The variable ξ is the sufficient variable to solve for in the heat transport equation (3.38). Indeed,

$$\xi = \frac{\delta}{3}\left(-2\Theta_b - \Theta_s + 3\right) \tag{4.33}$$

where we have used (4.10). In addition, from (4.13), we can rewrite

$$\Theta_s = \frac{2\Theta_b}{\beta\delta + 2}, \tag{4.34}$$

$$\delta = \frac{1}{\Theta_s\beta}\left(2\Theta_b - 2\Theta_s\right), \tag{4.35}$$

$$\Theta_b = \frac{\Theta_s}{2}\left(\beta\delta + 2\right) \tag{4.36}$$

When the thermal boundary layer just merged, then $\Theta_b = 1$, $\delta = h/2$ and injecting (4.34) into (4.33) gives

$$\xi_t(t) = \frac{\beta(t)h^2(r,t)}{6\beta(t)h(r,t) + 24} \tag{4.37}$$

Therefore, when $\xi < \xi_t$, the thermal boundary layer are not merged, $\Theta_b = 1$ and injecting (4.35) into (4.33) and solving for Θ_s gives

$$\Theta_s = \frac{3\beta}{4}\xi - \frac{\sqrt{3}}{4}\sqrt{\beta\xi\left(3\beta\xi+8\right)} + 1. \tag{4.38}$$

In contrast, when $\xi > \xi_t$, the thermal boundary layer are merged, $\delta = h/2$ and injecting (4.36) into (4.33) and solving for Θ_s gives

$$\Theta_s = \frac{-12\xi + 6h}{\left(\beta h + 6\right)h}. \tag{4.39}$$

Appendix B: Integral expressions

The model developed in Section 4.2 depends on the integrals

$$\begin{aligned}
I_0(z) &= \int_0^z \frac{1}{\eta(y)}\left(y - \frac{h}{2}\right)dy & (4.40)\\
I_1(z) &= \int_0^z \frac{1}{\eta(y)}\left(y - \frac{h}{2}\right)ydy & (4.41)\\
I_2(z) &= \int_0^y \frac{1}{\eta(y)}\left(y - \frac{h}{2}\right)G(y)dy & (4.42)
\end{aligned}$$

where $G(z)$ is a primitive of $\theta(z)$ where $z < \delta$ and is given by

$$G(z) = \frac{z\left(3\delta^2\Theta_s + 3\delta z(\Theta_b - \Theta_s) + z^2(\Theta_s - \Theta_b)\right)}{3\delta^2}. \tag{4.43}$$

In particular, the model requires the expression of $I_0(\delta)$, $I_1(\delta)$, $I_1(h)$ and $I_2(\delta)$.

Rheology 1: $\eta(\theta) = \eta_1(\theta)$

In that case, the four integrals can be easily derived and read

$$\begin{aligned}
I_0(\delta) &= \frac{\delta}{12}\left(6\delta\nu + (1-\nu)\left(-\alpha_1\delta + 2\alpha_1 h + 6\Theta_b\delta - 6\Theta_b h\right) - 6h\nu\right)\\
I_1(\delta) &= \frac{\delta^2}{120}\left(40\delta\nu + (1-\nu)\left(-4\alpha_1\delta + 5\alpha_1 h + 40\Theta_b\delta - 30\Theta_b h\right) - 30h\nu\right)\\
I_1(h) &= \frac{1}{60}\left((1-\nu)\left(-4\alpha_1\delta^3 + 10\alpha_1\delta^2 h - 10\alpha_1\delta h^2 + 5\Theta_b h^3\right) + 5h^3\nu\right)\\
I_2(\delta) &= -\frac{\delta^2}{2520}\left(378\alpha_1\delta\nu - 315\alpha_1 h\nu - 840\Theta_b\delta\nu + 630\Theta_b h\nu\right)\\
&\quad -\frac{\delta^2}{2520}(1-\nu)\left(-50\alpha_1^2\delta + 70\alpha_1^2 h + 462\alpha_1\Theta_b\delta - 420\alpha_1\Theta_b h - 840\Theta_b^2\delta + 630\Theta_b^2 h\right)
\end{aligned}$$

where $\alpha = \Theta_b - \Theta_s$ has been introduced for clarity.

Rheology 2: $\eta(\theta) = \eta_2(\theta)$

For cases where $\nu < 1$, we have

$$
\begin{aligned}
I_0(\delta) &= -\frac{\delta \nu^{1-\Theta_b}\left(\sqrt{\pi}\sqrt{\alpha_1}(2\delta - h)\sqrt{-\alpha_2}\mathrm{erf}\left(\sqrt{\alpha_1}\sqrt{-\alpha_2}\right) + 2\delta\left(\nu^{\alpha_1} - 1\right)\right)}{4\alpha_1\alpha_2} \\
I_1(\delta) &= \frac{\delta^2\nu^{1-\Theta_b}\left(\sqrt{\pi}\,\mathrm{erf}\left(\sqrt{\alpha_1}\sqrt{-\alpha_2}\right)\left(\alpha_1(h-2\delta)\alpha_2 + \delta\right)\right)}{4\alpha_1^{3/2}(-\alpha_2)^{3/2}} \\
&+ \frac{\delta^2\nu^{1-\Theta_b}\left(\sqrt{\alpha_1}\sqrt{-\alpha_2}\left(2\delta\left(\nu^{\alpha_1} - 2\right) - h\nu^{\alpha_1} + h\right)\right)}{4\alpha_1^{3/2}(-\alpha_2)^{3/2}} \\
I_1(h) &= \frac{\nu^{1-\Theta_b}\left(\sqrt{\alpha_1}\sqrt{-\alpha_2}\left(12\delta^2\left(\delta\left(\nu^{\alpha_1} - 2\right) - h\nu^{\alpha_1} + h\right) + \alpha_1(2\delta - h)^3\log(\nu)\right)\right)}{12\alpha_1^{3/2}(-\alpha_2)^{3/2}} \\
&- \frac{\nu^{1-\Theta_b}\left(3\sqrt{\pi}\delta\mathrm{erf}\left(\sqrt{\alpha_1}\sqrt{-\alpha_2}\right)\left(\alpha_1(h-2\delta)^2\alpha_2 - 2\delta^2\right)\right)}{12\alpha_1^{3/2}(-\alpha_2)^{3/2}}
\end{aligned}
$$

$$
\begin{aligned}
I_2(\delta) &= \frac{\delta^2\nu^{1-\Theta_b}\left(\sqrt{\pi}\mathrm{erf}\left(\sqrt{\alpha_1}\sqrt{-\alpha_2}\right)\left(-2\alpha_1(2\delta - h)(\alpha_1 - 3\Theta_b)\alpha_2^2 - 6\delta\Theta_b\alpha_2 - 3\delta\right)\right)}{24\alpha_1^{3/2}(-\alpha_2)^{5/2}} \\
&+ \frac{\delta^2\nu^{1-\Theta_b}\left(2\sqrt{\alpha_1}\nu^{\alpha_1}\sqrt{-\alpha_2}\left(\nu^{-\alpha_1}\left(\alpha_2(-2\delta(\alpha_1 - 6\Theta_b) - 3h\Theta_b) + 2\delta - h\right)\right)\right)}{24\alpha_1^{3/2}(-\alpha_2)^{5/2}} \\
&+ \frac{\delta^2\nu^{1-\Theta_b}\left(2\sqrt{\alpha_1}\nu^{\alpha_1}\sqrt{-\alpha_2}\left(2\delta\alpha_1\alpha_2 - 6\delta\Theta_b\alpha_2 + \delta - \alpha_1 h\alpha_2 + 3h\Theta_b\alpha_2 + h\right)\right)}{24\alpha_1^{3/2}(-\alpha_2)^{5/2}}
\end{aligned}
$$

where in addition to α_1, we also introduced $\alpha_2 = log(\nu)$ for clarity. In the case where $\nu = 1$, the expression above simplify and read

$$
\begin{aligned}
I_0(\delta) &= \frac{1}{2}\delta(\delta - h) \\
I_1(\delta) &= \frac{1}{12}\delta^2(4\delta - 3h) \\
I_1(h) &= \frac{h^3}{12} \\
I_2(\delta) &= -\frac{1}{120}\delta^2(18\delta\alpha_1 - 40\delta\Theta_b - 15\alpha_1 h + 30h\Theta_b)
\end{aligned}
$$

Appendix C: Second phase of the bending regime

For all simulations, the second phase of important thickening in the bending regime occurs in two stages: a first stage where the thickness drastically increases and a second stage where it continues increasing but much slower (Figure 4.3, 4.5 and 4.6). The transition is sharper for the rheology $\eta_1(\theta)$ and is enhanced by the smaller spatial resolution of the numerical simulations ($\Delta r = 0.005$) in Chapter 4 than in previous Chapter (Figure 4.6).

In all cases, it reflects the transition from the last moment of prewetting film cooling to the detachment of the thermal anomaly. For instance, for $\eta_1(\theta)$, $\nu = 0.001$ and $Pe = 100.0$, the transitions between the two stages occurs at $t = 1.8\ 10^{-2}$ and coincide to the film becoming entirely cold (Figure 4.6 a, b, c). Before this time, the average temperature in the film is non zero and after this time, the average temperature in the film is effectively $\overline{\theta} = 0$ and the thermal anomaly grows (Figure 4.6 c). For the rheology $\eta_2(\theta)$, the viscosity increases on a wide range of temperature and the transition is smoother (Figure 4.6 d, e, f).

Bibliography

Bercovici, D. (1994), A theoretical model of cooling viscous gravity currents with temperature-dependent viscosity, *Geophys. Res. Lett.* (Not cited.)

Blatt, H., R. J. Tracy, and B. Owens (2006), Petrology: igneous, sedimentary, and metamorphic. (Not cited.)

Carslaw, H. S., and J. C. Jaeger (1959), Heat in solids. (Not cited.)

Diniega, S., S. E. Smrekar, S. Anderson, and E. R. Stofan (2013), The influence of temperature-dependent viscosity on lava flow dynamics, *J. Geophys. Res. Earth Surf.*, *118*(3), 1516–1532. (Not cited.)

Everett, B. C., and T. D. Hoisch (2008), Conditions of metamorphism of the Colorado Yule Marble, *Rocky Mountain Association of Geologists*. (Not cited.)

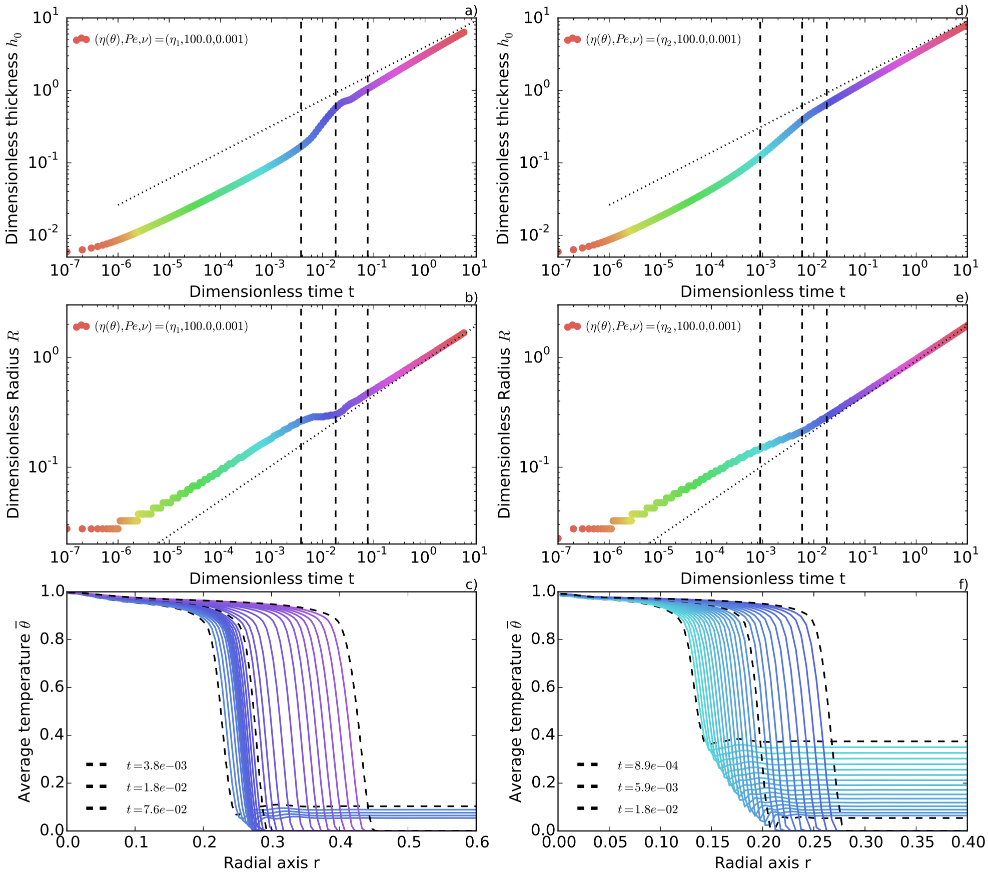

Figure 4.6: a) Dimensionless thickness h_0 versus dimensionless time t for $Pe = 100.0$, $\nu = 0.001$ and the rheology $\eta_1(\theta)$. Colors refer to the time t. Dotted line: Scaling law $h_0 = 0.7 h_f^{-1/11} \nu^{-2/11} t^{8/22}$. Vertical dashed-lines: initial, intermediate and final times of the temperature profiles plotted in c). b) Dimensionless radius R versus dimensionless time t for $Pe = 100.0$, $\nu = 0.001$ and the rheology $\eta_1(\theta)$. Colors refer to the time t. Dotted line: Scaling law $R = 2.2 h_f^{1/22} \nu^{1/11} t^{7/22}$. Vertical dashed-lines: same than in a). d) Dimensionless average temperature over the flow thickness $\overline{\theta}$ versus radial axis r for times between $t = 3.8\ 10^{-3}$ and $t = 7.6\ 10^{-2}$. Dashed-line profiles: profiles at the three different times marked in a) and b). Colors also refer to the time on the same scale than a) and b). d), e) and f), same plots than a), b) and c) but for the Arrhenius rheology η_2.

Part III

Crats l fractur Tins d'un magmatisme intrusif lunaire

Chapter 5

Floor-fractured craters

Chapter 6

Gravitationnal signature of lunar floor-fractured craters

Chapter 7

Conclusion